Analysis of CXCR4 in microglial pyroptosis after ischemia–reperfusion

Inauguraldissertation
zur Erlangung des Grades eines Doktors der Medizin
des Fachbereichs Medizin
der Justus-Liebig-Universität Gießen

vorgelegt von Yu Haiyang
Aus Heilongjiang China
Gießen 2026

Aus dem Fachbereich Medizin der Justus-Liebig-Universität Gießen

Universitätsklinikum Gießen und Marburg, Standort Gießen
Medizinisches Zentrum für Neurologie
Neurologische Klinik
Experimentelle Neurologie

Gutachter: Prof. Dr. Thorsten R. Döppner
Gutachter: Prof. Dr. Ralph Schermuly

Tag der Disputation: 03.07.2026

TABLE OF CONTENTS

Page

1 INTRODUCTION

1.1 Ischemic stroke and cerebral ischemia-reperfusion injury

1.1.1 Ischemic stroke

The latest estimates from the Global Burden of Disease 2021 study indicate that, among non-communicable diseases, stroke is the second leading cause of death worldwide and the third leading cause of disability when measured in disability-adjusted life years ("Global, regional, and national burden of stroke and its risk factors, 1990-2021: a systematic analysis for the Global Burden of Disease Study 2021," 2024). The global economic cost of stroke is estimated to exceed US$890 billion annually, representing approximately 0.66% of the world's gross domestic product, and is projected to double by 2050 (Feigin & Owolabi, 2023). Pathophysiologically, stroke is classified into ischemic stroke (IS) and hemorrhagic stroke (HS). IS typically results from occlusion of intracranial or extracranial arteries, most often because of thrombosis or embolism, leading to reduced cerebral blood flow, focal brain ischemia, and hypoxic and ischemic necrosis (Sacco et al., 2013). IS is the most common subtype, accounting for approximately 65.3% of strokes worldwide (Feigin et al., 2025). At present, therapies for stroke that are approved by the U.S. Food and Drug Administration (FDA) include recombinant tissue plasminogen activator (rtPA) thrombolysis, ultrasound assisted thrombolysis, and mechanical thrombectomy (Powers et al., 2019). However, restoration of cerebral blood flow can precipitate ischemia-reperfusion injury (Sah et al., 2019).

1.1.2 Cerebral ischemia-reperfusion injury

Ischemia-reperfusion injury of the brain arises from the concerted action of multiple pathophysiological processes. Decades of research have identified oxidative stress, intracellular calcium overload, inflammatory responses, and damage mediated by excitatory amino acids as the principal drivers of reperfusion injury (Wu et al., 2020; M. Zhang et al., 2024).
Ischemia-reperfusion injury is characterized by a rapid shift from oxygen deprivation to oxidative stress, which drives early cellular damage after cerebral vascular occlusion (Anaya-Fernández et al., 2024). After cerebral vascular occlusion, hypoxia impairs the mitochondrial

electron transport chain, reduces adenosine triphosphate (ATP) production, and depletes intracellular antioxidants such as glutathione (Anderson & Sims, 2002). When oxygen supply is restored during reperfusion, mitochondria generate excessive reactive oxygen species (ROS), including superoxide anion (O_2^-), hydrogen peroxide (H_2O_2), and hydroxyl radicals (•OH) (Orellana-Urzúa et al., 2020). In addition, the recruitment of inflammatory cells during reperfusion produces large amounts of O_2^- through nicotinamide adenine dinucleotide phosphate (NADPH) oxidase (Bedard & Krause, 2007). Excess ROS attack polyunsaturated fatty acids in cellular and organellar membranes and initiate lipid peroxidation chain reactions, generating toxic products such as malondialdehyde (MDA). This decreases membrane fluidity, disrupts ion channel function, and triggers opening of the mitochondrial permeability transition pore (mPTP), culminating in cellular swelling and necrosis (Martynov et al., 2023; Ong et al., 2015). ROS also oxidize protein sulfhydryl groups and methionine residues, resulting in enzyme inactivation and abnormal signaling. Oxidation of antioxidant enzymes further weakens endogenous defense capacity (Chen et al., 2020; Stadtman & Levine, 2000). Lipid peroxidation of neuronal membranes increases glutamate release and induces excitotoxicity (Keller et al., 1997). Moreover, ROS directly attack DNA bases, causing DNA damage, neuronal apoptosis, and impairment of cognitive function (Cooke et al., 2003).

During ischemia, insufficient adenosine triphosphate (ATP) impairs the Na^+/K^+-adenosine triphosphatase (Na^+/K^+-ATPase) on the plasma membrane, which fails to extrude accumulating intracellular Na^+ (Stys, 1998). Upon reperfusion, restoration of blood flow only partly normalizes Na^+/K^+-ATPase activity. Because intracellular Na^+ remains elevated, the sodium calcium exchanger (NCX) operates in reverse mode, extruding Na^+ while importing Ca^{2+} and thereby driving a rapid rise in cytosolic Ca^{2+} (Gerkau et al., 2017; Huang et al., 2015). In parallel, ischemia reperfusion is accompanied by massive glutamate release that overactivates N-methyl-D-aspartate receptors (NMDARs), further increasing neuronal Ca^{2+} influx (Choi, 2020). Calcium release channels in the endoplasmic reticulum are also activated during ischemia–reperfusion, causing substantial discharge of stored Ca^{2+} into the cytosol (Ruiz et al., 2009). Excess intracellular Ca^{2+} activates calcium dependent enzymes (Szydlowska & Tymianski, 2010). Phospholipases hydrolyze membrane phospholipids, release arachidonic acid, generate proinflammatory mediators such as leukotrienes and prostaglandins, and compromise membrane integrity (Adibhatla & Hatcher, 2008). Proteases dismantle cytoskeletal

proteins including microtubules and actin filaments, leading to loss of cellular architecture (Rami, 2003). Calcium entry into mitochondria collapses the mitochondrial membrane potential, inactivates components of the electron transport chain (ETC), and thereby aggravates ATP depletion while amplifying reactive oxygen species production (Zorov et al., 2014). Concurrently, pathological opening of the mitochondrial permeability transition pore (mPTP) promotes the release of cytochrome c and other proapoptotic factors, initiating apoptosis (Bernardi et al., 2015).

Cerebral ischemia-reperfusion leads to neuronal necrosis or apoptosis and the release of damage associated molecular patterns (DAMPs), including high mobility group box 1 (HMGB1), adenosine triphosphate (ATP), heat shock proteins (HSPs), and DNA fragments (Gülke et al., 2018). These signals bind pattern recognition receptors (PRRs), including Toll like receptor 4 (TLR4) and the NLR family pyrin domain containing 3 (NLRP3) inflammasome, thereby activating downstream pathways in microglia and initiating inflammatory responses (Var et al., 2021). In addition, ischemia increases the expression of endothelial adhesion molecules, which promotes the recruitment and adhesion of neutrophils and monocytes to the vessel wall, followed by transmigration into injured tissue where they release reactive oxygen species, proteases, proinflammatory cytokines, and chemokines. These events promote apoptosis, increase vascular permeability, and recruit additional immune cells (Bui et al., 2022). The complement system is also activated by recognition of antigen–antibody complexes on damaged cells through the classical pathway, or by direct binding to injured tissue through the alternative pathway. Complement component 5a (C5a) recruits neutrophils and enhances reactive oxygen species generation, while the membrane attack complex inserts into cell membranes to form pores that cause lysis (Diepenhorst et al., 2009). Moreover, inflammatory mediators induce endothelial expression of adhesion molecules and suppress nitric oxide synthesis, which contributes to vasospasm (Pober & Sessa, 2014; Var et al., 2021). Neutrophils and platelets form microthrombi that obstruct capillaries, impede restoration of flow, and aggravate ischemia and hypoxia (Denorme et al., 2022). Overall, the inflammatory component of cerebral ischemia-reperfusion injury involves excessive activation of innate immunity, cytokine driven amplification, and dysregulated complement activity, culminating in irreversible tissue damage.

Excitatory amino acids are key excitatory neurotransmitters in the brain, with glutamate as the predominant transmitter (Patri, 2019). The principal ionotropic glutamate receptors are the NMDAR and the α-amino-3-hydroxy-5-methyl-4-isoxazolepropionic acid receptor (AMPAR), together with kainate receptors. During ischemia, neuronal energy failure inactivates sodium potassium adenosine triphosphatase (Na^+/K^+-ATPase) and depolarizes the membrane, which opens voltage dependent calcium channels (VDCCs) and triggers massive presynaptic release of glutamate (Neves et al., 2023; Nishizawa, 2001). Ischemia-induced acidosis suppresses excitatory amino acid transporters (EAATs), thereby reducing glutamate clearance from the synaptic cleft (Swanson et al., 1995). In addition, EAATs on astrocytes and neurons can operate in reverse under energy deficit and altered membrane potential, releasing intracellular glutamate into the extracellular space (Rossi et al., 2000). Excessive activation of NMDAR induces substantial Ca^{2+} influx and simultaneously activates downstream signaling pathways, such as the neuronal nitric oxide synthase and nitric oxide (nNOS/NO) pathway, driving excess production of NO and other reactive nitrogen species (RNS) and thereby exacerbating oxidative stress (Dawson & Dawson, 2018; Guo & Ma, 2021). Overactivation of AMPAR increases Na^+ influx, further depolarizes the membrane, and secondarily activates VDCCs and NMDAR, which together aggravate Ca^{2+} entry. NMDAR activation also promotes microglial release of tumor necrosis factor alpha (TNF-α) and interleukin-1 beta (IL-1β), amplifying neuroinflammation (Lai et al., 2014; Wu & Tymianski, 2018). Glutamate activates metabotropic glutamate receptors on endothelial cells (mGluRs), which increases matrix metalloproteinase-9 (MMP-9) expression, promotes degradation of tight junction proteins, and disrupts the blood–brain barrier (BBB) (Asahi et al., 2001; Legros et al., 2009). In addition, glutamate exacerbates ischemic brain injury through acid-sensing ion channels (Lai et al., 2024).

1.2 Microglia in cerebral ischemia-reperfusion injury

1.2.1 The origin and development of microglia

Microglia constitute approximately 5 to 12% of cells in the central nervous system (CNS) and are the principal resident immune cells of the brain (Lawson et al., 1990). During human development, microglia derive from extraembryonic yolk sac erythromyeloid progenitors

(EMPs) that seed the embryonic CNS and, through a stepwise developmental program, differentiate into mature microglia (Ginhoux et al., 2010; Gomez Perdiguero et al., 2015). Under physiological conditions, microglia reside within the brain parenchyma in close contact with neurons, astrocytes, and oligodendrocytes (Thion et al., 2018). Although often described as resting, in vivo two photon imaging shows that microglia are highly dynamic and responsive to environmental cues (Nimmerjahn et al., 2005). In homeostasis, microglia patrol the local parenchyma with highly motile processes, perform macropinocytosis, and secrete trophic factors such as brain derived neurotrophic factor (BDNF); through frequent perisynaptic contacts they monitor synaptic function and tune neuronal activity (Mandrekar et al., 2009; Parkhurst et al., 2013; Wake et al., 2009). Beyond developmental regulation and structural refinement, microglia sustain brain homeostasis by clearing pathogens, dead cell debris, and abnormal proteins, and they participate in injury responses followed by tissue remodeling and repair (Orihuela et al., 2016). To detect noxious stimuli, microglia employ a broad repertoire of immune receptors (Hickman et al., 2018). When danger signals are encountered during surveillance, microglia activate rapidly and undergo characteristic morphological changes, including enlargement of the soma, retraction of processes, and increased phagocytic activity (Davalos et al., 2005; Jung et al., 2023; Orr et al., 2009). These properties underlie the central roles of microglia in brain development and in diverse central nervous system diseases.

1.2.2 Microglial activation and polarization

Microglia in the healthy adult CNS typically display a homeostatic, highly ramified morphology with a small soma and long, thin, branched processes that dynamically survey the surrounding parenchyma, whereas activation is commonly accompanied by soma enlargement, process thickening and retraction, and a shift toward hypertrophic and sometimes fully amoeboid forms with enhanced migratory and phagocytic capacity (Leyh et al., 2021) (Figure 1). Although microglial responses are now recognized as a heterogeneous continuum rather than a strict dichotomy, the M1/M2 polarization framework remains a useful heuristic to describe predominant pro-inflammatory versus reparative tendencies (Figure 1) (Ransohoff, 2016). In this paradigm, M1-like programs are often induced by TLR-related danger signaling and by

IFN-γ, engaging NF-κB and MAPK cascades together with JAK–STAT1 signaling to promote inflammatory effector outputs including TNF-α, IL-1β, iNOS-derived nitric oxide, and NOX2-driven ROS generation, which can amplify neuroinflammation and impose oxidative and excitotoxic stress on neurons (Azam et al., 2019; Mo et al., 2022) (Figure 1). Conversely, M2-like programs are preferentially promoted by IL-4/IL-13 and other pro-resolving cues, with STAT6 signaling supporting anti-inflammatory and repair-associated functions including debris clearance, inflammation resolution, and tissue remodeling, and alternative activation may be accompanied in some contexts by more elongated or bipolar "rod-like" morphologies observed during injury responses, though morphology alone does not uniquely define phenotype (Figure 1) (Mo et al., 2022; Rosito et al., 2023).

These functional states are coupled to immunometabolic remodeling, with homeostatic microglia relying largely on oxidative phosphorylation but shifting toward glycolysis during inflammatory activation, providing a mechanistic bridge between inflammatory signaling and microglia-mediated effects on neuronal survival and circuit integrity (Jung et al., 2025). Meanwhile, microglia can directly influence synaptic architecture, and in Alzheimer's disease models complement tagging and microglial engagement have been shown to drive early synapse loss, linking inflammatory microglial programs to network dysfunction and cognitive decline (Hong et al., 2016).

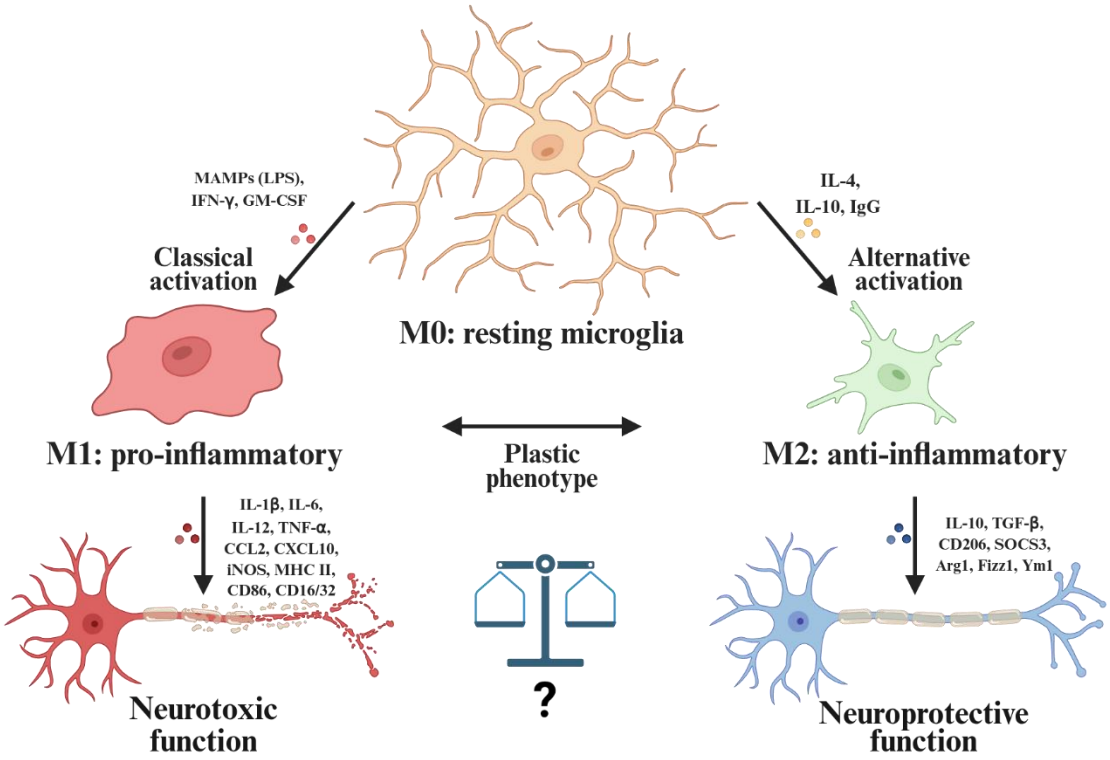

Figure 1. Microglial activation and polarization.
Resting microglia in the healthy CNS exhibit a highly ramified morphology and survey the parenchyma. Classical activation triggered by microbial and damage associated signals, including LPS, IFN-γ, and GM-CSF, promotes an M1-like pro-inflammatory state with increased expression of IL-1β, IL-6, IL-12, TNF-α, CCL2, CXCL10, iNOS, MHC II, CD86, and CD16/32 and is associated with neurotoxic effects. Alternative activation promoted by IL-4, IL-10, and IgG induces an M2-like anti-inflammatory state characterized by IL-10, TGF-β, CD206, SOCS3, Arg1, Fizz1, and Ym1 and is associated with neuroprotective and reparative functions. The bidirectional arrow and balance icon indicate phenotypic plasticity and context dependent switching between activation programs. The schematic was created with BioRender.

Single cell RNA sequencing indicates that, within the ischemic microenvironment, activated microglia occupy a continuum of phenotypes with heterogeneous co-expression of proinflammatory and anti-inflammatory gene programs, highlighting the inability of the M1/M2 framework to capture in vivo subpopulation diversity (H. Li et al., 2023). Single cell RNA sequencing has revealed that microglia display diverse transcriptional and functional states across development, brain regions, and disease contexts. Homeostatic microglia (HOM-M) predominate in healthy parenchyma and are characterized by expression of P2ry12, Tmem119, and Cx3cr1, consistent with the maintenance of central nervous system homeo-

stasis (Hammond et al., 2019; Li et al., 2019; Pettas et al., 2022; Zheng et al., 2021). Inflammatory microglia (IFLAM-M) emerge with innate immune activation and show high expression of Il1b, Ccl3, and Ccl4, with region specific representation across compartments (Hammond et al., 2019; Pettas et al., 2022; Zheng et al., 2021). Context dependent activation states also appear, including interferon responsive microglia (IFN-M), proliferative and lesion associated microglia (PLF-M), and myelin associated microglia (MYE-M), each defined by characteristic gene modules and observed in injury and demyelination models as well as after ischemia (Hammond et al., 2019; Li et al., 2019; Pettas et al., 2022; Zheng et al., 2021). Developmentally related subpopulations include embryonic microglia subsets EM1 (CD68 negative, Iba1 positive, highly proliferative) and EM2 (CD68 positive, Iba1 positive, with clearance and neuromodulatory functions), and the proliferative region associated microglia (PAM) enriched in developing white matter with pronounced phagocytic activity (Cheng et al., 2025; Li et al., 2019). Microglial activation after ischemic injury is initiated by the abnormal release of intracellular constituents, including nucleic acids, lipids, and functional proteins, into the extracellular matrix. These damage-associated molecular patterns (DAMPs) engage pattern recognition receptors (PRRs) on the microglial membrane and transduce signals through inflammatory pathways, triggering cascades of proinflammatory cytokines and chemokines that drive the infiltration of peripheral immune cells into the central nervous system (Inose et al., 2015; Q. Li et al., 2020; Patel, 2018). During this process, homeostatic microglia undergo phenotypic and functional transitions characterized by enlargement of the soma and retraction of processes, while remodeling of surface receptor networks and enzyme systems enhances phagocytic capacity and immune regulatory functions (Woodburn et al., 2021).

Microglia also shape post-ischemic pathology through multicellular interactions. By secreting distinct cytokine profiles, they regulate astrocyte activation states, and by phagocytosing neutrophils in the ischemic penumbra they exert immunomodulatory effects that influence lesion evolution (Matejuk & Ransohoff, 2020; Neumann et al., 2008). From the perspective of immune regulation, microglia display dual capacities. Through antigen presentation mediated by major histocompatibility complex (MHC) molecules they can activate T-cell responses, while anti-inflammatory cytokines such as interleukin 10 (IL-10) restrain excessive T-cell activation (Garcia et al., 2017; Jin et al., 2018). In addition, regulatory T cells (Tregs)

dampen aberrant microglial activation through direct cell–cell contact and soluble mediators (Y. Liu et al., 2023). During post-stroke repair, microglia exhibit bidirectional roles. Their phagocytic clearance of apoptotic neurons and necrotic debris limits secondary injury cascades and curbs the spread of inflammatory mediators, which facilitates resolution of neuroinflammation and supports synaptic remodeling (Jia et al., 2021). By selectively recognizing and engulfing axonal and myelin breakdown products, microglia not only cleanse the lesional microenvironment but also provide conditions that favor axonal regrowth and remyelination (Lampron et al., 2015). At the network level, activated microglia fine tune local immune tone by removing pathogens, aberrant immune cells, and inflammatory mediators, thereby preventing secondary neuronal injury caused by unchecked inflammation (Yu et al., 2022). These phagocytic programs are governed by integrated signaling, particularly Toll like receptors (TLRs) and nuclear factor kappa B (NF-κB), which dynamically regulate the expression of genes required for engulfment, set activation thresholds, and orchestrate switches between phagocytic modes (Janda et al., 2018; Zhao et al., 2013). Notwithstanding their protective roles, excessively activated microglia may engulf stressed yet viable neurons that retain electrophysiological activity, leading to neuronal loss, disruption of network integrity, and impeded functional recovery (Neher et al., 2013). Consequently, delineating the key molecules and mechanisms that govern microglial polarization, function, and phenotypic transitions after cerebral ischemia is essential for precise control of post-stroke neuroinflammation and for rational strategies to rebuild neural circuits.

1.2.3 Molecular mechanisms of microglial pyroptosis

Pyroptosis is a form of programmed cell death that is mechanistically and morphologically distinct from apoptosis and necroptosis, with gasdermin D (GSDMD) executing pyroptosis and mixed lineage kinase domain like protein (MLKL) executing necroptosis (Shi et al., 2015; Zhan et al., 2021). In microglia, pyroptosis is typically described as a two-step process. The priming step involves induction of inflammasome related genes by microbial products and inflammatory mediators. This is followed by activation of the inflammasome and downstream pathways that culminate in GSDMD mediated pore formation and lytic cell death (Broz & Dixit, 2016; Swanson et al., 2019). The GSDM protein family is broadly expressed across cell types and tissues. In humans, paralogs include GSDMA, GSDMB, GSDMC,

GSDMD, and GSDME (also known as DFNA5), as well as pejvakin (PJVK, also known as DFNB59). In mice, paralogs of GSDMA1-3, GSDMC1-4, GSDMD, DFNA5, and DFNB59 have been identified (Aglietti & Dueber, 2017; Ding et al., 2016). With the exception of DFNB59, all GSDM proteins share a pore forming N terminal domain, an autoinhibitory C terminal domain, and a flexible interdomain linker. Proteolytic cleavage that separates the N and C termini releases the cytotoxic N terminal fragment, which inserts into membranes and oligomerizes to form large pores that disrupt ionic homeostasis and trigger cell death (Ding et al., 2016; Shi et al., 2015). Pyroptosis is commonly initiated and propagated by inflammasomes, accompanied by GSDMD cleavage and the release of interleukin 1 beta (IL-1β) and interleukin 18 (IL-18) (Xia et al., 2019). Pathogen associated molecular patterns (PAMPs) and damage associated molecular patterns (DAMPs) are key triggers for inflammasome assembly. When cytosolic pattern recognition receptors (PRRs), also termed inflammasome sensors, detect PAMPs or DAMPs, inflammasome assembly is initiated (Liston & Masters, 2017; Zheng et al., 2020). Most inflammasomes comprise a nucleotide binding oligomerization domain like receptor (NLR) sensor containing leucine rich repeats, the adaptor apoptosis associated speck like protein containing a caspase recruitment domain (ASC), and pro caspase 1 (Zheng et al., 2020). Upon activation of inflammasome sensors, pro caspase 1 is cleaved to active caspase 1. One branch of the pathway cleaves GSDMD into C and N terminal fragments, with the N terminal fragment rapidly perforating the plasma membrane to execute pyroptosis (Shi et al., 2015). In parallel, caspase 1 processes pro IL 1β and pro IL 18 into their mature forms, which are subsequently released through GSDMD formed pores, thereby amplifying inflammation and driving pyroptotic cell death (He et al., 2015). Experimental evidence supports a pathogenic role for microglial pyroptosis in ischemia reperfusion. Recent studies report marked upregulation of GSDMD in microglia within ischemic regions (Li et al., 2024). After OGD and reoxygenation, microglia not only exhibit increased intracellular inflammasome content but, after membrane permeabilization, also release inflammasome components and DAMPs into the culture medium, which act directly on neighboring cells to propagate inflammatory cascades and exacerbate injury (Lücht et al., 2021). In rat focal cerebral ischemia reperfusion and in microglial OGD models, silencing GSDMD limits membrane pore formation, reduces the secretion of mature IL-1β and IL-18 by microglia, dampens caspase 1 mediated inflammatory signaling, and accelerates neurological recovery

after ischemia reperfusion injury (Wang et al., 2020). Collectively, these observations indicate that microglial pyroptosis represents an important mechanism of cerebral ischemia-reperfusion injury.

1.3 The role of C-X-C motif chemokine receptor 4 (CXCR4) in ischemia

1.3.1 The CXCL12–CXCR4 axis in the post-ischemic penumbra

Ischemic stroke initiates a rapid neurovascular cascade that extends beyond the initial energy failure. In the acute phase, sterile inflammation and leukocyte recruitment contribute to blood–brain barrier disruption, edema, and secondary neuronal injury, while later inflammatory remodeling can also participate in tissue repair and functional recovery (Iadecola & Anrather, 2011; Yang et al., 2019). These phase-dependent effects have motivated increasing attention to chemokine pathways that coordinate cell trafficking and intercellular communication within the ischemic penumbra. Among chemokine systems, the CXCL12 axis, historically termed stromal cell-derived factor 1 (SDF-1), and its canonical receptor CXCR4 represent a central node linking inflammatory cell migration with neural and vascular plasticity. After focal ischemia, CXCL12 and CXCR4 are induced in peri-infarct regions and have been associated with the homing of bone marrow-derived cells to injured brain tissue (Hill et al., 2004; Wang et al., 2012). Early experimental work further established that SDF-1 isoform–selective regulation can differentially engage CXCR4-dependent neuronal plasticity and cerebral leukocyte recruitment after focal ischemia, providing a mechanistic basis for the “dual role” concept of this axis in stroke pathophysiology (Stumm et al., 2002).

1.3.2 Acute injury amplification via CXCR4 and antagonist studies

Substantial evidence indicates that CXCL12–CXCR4 signaling can exacerbate acute injury, largely through promoting leukocyte trafficking, amplifying local cytokine programs, and aggravating BBB dysfunction. Pharmacologic blockade of CXCR4 with AMD3100 suppressed inflammatory responses and reduced BBB disruption after middle cerebral artery occlusion in mice (J. Huang et al., 2013). Beyond AMD3100, the development of alternative CXCR4 antagonists has reinforced this acute neuroprotective paradigm. CX549 showed higher affinity for CXCR4 than AMD3100 in vitro and, when administered early after stroke

in rodent models, improved behavioral outcomes, reduced infarct size, and suppressed inflammatory marker expression, consistent with attenuation of neuroinflammatory amplification (Wu et al., 2017). At the same time, CXCR4 signaling has been linked to inflammatory execution pathways in acute brain injury paradigms. For example, a CXCR4–BTK axis was reported to regulate NLRP3-mediated pyroptosis via NF-κB signaling in early brain injury after subarachnoid hemorrhage, suggesting plausible mechanistic intersections between CXCR4 signaling and inflammasome-driven cell death that warrant focused validation in ischemic stroke contexts (C. Liu et al., 2023). Collectively, these studies support the rationale that early CXCR4 antagonism can be beneficial when inflammatory recruitment and neurovascular permeability are dominant drivers of secondary damage.

1.3.3 Reparative CXCR4 signaling in later phases

Subacute and chronic phases highlight a reparative dimension of the same axis. Reviews synthesizing experimental and translational data describe CXCL12 signaling through CXCR4 and CXCR7 as an organizer of neural precursor migration, angiogenesis, and post-stroke axonal remodeling, implying that prolonged or indiscriminate inhibition could compromise endogenous recovery programs (Cheng et al., 2017; Wang et al., 2012). Consistent with this view, strategies that enhance CXCR4-dependent homing of reparative cells have demonstrated benefit in experimental stroke. CXCR4 overexpression in mesenchymal stem cells promoted migration and improved neuroprotection and angiogenesis in a rat model of cerebral ischemia (Yu et al., 2012). Similarly, transfusion of CXCR4-primed endothelial progenitor cells reduced ischemic damage and promoted repair in db/db diabetic mice, supporting the concept that augmenting CXCR4-mediated recruitment may be particularly relevant in comorbidity contexts where repair is impaired (Chen et al., 2012). Paracrine delivery routes have also been explored: exosomes derived from CXCR4-overexpressing BMSCs promoted microvascular endothelial proliferation and tube formation and were associated with anti-apoptotic effects in ischemia–reperfusion settings (X. Li et al., 2020).

Taken together, current evidence supports a model in which CXCR4 modulation requires strict consideration of timing, cellular target, and receptor network context. Acute antagonism may mitigate neurovascular inflammation, whereas later-phase enhancement of CXCR4-dependent homing or circuit remodeling may support recovery.

1.4 Aims and objectives

The primary aim of this doctoral thesis was to investigate the role of CXCR4 in pyroptosis induced by cerebral ischemia–reperfusion after stroke, and to evaluate whether the selective CXCR4 chemokine receptor antagonist AMD3100 can attenuate acute-phase pyroptotic injury under ischemia–reperfusion conditions.

The central hypothesis was that pharmacological blockade of CXCR4 by AMD3100 dampens inflammasome activation and caspase-1 activity, thereby reducing caspase-1–mediated cleavage of gasdermin D and limiting generation of the pore-forming GSDMD N-terminal fragment, ultimately mitigating pyroptotic execution and downstream inflammatory amplification (Figure 2).

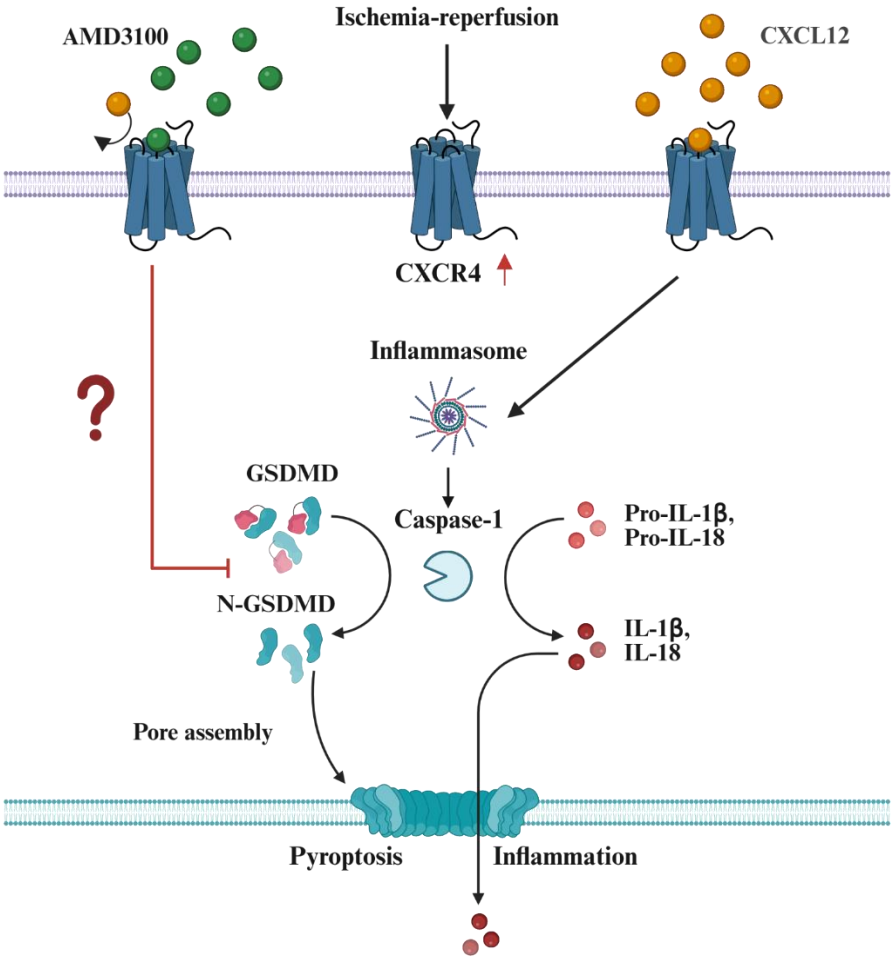

Figure 2. The central hypothesis of this study.

AMD3100 blocks CXCR4, reduces caspase-1–mediated GSDMD cleavage and GSDMD N-terminal fragment formation, and thereby limits pore assembly, pyroptotic execution, and downstream IL-1β and IL-18 release. The schematic was created with BioRender.

To test this hypothesis, the specific objectives were as follows.

1) To characterize transcriptomic changes in CXCR4 following cerebral ischemia–reperfusion and to define the temporal pattern of CXCR4 induction in post-stroke brain tissue.
2) To leverage single-cell transcriptomic data to examine the association between CXCR4 axis activity and pyroptosis-related programs in microglia after cerebral ischemia–reperfusion.
3) To establish an in vitro ischemia–reperfusion model in primary mouse microglia and to determine the effect of AMD3100 on GSDMD N-terminal fragment generation and membrane pore formation under OGD and reoxygenation conditions.

2 MATERIAL AND METHODS

This thesis was prepared on Windows 10/11 using Microsoft Word 2021. Figures and tabular reports were produced with Microsoft Excel 2021, GraphPad Prism 9, Adobe Illustrator CC 2023, and BioRender. Image processing and quantification were carried out in Fiji/ImageJ, and microscope acquisition and basic analysis used Leica Application Suite X (LAS X). Computational analyses were performed in R within RStudio. Batch data processing and automation were performed in Python (pandas, NumPy) using the Spyder IDE. All scripts and parameters were version-controlled and audited at runtime.

2.1 Equipment

Table 1. Equipment

Equipment Name	Manufacturer, Country
Analytical Balance	Mettler-Toledo, Switzerland
Automated Cell Counter LUNA™	Logos Biosystems, Korea
Biological Safety Cabinet	NuAire, USA
Cell Culture Incubator	Thermo Scientific, USA
Centrifuge EBA 20	Hettich, Germany
Centrifuge Mikro 120	Hettich, Germany
Centrifuge Universal 320 R	Hettich, Germany
ChemoCam Imager ECL System	INTAS, Germany
Electrophoresis Power Supply EV 231	PEQLAB Biotechnologie, Germany
Hypoxic Chamber System	DR. NEUMANN, Germany
Inverted Microscope DMi1	Leica, Germany
Laminar Flow Hood	Thermo Scientific, USA
Live-cell Imaging Microscope DMi8 S	Leica, Germany
Magnetic Stirrer RH B S000	IKA, Germany
Microplate Reader Multiskan EX	Thermo Scientific, USA
Mini-PROTEAN® Tetra Vertical Electrophoresis Cell	Bio-Rad, USA
pH Meter edge®	Hanna, USA
Pipette Controller pipetus®	Hirschmann, Germany
Pipettes & Multi-Dispenser	Eppendorf / Gilson / Sartorius, Germany / France / Germany
Platform Shaker Rotamax 120	Heidolph, Germany
Refrigerators and Freezers	Liebherr / Panasonic / Thermo Fisher, Germany / Japan / USA
Roller Mixer RM5 Assistant 348	Karl Hecht, Germany
Thermomixer comfort	Eppendorf, Germany
Trans-Blot® SD Transfer System	Bio-Rad, USA
Vortex Mixer peqTWIST	PEQLAB, USA
Water Bath	Memmert, Germany

2.2 Chemicals and reagents

Table 2. Chemicals and reagents

Product Name	Manufacturer, Country
3-(4,5-Dimethyl-2-thiazolyl)-2,5-Diphenyl-2H-Tetrazolium-Bromid (MTT)	Merck, Germany
4',6-diamidino-2-phenylindole, dihydrochloride (DAPI)	Thermo Scientific, USA
AMD3100 octahydrochloride hydrate	Merck, Germany
Ammonium persulfate (APS)	Carl Roth, Germany
Bovine Serum Albumin (BSA)	Capricorn Scientific, Germany
Calcium chloride ($CaCl_2$)	Carl Roth, Germany
DC™ Protein Assay Kit	Bio-Rad, USA
Dimethyl sulphoxide (DMSO)	Carl Roth, Germany
DMEM, high Glucose, GlutaMAX™ Supplement	Thermo Scientific, USA
Dulbecco's PBS (10x) (DPBS)	Capricorn Scientific, Germany
Ethanol	Merck, Germany
Fetal Bovine Serum (FBS)	Thermo Scientific, USA
Glycine	Merck, Germany
Hanks' Balanced Salt Solution (10X) (HBSS)	Thermo Scientific, USA
HEPES Buffer Solution (1M)	Thermo Scientific, USA
Hydrochloric acid (HCl)	Merck, Germany
Magnesium sulfate heptahydrate ($MgSO_4$)	Carl Roth, Germany
Methanol	Carl Roth, Germany
Nonfat Dry Milk	Cell Signaling, USA
PageRuler™ Prestained Protein Ladder	Thermo Scientific, USA
Paraformaldehyde (PFA)	Carl Roth, Germany
PBS Buffer (10× Dulbecco's) Powder	AppliChem, Germany
Penicillin-Streptomycin (P/S)	Thermo Scientific, USA
Pierce™ RIPA Buffer	Thermo Scientific, USA
Phosphatase Inhibitor Cocktail	Sigma-Aldrich, USA
Poly-D-Lysin (PDL, 0.1 mg/mL)	Thermo Scientific, USA
Potassium chloride (KCl)	Carl Roth, Germany
ProLong™ Glass Antifade Mountant	Life Technologies, USA
Protease Inhibitor Cocktail Tablets	Merck, Germany
Restore™ PLUS Western Blot Stripping Buffer	Thermo Scientific, USA
ROTI®Load 1	Carl Roth, Germany
ROTIPHORESE® Gel 30 (37.5:1)	Carl Roth, Germany
ROTIPHORESE®10x SDS-PAGE	Carl Roth, Germany
SDS (ultra pure)	Carl Roth, Germany
Sodium chloride (NaCl)	Carl Roth, Germany
Sodium dihydrogen phosphate (NaH_2PO_4)	Carl Roth, Germany
Sodium hydrogen carbonate ($NaHCO_3$)	Carl Roth, Germany
SuperSignal™ West Pico PLUS Chemilumineszenz-Substrat	Thermo Scientific, USA
TEMED	Carl Roth, Germany
TRIS (PUFFERAN®, ≥99.9%, p.a.)	Carl Roth, Germany
Tris-HCl buffer (pH 6.8)	Bio-Rad, USA
Tris-HCl buffer (pH 8.8)	Bio-Rad, USA

Product Name	Manufacturer, Country
Triton™ X-100 solution (10%)	Sigma-Aldrich, USA
Trypsin-EDTA (0.5 %)	Thermo Scientific, USA
Tween® 20	Sigma-Aldrich, USA

2.3 Consumables

Table 3. Consumables

Product Name	Manufacturer, Country
Cell culture 100×20 mm dish	Sarstedt, Germany
Cell culture 24-well plate	Sarstedt, Germany
Cell culture 60×15 mm dish	Sarstedt, Germany
Cell culture 6-well plate	Sarstedt, Germany
Cell culture 96-well plate	Greiner Bio-One, Germany
Cell culture T-25 flask	Greiner Bio-One, Germany
Cell culture T-75 flask	Sarstedt, Germany
Cell scraper	Greiner Bio-One, Germany
Cell strainer 70 µm (Falcon)	Corning, USA
Corning™ 500 mL Vacuum Filter	Thermo Scientific, USA
Coverslip	R. Langenbrinck, Germany
Extra thick blot paper 19×18.5 cm	Bio-Rad, Germany
Glass Pasteur pipette 150 mm	BRAND, Germany
Micro tube, 1.5 mL & 2.0 ml & 5 mL	Sarstedt, Germany
Mini-PROTEAN 10-well comb (1.5 mm)	Bio-Rad, Germany
Mini-PROTEAN glass plates (1.5 mm, set)	Bio-Rad, Germany
Mr. Frosty™ freezing container	Thermo Scientific, USA
Nitrile powder-free glove	B. Braun, Germany
Parafilm M sealing film	Amcor, USA
Pipette Tip, 20 µL & 100 µL & 1000µL	Sarstedt, Germany
Screw cap tube, 15 mL	Sarstedt, Germany
Screw cap tube, 50 mL	Sarstedt, Germany
Serological pipette, 2 mL & 5 mL & 10 mL & 25 mL	Greiner Bio-One, Germany
Syringe filter (0.2µm)	Sartorius, Germany
Transfermembran ROTI®PVDF 0.45µm	Carl Roth, Germany

2.4 Bioinformatics analysis

2.4.1 Bulk RNA sequencing analysis of microglia after ischemia–reperfusion

Publicly available bulk RNA-seq data of FACS-purified mouse microglia were obtained from GEO (GSE220042). In the original study, transient focal ischemia was induced by 60 min MCAO followed by 3 days of reperfusion, and microglia were sorted as $CD11b^{+}/CD45^{int}$;

raw two-column HTSeq-count files from three sham and three MCAO samples were downloaded and analyzed in the present study. Count files were merged in R into a gene-by-sample matrix (genes with zero counts across all samples were removed), and differential expression between MCAO and sham was tested using DESeq2 with Benjamini–Hochberg correction; DEGs were defined as adjusted $P < 0.05$ and $|\log_2FC| > 1$. Variance-stabilized counts were used for PCA, and volcano plots were generated from $\log_2FC$ and adjusted P values. Functional enrichment for GO (BP/CC/MF) and KEGG was performed with clusterProfiler after ID conversion using org.Hs.eg.db, and term directionality was quantified by z scores calculated with GOplot from gene-level $\log_2FC$ values. Enriched terms containing CXCR4 were identified by screening term gene sets, and co-occurrence analysis counted genes that repeatedly appeared with CXCR4 across significant terms, with additional extraction of terms jointly containing CXCR4 and Il1b. All analyses and visualizations were conducted in R 4.2.1, with plots produced using ggplot2 (v3.3.6).

2.4.2 ScRNA sequencing analysis of microglia after ischemia–reperfusion

Public scRNA-seq data were obtained from GEO (GSE174574), comprising three MCAO and three sham mouse brain samples collected 24 h after a 60 min MCAO or sham procedure. For each sample, raw cell-by-gene count matrices with corresponding barcode and feature files were downloaded and imported into R for downstream analysis. Single-cell preprocessing was performed in Seurat, including quality control filtering to remove low-quality barcodes and low-information genes, followed by library-size normalization, log transformation, selection of highly variable genes, and principal component analysis. Replicates were then integrated using a condition-aware batch-correction strategy to reduce inter-sample technical effects while preserving ischemia–reperfusion–associated biology. The integrated object was embedded by UMAP and clustered using graph-based unsupervised clustering. Major brain cell types were annotated based on canonical marker expression, including microglia, infiltrating myeloid cells, endothelial cells, astrocytes, oligodendrocytes, oligodendrocyte precursor cells, ependymal cells, pericytes, smooth-muscle cells, and lymphoid lineages. Cell-type composition was quantified by counting annotated cells within each condition and reporting proportions.

For microglia-focused analyses, annotated microglia were subsetted, reintegrated across replicates, and reclustered to resolve within-microglia state structure. Cluster markers were identified using Seurat FindAllMarkers with the Wilcoxon rank-sum test and Benjamini–Hochberg correction, and representative markers were prioritized by effect size and within-cluster prevalence. Pseudotime ordering within MCAO microglia was inferred using Slingshot based on UMAP coordinates and Seurat cluster labels, with the homeostatic cluster specified as the root; pseudotime values were min–max scaled for visualization and summarized by cluster medians.

Pyroptosis-related transcriptional programs were quantified by defining literature-based activation, execution, and composite gene sets and computing per-cell module scores using Seurat AddModuleScore on the batch-corrected microglial object. Cluster-wise differences were assessed relative to sham microglia in the homeostatic cluster using nonparametric testing with multiple-testing correction, and complementary sample-level summaries were obtained from per-sample mean module scores. A CXCL12–CXCR4 axis score was computed by module scoring, and associations with pyroptosis scores were evaluated using Spearman correlation within all microglia and within each condition, followed by Benjamini–Hochberg adjustment. To estimate regulatory consequences of CXCR4 loss, a network-based virtual knockout was performed with scTenifoldNet by constructing wild-type and CXCR4-silenced regulatory networks for each MCAO microglial cluster, comparing networks via manifold alignment, and summarizing module-level regulatory shifts with oriented Stouffer Z scores for visualization.

All single-cell analyses and visualizations were performed in R 4.4.1. Seurat was used for preprocessing, integration, clustering, marker detection, and module scoring, Slingshot for pseudotime inference, scTenifoldNet for virtual knockout analysis, and ggplot2 for figure generation. Package versions and session information were recorded to ensure reproducibility.

2.5 Isolation of primary microglia

Primary microglia were prepared based on a published protocol (Du et al., 2021) with some modifications.

2.5.1 Preparation of culture buffer, solution, flasks, and dissection tools

HBSS (1×):

A total of 100 mL of 10× HBSS and 0.35 g of $NaHCO_3$ were added to 900 mL of ddH_2O. The buffer was stirred on a magnetic stirrer for 10 min, the pH was adjusted to 7.0-7.4, and it was stored at 4 °C.

Culture medium (10% FBS, 1% P/S):

50 mL PBS and 5 mL P/S were added to 445 mL of DMEM GlutaMAX™ Supplement. The medium was stored at 4 °C.

DPBS (1×):

A total of 100 mL of 10× DPBS was diluted with 900 mL of ddH_2O to a final volume of 1 L. The solution was stored at 4 °C.

Coating flasks:

T-75 flasks were used for pre-plating the isolated brain cells. Prior to brain dissection, the flasks were coated with 6 mL of 0.1 mg/mL PDL and incubated at 37 °C for at least 1 h. The PDL solution was then aspirated, the flasks were washed twice with ddH_2O, and allowed to air-dry in the cell culture hood.

Dissection tools:

Dissection tools, including fine scissors and forceps, were soaked in 75% ethanol for at least 20 min prior to use.

2.5.2 Dissection of mouse brain

1) Newborn (P0-P4) wild-type C57BL/6J mice were decapitated using surgical scissors, and brains were immediately placed in ice-cold 1× HBSS. During this step, the culture medium was warmed in a 37 °C water bath.
2) Fine dissecting scissors were used to cut the skull along the medulla oblongata. A forceps was placed beneath the brain tissue at the cutting site to gently lift and remove the brain from the cranial cavity. The brain was transferred to a new chilled 60 mm dish containing ice-cold 1× HBSS.
3) The cerebellum and olfactory bulbs were removed and discarded. The cerebral cortex was then isolated from the remaining brain tissue, stripped of the meninges, and gently transferred to a chilled 15 mL tube containing 5 mL of ice-cold 1× HBSS.

4) The procedure was repeated until all brain tissues were collected.

2.5.3 Seeding of mixed primary cells

1) The cerebral cortex was transferred to a 60 mm dish and minced into small pieces (approximately 1 mm^2) using micro scissors. The tissue pieces were then transferred to a 50 mL tube.
2) 2 mL of culture medium was added, and the tissue was triturated sequentially with 25 mL, 5 mL, and 10 mL pipettes in that order. To remove large clumps and debris, the cell suspension was passed through a 70 μm cell strainer, and the flow-through was collected in a 50 mL tube.
3) The cell suspension was transferred to a 15 mL tube and centrifuged at 2500 rpm for 5 min at room temperature.
4) The supernatant was aspirated, and the cell pellet was resuspended in 2 mL of culture medium. The primary cells were seeded into T-75 flasks (three brains per flask, 10 mL of culture medium per flask) and cultured in a humidified incubator (5% CO_2, 37 °C). This was considered Day 0 of the culture schedule.

2.5.4 Collection of primary microglia

1) Every 2-3 days, the flasks were washed with 5 mL of warm 1× DPBS, and the medium was replaced with 10 mL of fresh culture medium until astrocytes reached 100% confluency (typically on Day 5–7). The astrocyte layer at this stage is shown in Figure 3A.
2) During this period, a subpopulation of microglia loosely attached to the mixed cell layer began to proliferate. A half-medium change was performed every 3–4 days by replacing 5 mL of the old medium with an equal volume of fresh culture medium, and this was continued until microglia reached confluency in the T-75 flask (typically on Day 14–19). Representative morphology at this stage is shown in Figure 3B.
3) Microglia were detached from the surface by gentle handshaking, and the culture medium containing the cells was collected into a 15 mL tube. The suspension was centrifuged at 2000 rpm for 5 min at room temperature.
4) The supernatant was aspirated, and the cells were resuspended in 2 mL of culture medium. Cell counting was performed using a hemocytometer. Primary microglia were then seeded

into 6-well plates (400,000 cells per well in 2 mL of culture medium) or 24-well plates (80,000 cells per well in 1 mL of culture medium) for subsequent experiments. Attached microglia are shown in Figure 3C.

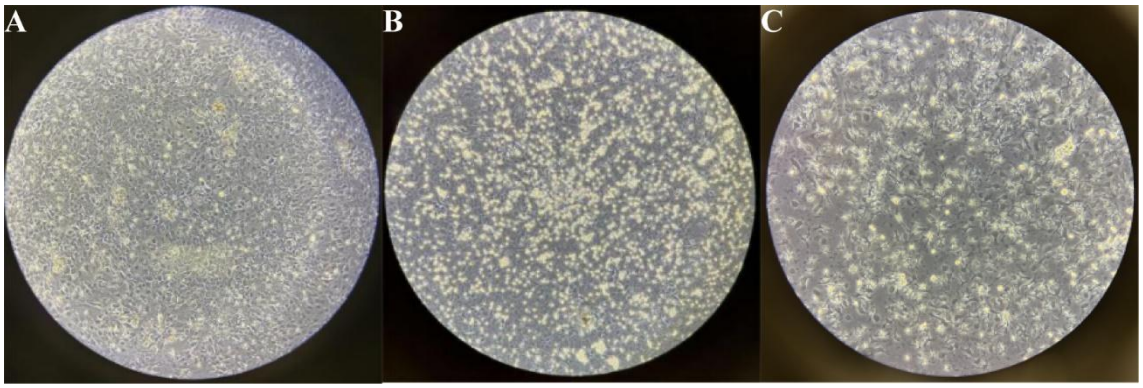

Figure 3. Primary microglia harvest and seeding from mixed glial cultures.

A. Astrocyte monolayer at confluence (Day 5–7); **B.** Emergence and expansion of loosely attached microglia on the mixed glial layer (Day 14–19); **C.** Attached primary microglia exhibiting ramified morphology with small somata and thin branched processes.

2.6 Oxygen-glucose deprivation (OGD) Model

2.6.1 Preparation of solutions.

BSS0 (10× stock solution):

A total of 34 g of NaCl, 2 g of KCl, 1 g of $MgSO_4$, and 0.7 g of NaH_2PO_4 were dissolved in ddH_2O to a final volume of 500 mL. The solution was mixed thoroughly, filtered through a 500 mL vacuum filter, and stored at 4 °C.

30 mM Glycine:

A total of 22.5 mg of glycine and 1 mL of 10× BSS0 were dissolved in ddH_2O to a final volume of 10 mL. The solution was mixed thoroughly and stored at 4 °C.

1 M $NaHCO_3$:

A total of 8.4 g of $NaHCO_3$ was dissolved in ddH_2O to a final volume of 100 mL. The solution was mixed thoroughly, and stored at 4 °C.

1 M $CaCl_2$:

A total of 1.11 g of $CaCl_2$ was dissolved in ddH_2O to a final volume of 10 mL. The solution was mixed thoroughly and stored at 4 °C.

BSS0 (1×):

A total of 13.1 mL of 1 M $NaHCO_3$, 5 mL of 1 M HEPES, 166 µL of 30 mM glycine, 900 µL of 1 M $CaCl_2$, and 50 mL of 10× BSS0 were combined in ddH_2O and brought to a final volume of 500 mL. The solution was mixed thoroughly, sterile-filtered (0.2 µm), and stored at 4 °C.

2.6.2 Cell preparation

Primary microglia were cultured until they reached 80-90% confluency. Upon reaching confluency, the cells were washed once with 1× DPBS to remove residual nutrients.

2.6.3 OGD induction

The culture medium was replaced with an equal volume of glucose-free balanced salt solution (BSS0 1×). The cells were then transferred to a hypoxic chamber system and incubated under hypoxic conditions (1.5% O_2, 5% CO_2, 45% humidity, 37 °C) for a predetermined time according to the experimental design.

2.6.4 Reoxygenation (RO)

After hypoxic incubation, BSS0 (1×) was removed, and the cells were washed once with 1× DPBS. Fresh culture medium was then added, and the cells were incubated under normoxic conditions (5% CO_2, 37 °C) for 12 h. The cells were then collected for subsequent analyses as required.

2.7 MTT Cell Viability Assay

2.7.1 Preparation of MTT solution

1) A total of 500 mg of MTT powder [3-(4,5-dimethyl-2-thiazolyl)-2,5-diphenyl-2H-tetrazolium bromide] was dissolved in 100 mL of ddH_2O to obtain a 5 mg/mL stock solution.
2) The solution was stirred on a magnetic stirrer for 1-2 h in the dark until the powder was completely dissolved. It was then sterile-filtered through a 0.2 µm syringe filter, aliquoted

into 15 mL tubes, and stored at -20 °C protected from light.

2.7.2 Assay procedure

1) MTT solution (100 µL, 5 mg/mL) was added to each well of a 24-well plate containing 0.9 mL culture medium, yielding a final MTT concentration of 0.5 mg/mL.
2) The plates were incubated for 3 h at 37 °C, protected from light. The MTT solution was then removed and replaced with 1 mL of dimethyl sulfoxide (DMSO).
3) The plates were shaken on an orbital shaker at 200 rpm for 3-5 min at room temperature to dissolve the formazan crystals.
4) Subsequently, 200 µL of the dissolved solution from each well was transferred to a 96-well plate, and absorbance was measured at 570 nm using a microplate reader.

2.8 Immunofluorescence

2.8.1 Preparation of solutions

PBS (10× stock solution):

A total of 99.5 g of PBS powder was dissolved in ddH_2O to a final volume of 1 L. The solution was mixed thoroughly and stored at 4 °C.

PBS (1×):

A total of 100 mL of 10× PBS was diluted with 900 mL of ddH_2O to obtain a 1× working solution. The solution was mixed thoroughly, the pH was adjusted to 7.2-7.6, and it was stored at 4 °C.

4% Paraformaldehyde (PFA):

A total of 4 g of paraformaldehyde (PFA) was dissolved in approximately 80 mL of 1× PBS by heating to 60 °C with stirring. After cooling to room temperature, the solution was adjusted to a final volume of 100 mL with 1× PBS, filtered through a 0.22 µm filter, and stored at 4 °C.

0.2% Triton X-100 solution:

A total of 20 µL of 10% Triton X-100 stock solution was diluted with 1× PBS to a final volume of 1 mL to obtain a 0.2% working solution. The solution was stored at 4 °C.

5% BSA blocking solution:

A total of 2.5 g of BSA was dissolved in 1× PBS to a final volume of 50 mL to obtain a 5% (w/v) blocking solution. The solution was stored at 4 °C

DAPI stain:

DAPI stock solution was diluted 1:500 in 1× PBS to obtain the working solution. The working solution was stored at 4 °C protected from light.

2.8.2 Primary and secondary antibodies

Table 4. Primary antibodies used for Immunofluorescence

Name	Host	Dilution	Art. No	Manufacturer, Country
CXCR4	Rabbit	1:100	11073-2-AP	Proteintech, USA
Iba1	Rabbit	1:100	ab178846	Abcam, UK
GSDMD	Rabbit	1:100	PA5-115330	Thermo Scientific, USA

Table 5. Secondary antibodies used for Immunofluorescence

Name	Host	Dilution	Art. No	Manufacturer, Country
Anti-Rabbit Alexa Fluor™ 488	Goat	1:500	A-11008	Thermo Scientific, USA

2.8.3 Experimental procedure

1) Preparation of coverslips: sterile coverslips were placed in 24-well plates. Primary microglia were seeded at a density of 20,000 cells per well and cultured for 1-2 days under standard conditions.
2) Fixation: cells were washed three times with ice-cold 1× PBS (30 s each) and fixed with 500 µL of 4% PFA per well for 10 min at room temperature, followed by three ice-cold 1× PBS washes (30 s each).
3) Permeabilization: cells were permeabilized with 500 µL of 0.2% Triton X-100 per well for 10 min at room temperature, followed by three ice-cold 1× PBS washes (30 s each).
4) Blocking: cells were blocked with 500 µL of 5% BSA per well for 30 min at room temperature.

5) Primary antibody incubation: a sealing film was prepared with drops (20 μL) of diluted primary antibodies. Coverslips were carefully inverted onto the antibody drops and incubated overnight at 4 °C in a humidified chamber. From the next step onwards, all procedures were performed under light-protected conditions.
6) Secondary antibody incubation: after three ice-cold 1× PBS washes, cells were incubated with diluted fluorescent secondary antibody solution for 1 h at room temperature in the dark, followed by three ice-cold 1× PBS washes.
7) DAPI nuclear staining: cells were incubated with diluted DAPI solution for 1 min at room temperature, followed by three ice-cold 1× PBS washes.
8) Mounting: slides were labeled with antibody information, cell type, date, and researcher's name. A total of 3 μL of ProLong™ Glass Antifade Mountant was added to the slide, and coverslips were inverted onto the mounting medium. Slides were stored at 4 °C until imaging.

2.9 Western Blot Analysis

2.9.1 Preparation of solutions

10% SDS solution:

A total of 10 g of SDS powder was dissolved in ddH_2O to a final volume of 100 mL. The solution was stirred and gently heated to facilitate dissolution, allowed to cool to room temperature, and stored at room temperature.

10% Ammonium Persulfate (APS):

A total of 1 g of ammonium persulfate (APS) was dissolved in 10 mL of ddH_2O to obtain a 10% (w/v) stock solution. The solution was mixed thoroughly, aliquoted into 1.5 mL tubes, and stored at 4 °C.

RIPA buffer (with inhibitors):

Pierce™ RIPA buffer was supplemented with one protease inhibitor cocktail tablet per 50 mL of buffer (final 1× concentration) and phosphatase inhibitor cocktail at a final 1× concentration (1:100 dilution from the 100× stock). The supplemented buffer was freshly prepared prior to use and kept on ice during protein extraction.

1× SDS-PAGE Running Buffer (1 L):

A total of 100 mL of Rotiphorese® 10× SDS-PAGE Running Buffer was diluted with 900 mL of ddH_2O to a final volume of 1 L.

SDS-PAGE Transfer Buffer (1 L):

A total of 100 mL of Rotiphorese® 10× SDS-PAGE Running Buffer, 200 mL of methanol, and 700 mL of ddH_2O were mixed thoroughly to a final volume of 1 L.

20× TBS:

A total of 48.2 g of Tris base and 175.4 g of NaCl were dissolved in ddH_2O and adjusted to a final volume of 1 L. The pH was adjusted to 7.2-7.6.

1× TBS-T (0.1% Tween-20):

A total of 50 mL of 20× TBS, 950 mL of ddH_2O, and 1 mL of Tween-20 were combined and mixed thoroughly to a final volume of 1 L.

5% Milk:

Nonfat dry milk powder was dissolved in 1× TBS-T to a final concentration of 5% (w/v). The solution was freshly prepared prior to use.

2.9.2 Primary and secondary antibodies

Table 6. Primary antibodies used for Western Blot

Name	Host	Dilution	Art. No	Manufacturer, Country
β-actin	Rabbit	1:5000	ab8227	Abcam, UK
CXCR4	Rabbit	1:1000	11073-2-AP	Proteintech, USA
GSDMD	Rabbit	1:500	PA5-115330	Thermo Scientific, USA

Table 7. Secondary antibodies used for Western Blot

Name	Host	Dilution	Art. No	Manufacturer, Country
Goat Anti-Rabbit IgG H&L (HRP)	Goat	1:10000	ab6721	Proteintech, USA

2.9.3 Preparation of 10% SDS-PAGE gels

1) Preparation of glass plates: glass plates were assembled in the casting frame with spacers to prevent leakage. Water was filled between the plates to check for tightness, then removed and the space was dried with lint-free paper before pouring the gel.
2) Running gel preparation: for two gels, ddH_2O (6.6 mL), 1.5 M Tris-HCl (pH 8.8, 5 mL), and 10% SDS (200 µL) were mixed. Immediately before pouring, acrylamide (6.6 mL),

10% APS (200 µL), and TEMED (20 µL) were added. The solution was poured between the glass plates up to the first marker line of the casting frame. A thin layer of methanol was gently overlaid to avoid drying. After polymerization, the methanol was removed, the surface was rinsed with ddH_2O, and dried with lint-free paper.

3) Stacking gel preparation: for two gels, ddH_2O (6.8 mL), 0.5 M Tris-HCl (pH 6.8, 1.25 mL), and 10% SDS (100 µL) were mixed. Immediately before pouring, acrylamide (1.7 mL), 10% APS (100 µL), and TEMED (10 µL) were added. The stacking gel solution was layered on top of the polymerized running gel, and a comb was inserted to form wells. After polymerization, the comb was removed. If not used immediately, gels were wrapped in wet paper towels soaked with ddH_2O and stored at 4 °C.

2.9.4 Protein extraction and quantification

1) Cell harvesting and lysis: following the OGD/RO treatment, cells were washed twice with ice-cold 1× PBS to remove residual medium and debris. Adherent cells were scraped off using a cold plastic cell scraper and transferred into pre-cooled 1.5 mL microcentrifuge tubes. The suspensions were centrifuged at 3000 × g for 5 min at 4 °C, and the supernatants were discarded. Cell pellets were lysed in RIPA buffer (with inhibitors) and incubated on ice for 30 min with vortexing every 5 min to facilitate lysis. To further disrupt the cells, sonication was performed for 30 s on ice, followed by an additional 30 min of incubation on ice.
2) Protein extraction: the lysates were centrifuged at 12,000 × g for 20 min at 4 °C, and the supernatants, containing the extracted proteins, were collected and stored at -80 °C until further analysis.
3) Protein quantifications were determined using the DC™ Protein Assay Kit according to the manufacturer's instructions. A standard curve was prepared using BSA (0–1.4 µg/µL). Cell lysates and standards (5 µL, in duplicate) were mixed with 25 µL of Reagent A + S mixture (A:S = 50:1) in a 96-well plate, followed by the addition of 200 µL of Reagent B. The plate was protected from light and placed on an orbital shaker at 50 rpm to ensure thorough mixing. Absorbance was measured at 750 nm using a microplate reader. Protein concentrations were calculated from the standard curve, and all samples were adjusted to equal concentrations using RIPA buffer.

4) Sample preparation for electrophoresis: protein samples were mixed with reducing loading buffer at a volume ratio of 4:1 and heated at 95 °C for 9 min to denature proteins prior to SDS-PAGE.

2.9.5 Western blotting procedure

1) Electrophoresis chambers were assembled and filled with running buffer. The combs were carefully removed, and protein marker (5 μL) together with protein samples (10-40 μg) were loaded into the wells. Electrophoresis was performed at 90 V for 30 min, followed by 120 V for 90 min.
2) PVDF membranes (0.45 μm, cut to the size of the gel, approximately 5 × 7 cm) were activated by soaking in methanol for 1 min. Membranes and filter papers were equilibrated in transfer buffer. The transfer sandwich was assembled in the cassette of the Trans-Blot® SD Transfer System in the following order: filter paper, membrane, gel, and filter paper. Air bubbles were removed by gently rolling after each step. Protein transfer was carried out at 25 V and 1.5 A for 30 ± 15 min, depending on protein size.
3) After transfer, membranes were washed once with TBS-T for 5 min on a shaker and incubated in blocking solution (5% nonfat milk in TBS-T) for 1 h at room temperature with gentle agitation.
4) For primary antibody incubation, membranes were incubated overnight at 4 °C with primary antibodies. Following three washes in TBS-T (15 min each), membranes were incubated for 1 h at room temperature with secondary antibody. After incubation, membranes were washed again three times in TBS-T (15 min each).
5) For chemiluminescent detection, ECL solution was prepared by mixing Reagent A and Reagent B at a 1:1 ratio. Membranes were incubated with the ECL solution for 5 min in the dark, covered with protective plastic film, and visualized using the ChemoCam Imager ECL System.

2.10 Data processing, analysis, and statistics

2.10.1 MTT cell viability assay

Cell viability was calculated relative to the normoxic control, which was set as 100%. Values for the hypoxic and treatment groups were expressed as percentages of this control. Data were analyzed using one-way ANOVA to assess differences among experimental groups. The assumption of homogeneity of variance was tested using both the Brown–Forsythe and Bartlett's tests, neither of which indicated significant variance differences ($P > 0.05$). When ANOVA revealed a significant effect, Dunnett's multiple comparisons test was applied to compare each OGD/RO group with the normoxic control, as well as to compare OGD/RO groups with treatment groups. Adjusted P values were reported, and statistical significance was set at $\alpha = 0.05$. All statistical analyses were performed using GraphPad Prism 9 (GraphPad Software, San Diego, USA).

2.10.2 Immunofluorescence

Fluorescence images were acquired using identical exposure settings across all experimental groups. Images were exported as 16-bit TIFF files and analyzed in Fiji/ImageJ (NIH, USA). For each image, the total fluorescence intensity of the target signal was measured and divided by the corresponding number of cells (determined from DAPI staining) to obtain the average fluorescence intensity per cell. Normalized fluorescence intensities were expressed relative to the mean of the normoxic control (set to 1.00) to yield fold-of-control, and data were presented as mean ± SD. Data from multiple fields ($n \geq 3$ per group) were averaged to represent each biological replicate.

Average fluorescence intensities were analyzed in GraphPad Prism 9. When only two experimental conditions were compared, a paired t-test was used. When three or more groups were compared, a one-way ANOVA was performed, followed by appropriate post hoc tests (e.g., Dunnett's test for comparison with a control, or Tukey's test for pairwise comparisons). Statistical significance was defined at $\alpha = 0.05$.

2.10.3 Western blotting

Blots were exposed within the linear dynamic range (no saturated pixels) and exported as 16-bit TIFF files with identical exposure settings across groups within an experiment. Band intensities were quantified in Fiji/ImageJ (NIH, USA) as follows: (i) images were left unmodified except for conversion to 8-bit when required; (ii) lanes were defined using the Gel Analyzer tool with a constant lane width for all samples; (iii) background was removed by baseline correction of each lane profile and by subtracting a local background ROI adjacent to each band; (iv) the integrated density was recorded for both the target protein and the loading control (β-actin). For each lane, target signals were normalized to β-actin (target/β-actin). Normalized values were then expressed relative to the mean of the normoxic control (set to 1.00) to yield fold-of-control. When multiple blots were required, each blot was normalized to its own control prior to pooling. Data are presented as mean ± SD; the sample size for Western blots was n = 3 per group unless otherwise stated.

Normalized band intensities were analyzed using one-way ANOVA. Homogeneity of variance was tested with the Brown–Forsythe and Bartlett's tests, which confirmed variance equivalence ($P > 0.05$). When ANOVA revealed significant differences, appropriate post hoc tests were performed (e.g., Dunnett's test for comparisons with a control, or Tukey's test for pairwise comparisons). Adjusted P values were reported, and statistical significance was set at $\alpha = 0.05$. Analyses were carried out in GraphPad Prism.

3 RESULTS

3.1 Study design and workflow

The aim of this study was to determine whether CXCR4 contributes to microglial pyroptosis after ischemia–reperfusion, using a four-step workflow that links in-silico discovery to in-vitro validation. First, a mechanistic hypothesis was defined that chemokine signaling through the CXCL12–CXCR4 axis couples guidance cues to inflammasome activation and GSDMD processing in post-ischemic microglia. Second, publicly available bulk RNA sequencing of FACS-purified microglia three days after transient MCAO with reperfusion (GSE220042; three MCAO and three sham samples) was reanalyzed to identify differential expression and enriched pathways related to CXCR4. Third, a brain-wide single-cell RNA sequencing dataset collected at 24 hours after MCAO or sham (GSE174574; three MCAO and three sham samples) was integrated with batch correction to define cell types and microglial states; cluster markers were derived with FindAllMarkers, module scores for the CXCR4 axis and for pyroptosis activation, execution, and composite programs were computed, condition-stratified correlations were tested, and a cluster-wise network-based virtual CXCR4 knockout was performed to infer CXCR4 dependence of pyroptosis programs. Fourth, primary microglia were subjected to oxygen–glucose deprivation followed by reoxygenation, CXCR4 was pharmacologically blocked with AMD3100, and viability, western blotting, and immunofluorescence readouts for CXCR4 and GSDMD were acquired to validate bioinformatic findings.

3.2 Bioinformatic analysis of CXCR4 in mouse brain after ischemia–reperfusion

3.2.1 Bioinformatic database search and study selection

A structured search of the GEO database identified mouse datasets relevant to microglial responses after ischemia–reperfusion. The query string was: “microglia[All Fields] AND (“ischemia-reperfusion” OR “ischemia reperfusion” OR “ischemic stroke” OR stroke OR “middle cerebral artery occlusion” OR MCAO OR tMCAO) AND “Mus musculus”[Organism] AND “expression profiling by high throughput sequencing”[DataSet Type]”. The

search targeted both bulk RNA-seq and single-cell RNA-seq resources. Inclusion required sham and experimental groups each with at least three biological replicates, explicit reporting of surgical method, ischemia duration, and reperfusion duration, and the availability of analyzable files. Datasets were excluded if they modeled ischemia without reperfusion or lacked usable data files, defined as missing raw count tables for bulk RNA-seq or missing barcode, feature, and matrix files for each sample in single-cell studies. The search cutoff date was 1 October 2025 and returned 62 records. After screening against the prespecified criteria, two datasets met eligibility for analysis: GSE220042 for microglial bulk RNA-seq and GSE174574 for brain-wide single-cell RNA-seq.

3.2.2 RNA sequencing analysis of CXCR4 in microglia after ischemia–reperfusion

Publicly available RNA sequencing (RNA-seq) data from GEO (GSE220042) were analyzed, in which a 60-min middle cerebral artery occlusion (MCAO) was used to induce transient focal cerebral ischemia (tFCI) in mice, followed by 3 days of reperfusion (Y. Zhang et al., 2024). At this time point, microglia were isolated by fluorescence-activated cell sorting as $CD11b^{+}/CD45^{int}$, and bulk RNA-seq of the purified population was generated (Figure 4). All animal procedures and sequencing were conducted by the original authors, while downstream analyses were performed in the present study. The two-column HTSeq-count files provided in GEO (Ensembl gene IDs and raw counts) from three sham and three MCAO samples were analyzed in this research.

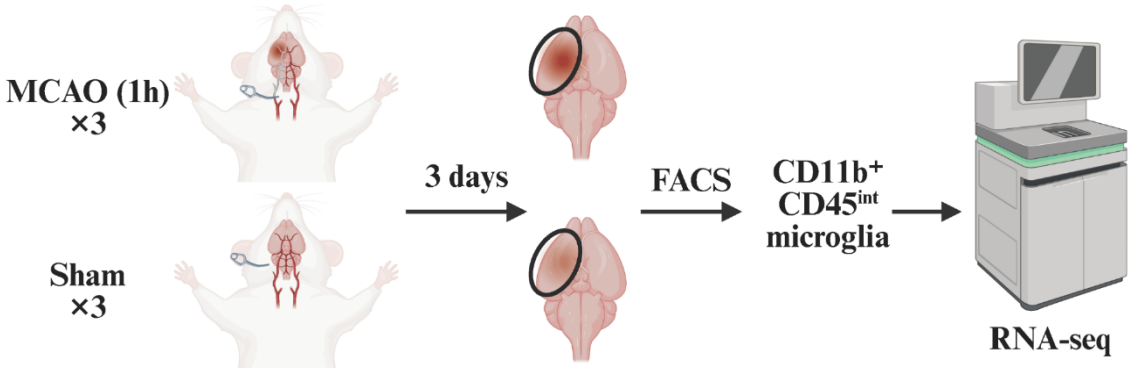

Figure 4. Workflow for RNA-seq in mouse microglia after ischemia-reperfusion.
Transient focal cerebral ischemia was induced by 60-min MCAO, followed by 3 days of reperfusion. Microglia were purified by FACS as $CD11b^{+}/CD45^{int}$ and subjected to bulk RNA-seq. The dataset

comprises 3 MCAO and 3 sham samples. Count data analyzed in this study were obtained from the public GEO accession GSE220042. The schematic was created with BioRender.

Principal component analysis (PCA) resolves the two conditions along PC1 (38.4% variance): MCAO samples score positively and sham samples score negatively, with no overlap. PC2 (19.1%) captures within-group dispersion in both conditions. No outliers are observed. Overall, the first two components organize the data primarily by ischemic-reperfusion status, indicating marked transcriptomic differences between MCAO and sham microglia (Figure 5A). Using the predefined threshold (adjusted $P < 0.05$ and $|\log_2FC| > 1$), the analysis identifies 3166 differentially expressed genes (DEG), including 2463 up-regulated and 703 down-regulated transcripts. Up-regulated genes show larger effect sizes overall ($\log_2FC$ range +1.00 to +11.16, median +2.87; 1659 genes with $\log_2FC \geq 2$), whereas down-regulated genes display smaller shifts on average ($\log_2FC$ range −6.83 to −1.00, median −1.33; 112 genes with $\log_2FC \leq -2$). CXCR4 is significantly upregulated in microglia after ischemia–reperfusion relative to sham ($\log_2FC = 2.88$; padj = 5.58×10^{-4}). Meanwhile, the transcript for the proinflammatory cytokine Il1b shows an even greater increase ($\log_2FC = 3.57$; padj = 6.96×10^{-82}) (Figure 5B).

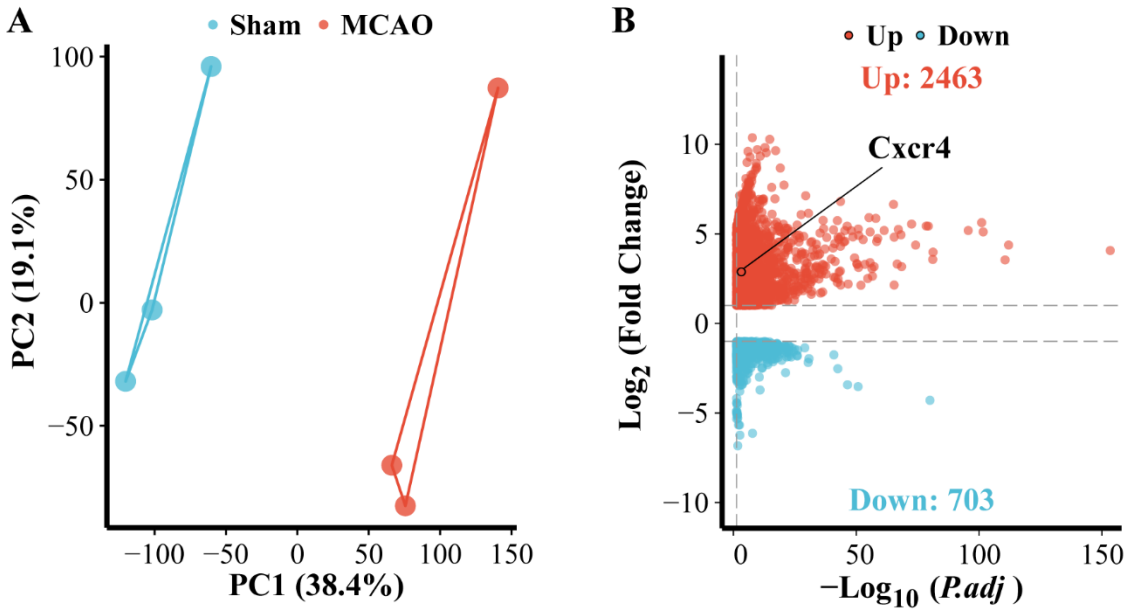

Figure 5. PCA and volcano plot of RNA-seq in mouse microglia after ischemia-reperfusion.
A. Principal component analysis separates MCAO and sham along PC1 (38.4% variance), while PC2 (19.1%) reflects within-group dispersion. Each point represents one library; n = 3 per group, PC1

and PC2 denote the first two principal components—orthogonal linear combinations of gene expression that capture the largest and second-largest proportions of variance, respectively; axis values represent sample scores; **B.** Volcano plot for MCAO vs. sham using adjusted $P < 0.05$ and $|\log_2 FC| > 1$. Up-regulated genes, 2463; down-regulated genes, 703. CXCR4 and Il1b are among the significantly up-regulated transcripts.

Functional enrichment of DEGs induced in microglia after MCAO identifies significant terms across Gene Ontology Biological Process (BP), Cellular Component (CC), Molecular Function (MF), and Kyoto Encyclopedia of Genes and Genomes (KEGG) pathways. Statistical significance is defined as $p < 0.05$ with Benjamini–Hochberg–adjusted p (padj) < 0.10. For each term, a directionality z score was computed from the gene-wise $\log_2$ fold changes of its members. Positive z scores indicate a predicted positive regulation (activation/up-shift of the term), whereas negative z scores indicate negative regulation (suppression/down-shift). Among significant terms that contain CXCR4 (n = 145; Biological Process 119, Molecular Function 14, Cellular Component 6, KEGG 6), z-scores are uniformly positive from 0.71 to 8.77, indicating pathway activation three days after reperfusion (Figure 6). Enrichments converge on a program centered on microglial motility and chemokine-driven signaling. Biological Process terms emphasize migration and vascular remodeling, including ameboidal type cell migration (GO:0001667), cell chemotaxis (GO:0060326), regulation of angiogenesis (GO:0045765), regulation of vasculature development (GO:1901342), and gliogenesis (GO:0042063). Cellular Component terms map to structures for movement and receptor trafficking, including the cell leading edge (GO:0031252), growth cone (GO:0030426), distal axon (GO:0150034), site of polarized growth (GO:0030427), and early endosome (GO:0005769), consistent with ligand-dependent CXCR4 internalization and recycling. Molecular Function terms highlight actin binding (GO:0003779), cytokine binding (GO:0019955), chemokine binding (GO:0019956), cytokine receptor activity (GO:0004896), and immune receptor activity (GO:0140375). KEGG pathways are led by cytokine and cytokine receptor interaction (mmu04060) and chemokine signaling (mmu04062), capturing shared signaling and guidance networks. Taken together, the enrichment landscape that contains CXCR4 is uniformly positive and centers on microglial motility, cytoskeletal remodeling, and chemokine-driven signaling three days after reperfusion. Biological processes associated with migration and vascular remodeling suggest that microglia are poised to move toward peri-infarct cues while engaging in glial reorganization. Cellular component terms at

the leading edge, growth cone, and early endosome indicate coordinated actin dynamics and receptor trafficking, compatible with ligand-dependent CXCR4 internalization and recycling that can sustain CXCL12–CXCR4 signaling and directional sensing. Molecular functions enriched for actin binding and cytokine or chemokine receptor activity are consistent with this adhesive and chemotactic phenotype. Together with the increased CXCR4 and Il1b transcripts, these results support a model in which microglia adopt a chemokine-responsive, migratory state after ischemia-reperfusion.

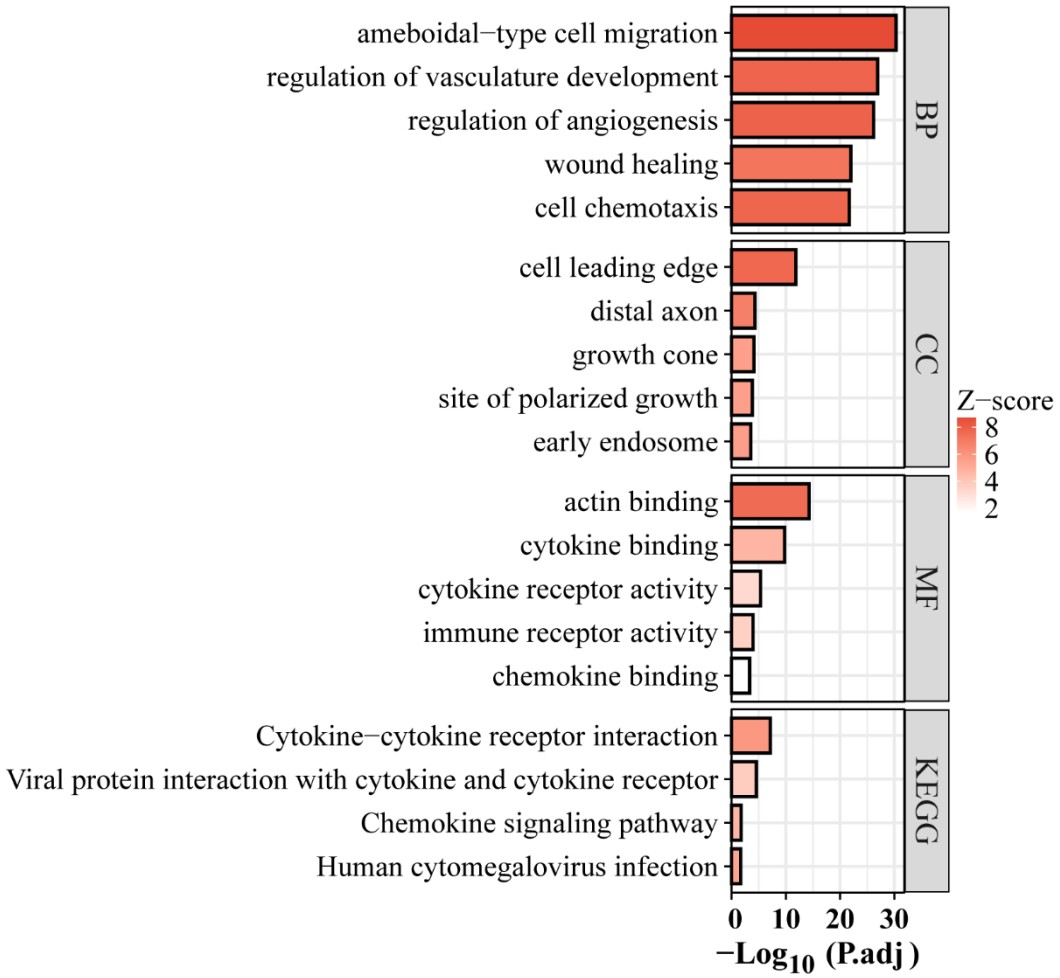

Figure 6. Enrichment terms involving CXCR4 in microglia after ischemia-reperfusion.
Bars show the top significant terms (up to five) in each category: Biological Process (BP), Cellular Component (CC), Molecular Function (MF), and Kyoto Encyclopedia of Genes and Genomes pathways (KEGG), for the comparison between MCAO and sham microglia (n = 3 per group). Significance is defined as $p < 0.05$ and adjusted p (padj) < 0.10. The x axis displays -log10 (padj). Bar shading encodes the z score derived from member gene $\log_2$ fold changes. Positive values indicate predicted activation, and all terms shown have positive z scores.

To map the functional neighborhood of CXCR4, genes that co-occur with CXCR4 within significant enrichment terms were counted. The top ten co-occurring genes are shown in Figure 7, with Il1b ranking tenth (38 co-mentions). The top set also comprises the ligand Cxcl12, vascular and endothelial regulators (Vegfa, Edn1, Ednra), morphogen pathways (Bmp4, Wnt5a), growth factors (Igf1, Nrg1), and a kinase involved in cytoskeletal control (Abl1). This constellation places CXCR4 within chemotactic, cytoskeletal, and vascular-cue programs that are expected after MCAO.

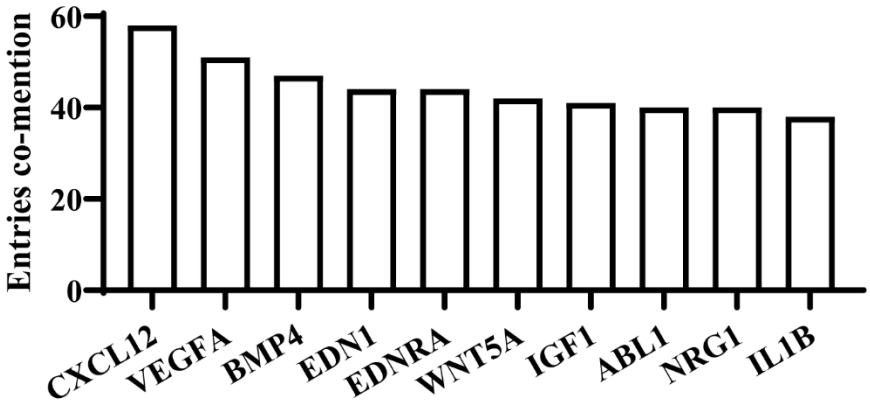

Figure 7. Top co-occurring DEGs with CXCR4 across enriched terms in MCAO microglia. Bars show the top ten genes that most frequently co-occur with CXCR4 among significant enrichment terms from the MCAO versus sham comparison of microglia three days after reperfusion.

In the context of ischemia–reperfusion and pyroptosis, the frequent co-mention of Il1b with CXCR4 is compatible with a milieu in which CXCL12–CXCR4 signaling intersects inflammatory cytokine production and receptor trafficking. Vascular and morphogen signals may further shape microglial positioning and sensitivity to inflammatory activation. The 38 significant enriched terms that include both Il1b and CXCR4 are listed in Table 8**.** These terms converge on a coherent program centered on microglial motility and chemokine driven signaling. Specifically, migration and vascular guidance are represented by regulation of vasculature development (GO:1901342), regulation of angiogenesis (GO:0045765), cell chemotaxis (GO:0060326), and gliogenesis (GO:0042063). Moreover, stimulus responsive signaling is supported by cytokine mediated signaling pathway (GO:0019221), positive regulation

of response to external stimulus (GO:0032103), and the ERK1/ERK2 cascade and its regulatory nodes (GO:0070371, GO:0070372, GO:0070374), together with the KEGG term Cytokine and cytokine receptor interaction (mmu04060).

Table 8. CXCR4 and Il1b co-mentioned enriched terms after ischemia-reperfusion.

ID	Description	p.adjust	qvalue
GO:1901342	regulation of vasculature development	1.15E-27	5.74E-28
GO:0045765	regulation of angiogenesis	6.33E-27	3.15E-27
GO:0060326	cell chemotaxis	1.99E-22	9.87E-23
GO:0042063	gliogenesis	2.75E-22	1.37E-22
GO:0032103	positive regulation of response to external stimulus	6.58E-19	3.27E-19
GO:0050920	regulation of chemotaxis	1.05E-17	5.2E-18
GO:0001763	morphogenesis of a branching structure	6.28E-17	3.12E-17
GO:0045766	positive regulation of angiogenesis	6.28E-17	3.12E-17
GO:1904018	positive regulation of vasculature development	6.28E-17	3.12E-17
GO:0019221	cytokine-mediated signaling pathway	1.8E-16	8.96E-17
GO:0070371	ERK1 and ERK2 cascade	4.36E-16	2.17E-16
GO:0070372	regulation of ERK1 and ERK2 cascade	6.11E-15	3.04E-15
GO:0010720	positive regulation of cell development	5.5E-14	2.73E-14
GO:0050767	regulation of neurogenesis	7.69E-14	3.82E-14
GO:0061351	neural precursor cell proliferation	2.14E-13	1.06E-13
GO:0006874	cellular calcium ion homeostasis	2.7E-13	1.34E-13
GO:0050921	positive regulation of chemotaxis	3.54E-13	1.76E-13
GO:0070374	positive regulation of ERK1 and ERK2 cascade	5.26E-13	2.62E-13
GO:0003158	endothelium development	8.47E-13	4.21E-13
GO:0070661	leukocyte proliferation	4.08E-12	2.03E-12
GO:0010001	glial cell differentiation	5.76E-11	2.86E-11
GO:0032943	mononuclear cell proliferation	5.92E-11	2.94E-11
GO:0045446	endothelial cell differentiation	6.6E-11	3.28E-11
GO:0046651	lymphocyte proliferation	8.88E-11	4.41E-11
GO:0050769	positive regulation of neurogenesis	3.78E-10	1.88E-10
GO:0051480	regulation of cytosolic calcium ion concentration	4.53E-10	2.25E-10
GO:0051962	positive regulation of nervous system development	8.2E-10	4.07E-10
GO:0042098	T cell proliferation	3.52E-09	1.75E-09
GO:0007204	positive regulation of cytosolic calcium ion	1.41E-08	7.03E-09
GO:0043270	positive regulation of ion transport	5.13E-08	2.55E-08
GO:0002064	epithelial cell development	9.2E-08	4.57E-08
GO:0001659	temperature homeostasis	4.23E-06	2.1E-06
GO:0014013	regulation of gliogenesis	1.39E-05	6.92E-06
GO:0014015	positive regulation of gliogenesis	2.54E-05	1.26E-05
GO:0045685	regulation of glial cell differentiation	0.001492	0.000742
GO:0045687	positive regulation of glial cell differentiation	0.011034	0.005484
mmu04060	Cytokine-cytokine receptor interaction	7.22E-08	5.06E-08
mmu05163	Human cytomegalovirus infection	0.021746	0.015237

To sum up, differential expression shows widespread changes dominated by up-regulated transcripts, and CXCR4 and Il1b are up-regulated in mouse microglia after ischemia-reperfusion. Functional enrichment indicates CXCR4 involves in activation of chemotaxis, vascular remodeling, cytokine and chemokine signaling, cytoskeletal remodeling, and receptor trafficking. Co-occurrence analysis of CXCR4-containing terms places CXCR4 with its ligand Cxcl12, vascular and morphogen cues, trophic factors, and a cytoskeletal kinase, with Il1b among the top partners. Collectively, these findings support a chemokine-responsive, migratory microglial state after reperfusion, with CXCR4 contributing to this program.

3.2.3 Single-cell RNA sequencing analysis of CXCR4 in ischemia–reperfusion

Based on the bulk microglial RNA-seq findings after ischemia-reperfusion, a public single-cell RNA sequencing (scRNA-seq) dataset (GSE174574) was analyzed to resolve cell-type specificity and within-microglia heterogeneity at an earlier time point. In this dataset, mouse brains were collected 24 hours after MCAO or sham surgery, were dissociated into single-cell suspensions, and were profiled by scRNA-seq (Figure 8). This analysis separates microglia from other brain cell types, resolves subcluster structure within microglia, and quantifies chemokine-signaling and pyroptosis-related gene programs at single-cell resolution, thereby linking bulk-level features to specific microglial subsets.

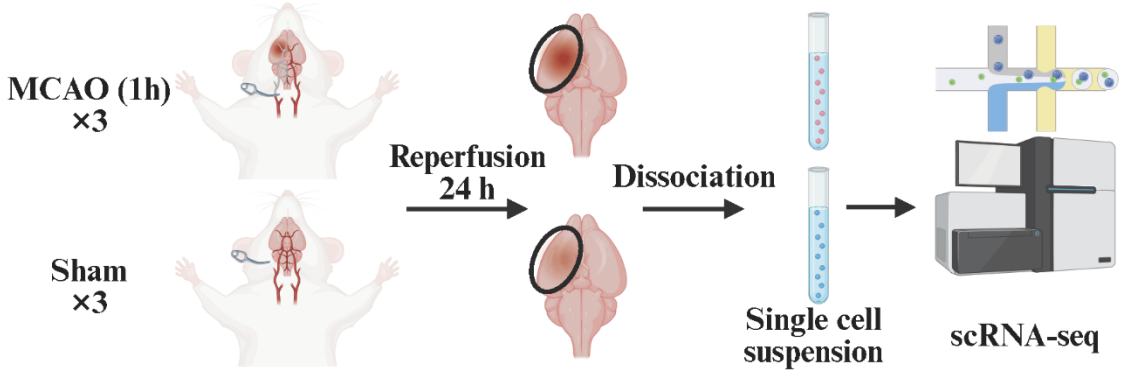

Figure 8. Workflow for scRNA-seq in the mouse brain after ischemia-reperfusion.
Transient focal cerebral ischemia was induced by 60-min MCAO, followed by 24 h of reperfusion. Brains were dissociated to single-cell suspensions and profiled by scRNA-seq. The dataset comprises three MCAO and three sham samples. Raw cell-by-gene count matrices and the associated barcode and feature index files for each sample were downloaded from GEO (GSE174574) and analyzed in this study. The schematic was created with BioRender.

After condition-aware integration to correct batch effects among replicates, the UMAP embedding shows well-mixed cells within each condition and organizes primarily by cell type rather than batch, while biological differences between MCAO and sham are retained (Figure 9A). Clusters are annotated as major brain cell types, including microglia, infiltrating macrophages, endothelial cells, astrocytes, oligodendrocytes, oligodendrocyte precursor cells (OPCs), ependymal cells, pericytes, smooth-muscle cells, B cells, and NK cells (Figure 9B). Marker expression illustrates these identities (Figure 9C), including microglial markers P2ry12, Tmem119, Cx3cr1; infiltrating-macrophage markers Lyz2, Ms4a7, S100a8, S100a9; endothelial markers Pecam1, Cldn5, Kdr; astrocyte markers Gfap, Aqp4; OPC markers Pdgfra, Cspg4; oligodendrocyte markers Mbp, Plp1; pericyte markers Pdgfrb, Rgs5; and smooth-muscle markers Acta2, Tagln.

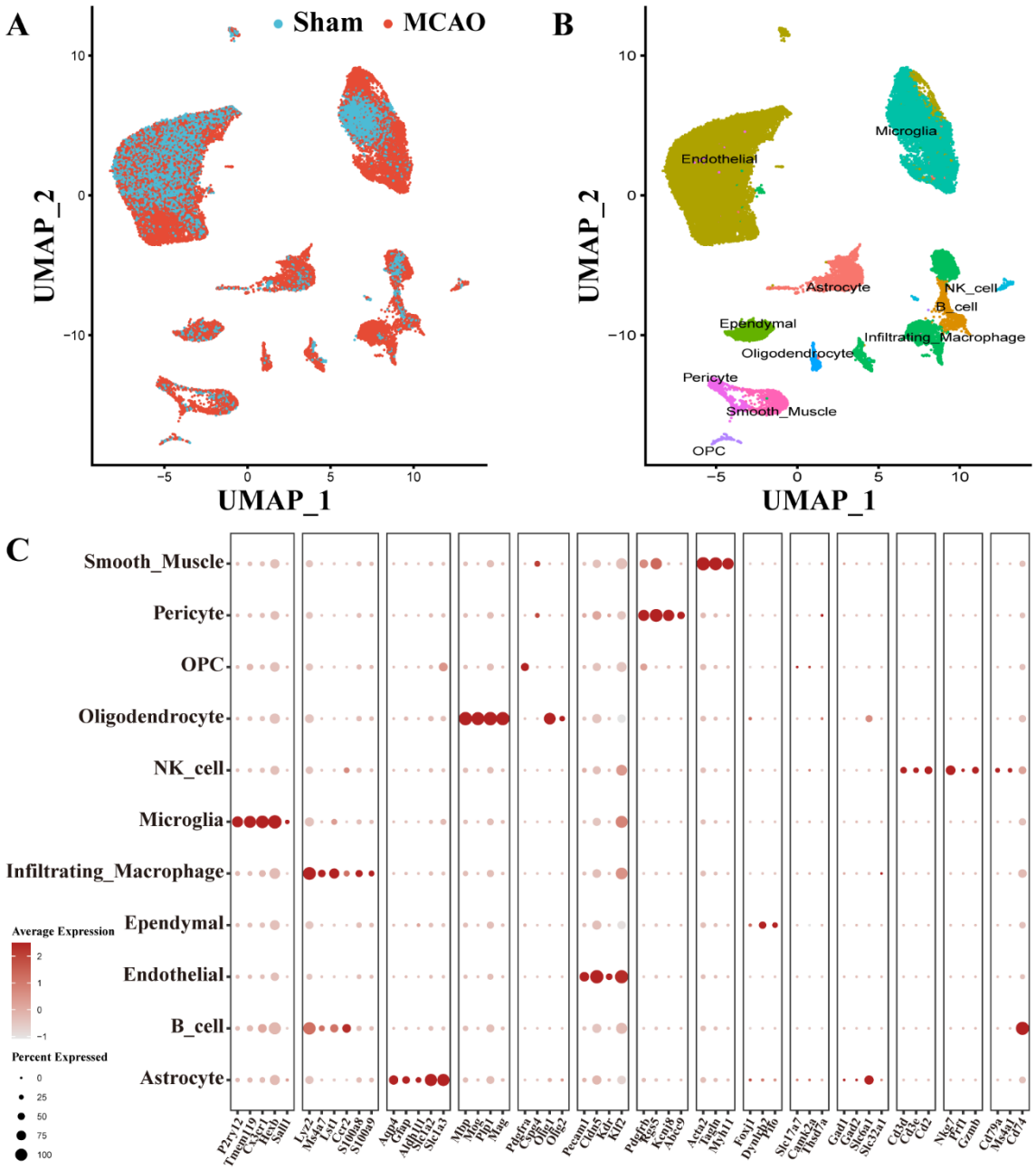

Figure 9. Single-cell landscape of the mouse brain after ischemia-reperfusion.
A. UMAP after condition-aware integration. Batch effects among replicates were corrected while ischemia–reperfusion biology was preserved. Cells from MCAO and sham are well mixed without artifactual condition segregation; **B.** UMAP annotated to major brain cell types: microglia, infiltrating macrophage, endothelial, astrocyte, oligodendrocyte, oligodendrocyte precursor cell (OPC), ependymal, pericyte, smooth-muscle, B cell, and NK cell.; **C.** Dot plot of canonical markers supporting annotations. Data comprise 3 MCAO and 3 sham samples collected 24 h after a 60-min MCAO or sham procedure.

Cell-composition analysis of 26472 cells in MCAO group and 21806 cells in sham group shows that endothelial cells remain the largest compartment in both conditions but decline

after ischemia-reperfusion (44.5% vs 60.8%). Microglia also decrease (22.0% vs 26.9%), whereas infiltrating macrophages expand (10.7% vs 4.0%). Astrocytes (7.0% vs 2.6%), ependymal cells (3.9% vs 1.6%), pericytes (3.0% vs 1.0%), smooth-muscle cells (2.8% vs 0.9%), B cells (2.4% vs 1.2%), and oligodendrocytes (2.1% vs 0.2%) also increase.

Building on the brain-wide scRNA-seq composition analysis, microglia were subsetted and replicates were integrated for state-level profiling. The resulting UMAP shows a condition-associated shift (Figure 10A): microglia of sham group occupy a single basin, whereas microglia of MCAO group redistribute to distinct regions with limited overlap, consistent with multiple post-ischemic states. Unsupervised clustering resolves eight transcriptional states (0–7) (Figure 10B).

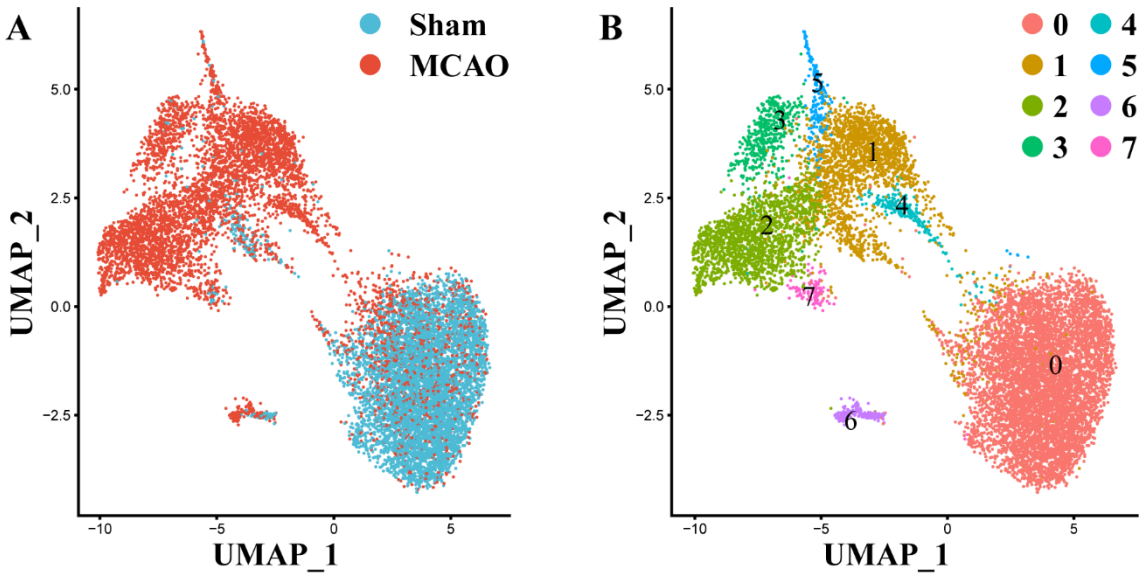

Figure 10. Microglial state structure after ischemia-reperfusion.
A. UMAP of microglia after condition-aware integration; **B.** Unsupervised clustering partitions microglia into eight transcriptional states (0–7). Each dot represents one cell

Within the microglial subset, cluster marker genes were derived with FindAllMarkers (Wilcoxon test with Benjamini–Hochberg adjustment), and top markers are selected by effect size and within-cluster prevalence (Figure 11).

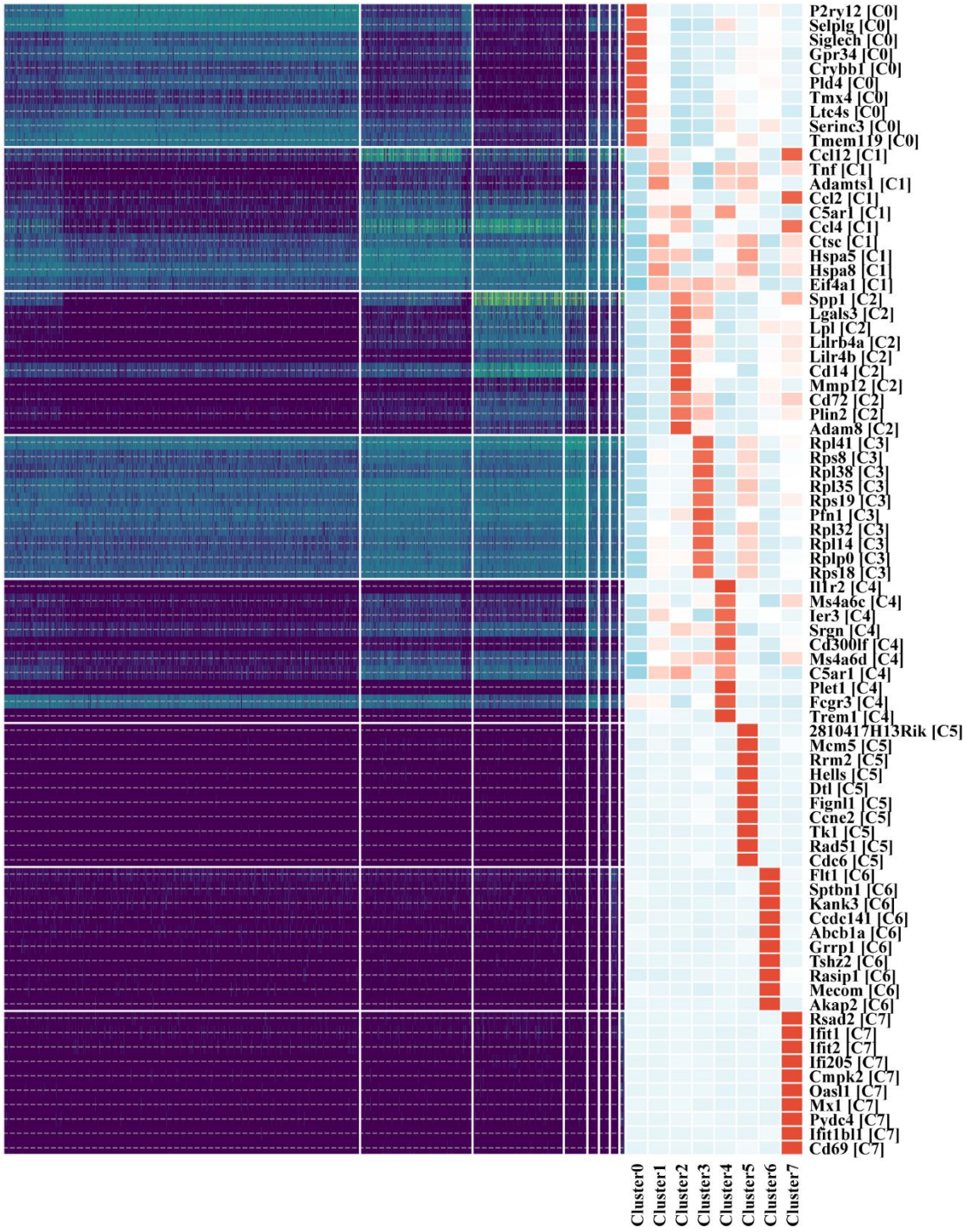

Figure 11. Cluster-specific marker genes of microglia after ischemia-reperfusion.
Heat map of top marker genes for eight microglial clusters. Vertical separators delineate clusters 0–7. Rows are the top markers per cluster identified with FindAllMarkers (Wilcoxon test with Benjamini–Hochberg adjustment). Left panel: log-normalized expression per cell. Right panel: per-cluster average expression after row-wise z score scaling to show relative specificity.

Cluster 0 represents homeostatic surveillant microglia marked by P2ry12 and Tmem119, together with phagosome and identity genes including Pld4 and Siglech, consistent with baseline surveillance. Cluster 1 shows a chemokine-rich inflammatory program with Ccl2, Ccl4, and Tnf, together with feedback modulators Socs3 and Gpr84, indicating cytokine and GPCR signaling that can recruit leukocytes and tune microglial activation. Cluster 2 exhibits an Spp1-positive phagocytic and lipid-handling state characterized by Spp1, Lgals3, Lpl, Cd14, and Plin2, which together point to enhanced debris recognition, lysosomal activity, and lipid clearance reminiscent of disease-associated microglia. Cluster 3 reflects a stress-responsive migratory phenotype with Lgals1 and Capg linked to actin remodeling, alongside chemokines Ccl5 and Ccl9, consistent with increased motility and guidance cue responsiveness. Cluster 4 indicates modulation of interleukin-1 signaling and stress adaptation, with Il1r2 acting as a decoy receptor for IL-1, Ms4a6 family members associated with microglial activation states, and immediate-early and cell-cycle checkpoint genes such as Ier3 and Cdkn1a, suggesting controlled responsiveness under stress. Cluster 5 captures a proliferative state dominated by cell-cycle and replication genes including Stmn1 and Mcm5, consistent with microglial expansion after injury. Cluster 6 shows a vascular-associated signature with Cldn5, Flt1, Slc2a1, and Ly6a, compatible with perivascular interaction or rare endothelial admixture and therefore interpreted cautiously. Cluster 7 displays a type I interferon–responsive program with Cxcl10, Ifit1/Ifit2, Rsad2, and Isg15, indicating antiviral and interferon-stimulated gene activity. Together, these states map a shift from homeostatic surveillance toward inflammatory, phagocytic, proliferative, interferon-responsive, and vascular-associated phenotypes in microglia after ischemia-reperfusion.

To define the ordering by which microglia differentiated into subtypes after ischemia–reperfusion, pseudotime analysis was performed on all microglial clusters in the MCAO group. Cluster 0 was fixed as the root since microglia of sham group predominantly localized in this cluster. Pseudotime analysis resolved a monotonic progression across MCAO microglia in the order $0 \rightarrow 4 \rightarrow 6 \approx 1 \rightarrow 5 \rightarrow 3 \rightarrow 2 \rightarrow 7$ (Figure 12A). Early cells in cluster 0 retained homeostatic surveillance features. Cells then moved to cluster 4, which showed regulation of interleukin-1 signaling and stress adaptation, indicating an initial controlled response to injury. Mid-trajectory comprised two components: cluster 1 displayed chemokine-rich inflammatory signaling with modulators of cytokine and GPCR pathways consistent with leukocyte

recruitment and tuning of activation, while cluster 6 exhibited a vascular-associated signature compatible with perivascular interaction or rare endothelial admixture and was interpreted cautiously. Proliferative programs dominated cluster 5, indicating microglial expansion, followed by a stress-responsive migratory phenotype in cluster 3 with cytoskeletal remodeling and chemokine cues consistent with directed movement toward injured regions. Late stages were represented by clusters 2 and 7: cluster 2 showed an Spp1-positive phagocytic and lipid-handling state with enhanced debris recognition, lysosomal activity, and lipid clearance, and cluster 7 showed a type I interferon–responsive program with interferon-stimulated genes. Notably, cluster 0 contained cells at both the earliest and the latest pseudotime, suggesting that a subset of microglia may have returned to a homeostatic-like transcriptional state after interim inflammatory, proliferative, migratory, and phagocytic–interferon programs (Figure 12B). Overall, the trajectory depicted a shift from baseline surveillance toward inflammatory, proliferative, migratory, phagocytic lipid-handling, and interferon-responsive states after ischemia–reperfusion, with a small vascular-associated branch in the mid-course.

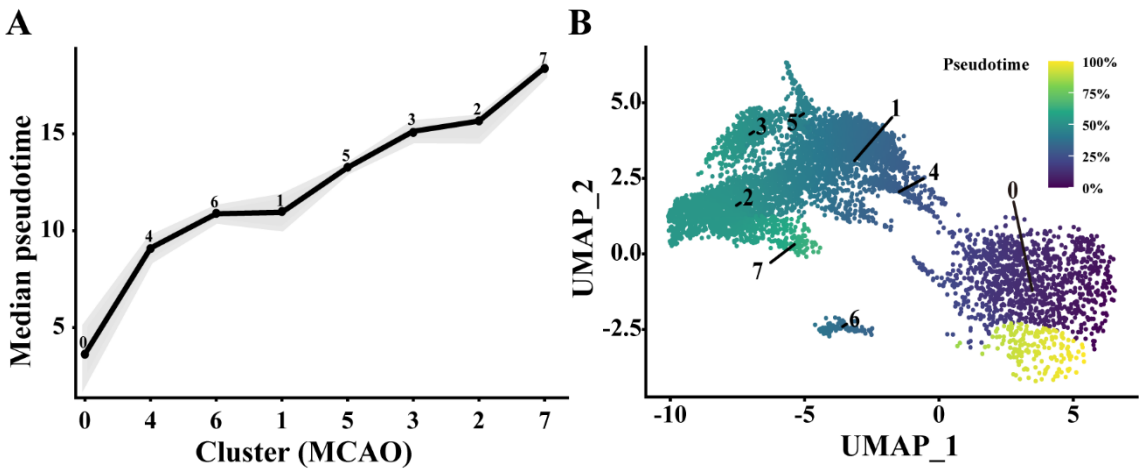

Figure 12. Pseudotime ordering of microglia after ischemia-reperfusion.
A. Median pseudotime by cluster for MCAO microglia. Median pseudotime denoted the fiftieth percentile of cell-level pseudotime within each cluster and summarized the typical stage of that cluster with robustness to outliers. The black line connected cluster medians and the grey ribbon showed within-cluster dispersion. Larger values indicated later positions along the inferred trajectory; **B.** UMAP of MCAO microglia colored by scaled pseudotime from 0 to 100. Numeric labels marked Seurat clusters and arrows marked their centroids. Cluster 0 served as the starting point because Sham cells predominated in this cluster. Only microglia from MCAO group were plotted. Pseudotime was inferred with Slingshot using UMAP coordinates and Seurat cluster labels, with cluster 0 set as the

root and values scaled by min–max scaling to a common range. Pseudotime reflected relative ordering rather than real time.

To quantify pyroptosis-related transcriptional programs in microglia, three pyroptosis gene sets were defined from the literature: an execution module (Casp1, Casp11, Gsdmd, Gsdme, Ninj1, Panx1), an activation module (Nlrp3, Nlrp1a, Nlrp1b, Nlrc4, Aim2, Pycard, Nek7, Txnip, Irf1, Stat1, Gbp2, Gbp5, Gbp7), and an overall module combining activation, execution, Il1b and Il18. Gene symbols were matched to the RNA assay, and per-cell module scores were then calculated with Seurat's AddModuleScore function, yielding "overall", "activation" and "execution" pyroptosis scores for each microglial cell. Using sham cluster 0 as the reference, each MCAO cluster (0-7) was contrasted at the cell level and sample level.

At the cell level, using sham microglia in cluster 0 as the reference, pyroptosis module scores show a non-uniform reorganization across MCAO clusters (Figure 13, A-C). The activation module is significantly reduced in MCAO clusters 0–6, with the largest decreases in the chemokine-rich inflammatory cluster (cluster 1), the $Spp1^{+}$ phagocytic/lipid-handling cluster (cluster 2), the stress-migratory cluster (cluster 3), the proliferative cluster (cluster 5), and the vascular-associated cluster (cluster 6). In contrast, the interferon-responsive cluster (cluster 7) displays higher activation and higher overall pyroptosis scores than sham cluster 0, whereas execution scores in this cluster are not significantly changed. For the execution module, the most pronounced reductions occur in the inflammatory (cluster 1) and proliferative (cluster 5) states, with other clusters showing only small or nonsignificant shifts relative to sham. Consequently, the overall pyroptosis score is significantly lower in MCAO clusters 1–6 and higher in cluster 7, while MCAO cluster 0 is only mildly reduced relative to the sham baseline.

When scores are aggregated to the sample level (three MCAO and three sham samples), the same pattern is recapitulated in the mean values for each cluster: MCAO groups corresponding to clusters 1–6 have lower activation and overall pyroptosis scores than sham cluster 0, whereas the MCAO group corresponding to the interferon-responsive cluster 7 shows higher activation and overall scores (Figure 14, A-C). Although formal significance is attenuated at the sample level because of the small number of samples, the direction and relative magnitude of the changes reinforce the cell-level finding that pyroptosis-related programs are

broadly dampened in most MCAO microglial states, with a selective enhancement in the interferon-driven cluster (cluster 7).

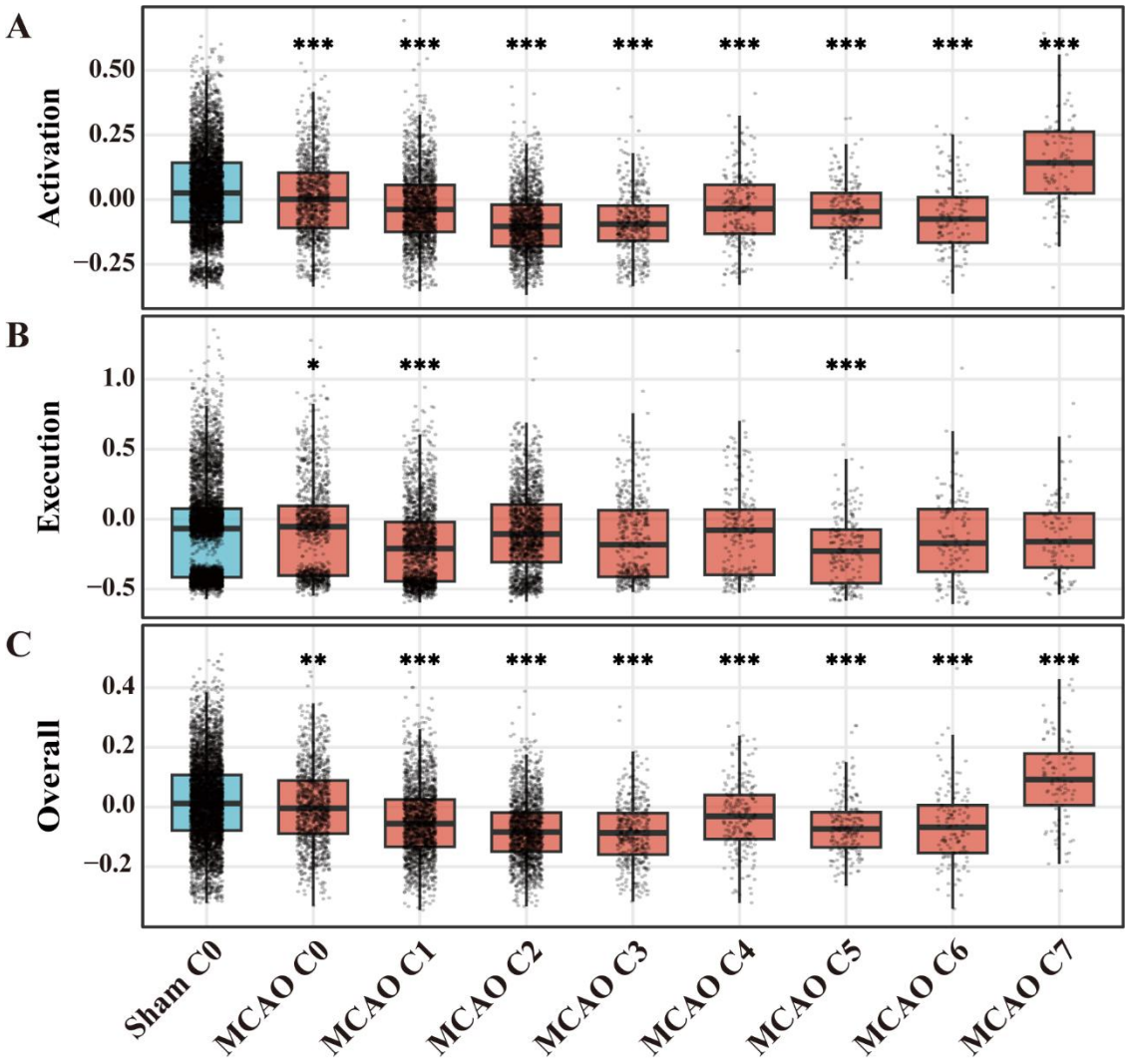

Figure 13. Cell-level pyroptosis scores of microglial clusters after ischemia-reperfusion.
Per-cell scores for the activation, execution, and overall pyroptosis modules (A–C) are shown for sham microglia in cluster 0 and MCAO microglia in clusters 0–7. Scores were computed by module scoring of predefined gene sets as described in Methods. Boxes show the interquartile range with median; points are individual cells. Colors indicate condition (sham, blue; MCAO, red). Group contrasts use the Wilcoxon rank-sum test with Benjamini–Hochberg adjustment relative to sham cluster 0. Significance is denoted as *** $p < 0.001$, ** $p < 0.01$, * $p < 0.05$.

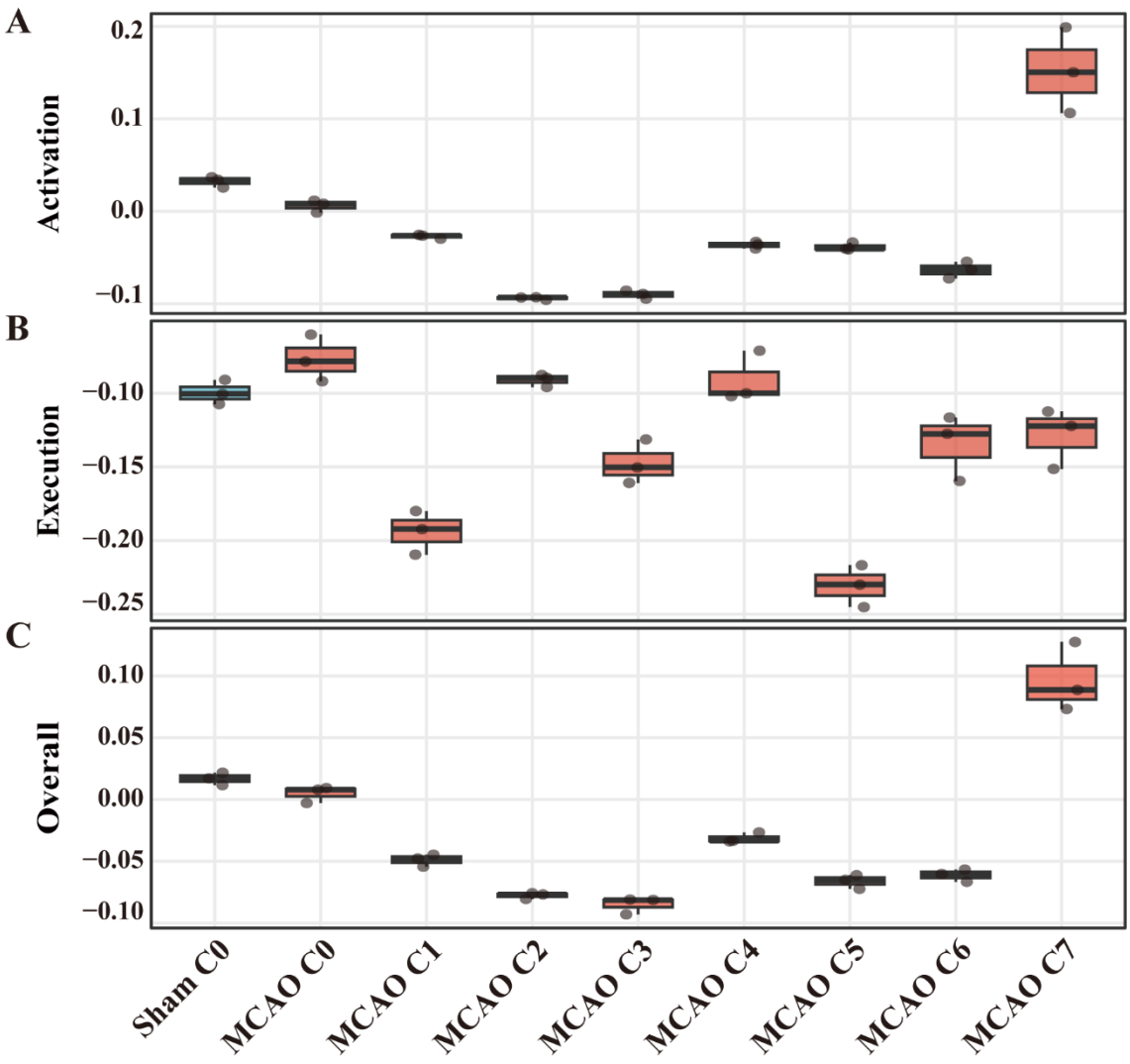

Figure 14. Sample-level pyroptosis scores of microglial clusters after ischemia-reperfusion. Per-sample means of the activation, execution, and overall pyroptosis modules (A–C) are shown for sham cluster 0 and MCAO clusters 0–7. Each dot represents one sample mean; boxes summarize between-sample variability. Only groups with sufficient cells per sample were included. The pattern observed at the cell level is recapitulated at the sample level, with higher values in cluster 7.

Axis score for the CXCL12–CXCR4 axis and three pyroptosis scores including the pyroptosis composite score, the pyroptosis activation score, and the pyroptosis execution score were computed with AddModuleScore on the batch-corrected microglial object, and Spearman correlations between CXCL12–CXCR4 axis score and each pyroptosis score were tested within all cells, the MCAO group, and the sham group with Benjamini–Hochberg correction (Figure 15). Across all microglia, CXCL12–CXCR4 axis shows a weak positive association with the pyroptosis composite score ($r = 0.074$, FDR = 9.05×10^{-15}) and smaller but significant

correlations with the pyroptosis activation score (r = 0.059, FDR = 3.54×10^{-9}) and the pyroptosis execution score (r = 0.036, FDR = 2.04×10^{-4}). Within the MCAO group, CXCL12–CXCR4 axis remains positively correlated with the pyroptosis composite score (r = 0.055, FDR = 7.69×10^{-5}) and the pyroptosis execution score (r = 0.039, FDR = 5.08×10^{-3}), whereas its association with the pyroptosis activation score is not significant (r = 0.028, FDR = 0.106). In the sham group, no correlation reaches significance. These results indicate that coupling between the CXCL12–CXCR4 axis and pyroptosis emerges after ischemia–reperfusion and aligns more closely with the composite and execution modules than with the activation module.

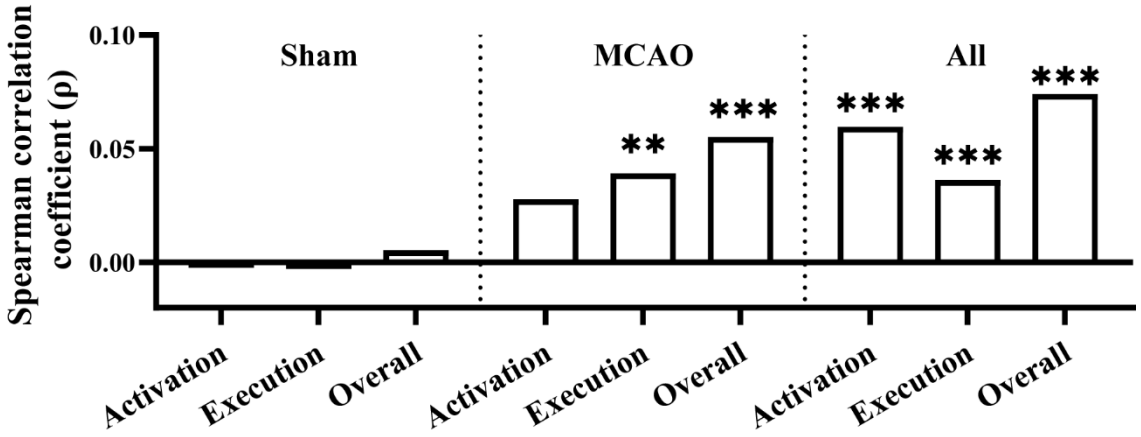

Figure 15. Correlations between the CXCL12–CXCR4 axis and pyroptosis in microglia.
Bars show the Spearman correlation coefficient (ρ) between the CXCL12–CXCR4 AxisScore and three pyroptosis readouts including the activation score, the execution score, and the composite score computed on batch-corrected microglia. Results are displayed separately for sham, MCAO, and all cells combined. Significance was assessed by two-sided Spearman tests with Benjamini–Hochberg correction; *** $p < 0.001$, ** $p < 0.01$, * $p < 0.05$. Correlations are negligible in sham, positive in MCAO for the composite and execution scores, and positive across all cells, with the largest coefficient for the composite score.

A network-based virtual knockout was applied with scTenifoldNet by constructing wild-type and CXCR4-silenced regulatory networks for each microglial cluster from the MCAO group and comparing them by manifold alignment and differential regulation; Stouffer Z scores were oriented by the CXCR4 effect so that negative values indicate attenuation under CXCR4 silence (Figure 16, A-C). At the overall pyroptosis level, cluster 7 shows the largest negative shift and approaches nominal significance, with additional negative trends in clusters 0 and

5, while clusters 1, 2, and 6 exhibit small positive counter-shifts (Figure 16C). In the execution component (Casp1, Casp11, Gsdmd, Gsdme, Ninj1, Panx1), negative shifts predominate in clusters 2, 3, 4, 5, and 7, whereas clusters 0, 1, and 6 show weak positive changes (Figure 16B). The activation component (including Nlrp3, Pycard, Irf1, Stat1, and Gbp family members) presents a mixed pattern with positive trends in clusters 1, 2, 3, 4, and 6 and negative trends in clusters 0, 5, and 7(Figure 16A). Effects remain modest overall and are generally not significant at the 0.05 level. Collectively, the most coherent attenuation concentrates in cluster 7, consistent with CXCL12–CXCR4 signaling sustaining pyroptosis tone in a specific microglial subpopulation, while other clusters display heterogeneous or compensatory responses.

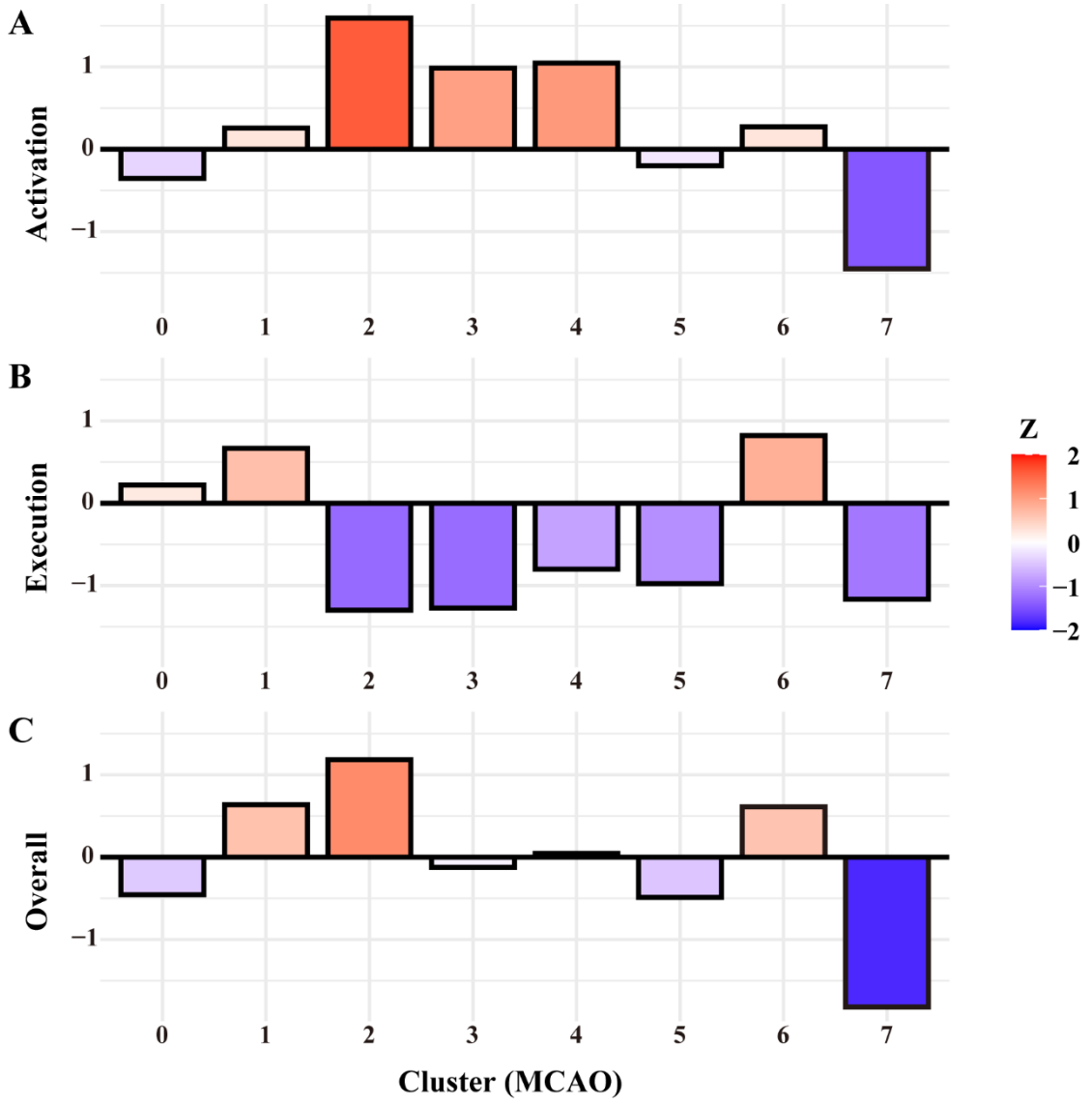

Figure 16. Effect of virtual CXCR4 knockout on pyroptosis in microglia.
Bars show oriented Stouffer Z scores per microglial cluster (0–7) derived from scTenifoldNet by comparing wild-type and CXCR4-silenced regulatory networks within the MCAO group. Panel A displays the activation module, including Nlrp3, Nlrp1a, Nlrc4, Aim2, Pycard, Nek7, Txnip, Irf1, Stat1, Gbp2, Gbp5, and Gbp7. Panel B displays the execution module, including Casp1, Casp11, Gsdmd, Gsdme, Ninj1, and Panx1. Panel C displays the overall module, the union of activation and execution with Il1b and Il18. Scores were oriented by the CXCR4 effect so that negative values indicate attenuation of the module under CXCR4 loss and positive values indicate enhancement. Bar color encodes Z and is clipped to the range −2 to 2. The strongest attenuation appears in cluster 7 for the overall module.

3.3 In vitro validation of CXCR4 in microglial pyroptosis after OGD/RO

3.3.1 Isolation, purification, and characterization of primary microglia

Primary microglial cultures were established from cerebral cortices of newborn wild type C57BL/6J mice at postnatal day 0 to day 4. Cortical tissue was dissected in ice cold buffer, carefully cleared of meninges, mechanically dissociated and seeded as mixed glial cultures in T-75 flasks. After astrocytes formed a confluent monolayer and loosely attached microglia progressively proliferated, microglia were harvested by gentle shaking, collected by centrifugation and resuspended in culture medium. The cells were then seeded at defined densities into 6 well or 24 well plates for subsequent experiments, resulting in a robust in vitro primary microglial culture model. The workflow was summarized in Figure 17.

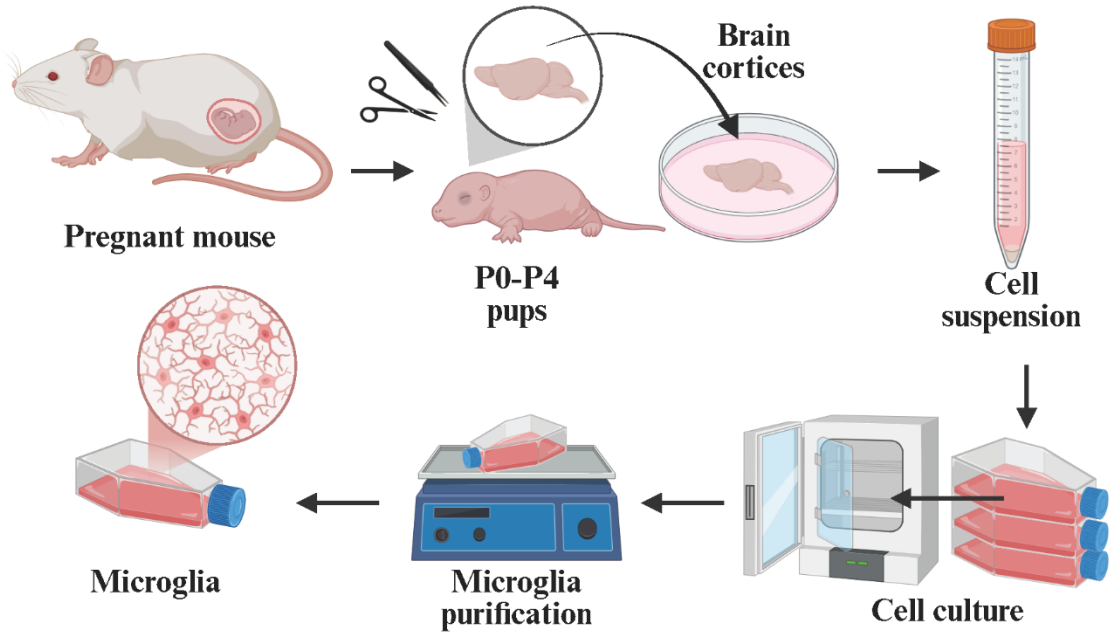

Figure 17. Establishment of the in vitro primary microglial culture model.
Brains were collected from P0 to P4 C57BL/6J pups obtained from pregnant mice, and cerebral cortices were dissected and transferred into ice cold buffer to generate a cell suspension. The resulting mixed glial cells were seeded into culture flasks and maintained in an incubator until astrocytes reached confluency. Loosely attached microglia were then purified by gentle shaking and reseeded to obtain primary microglial cultures for subsequent experiments. The schematic was created with BioRender.

Bright-field microscopy showed typical microglial morphology. Cells exhibited small oval or spindle-shaped somata with elongated bipolar or multipolar processes. Many cells appeared fusiform or rod-like with thin projections extending from both poles, whereas a minority were round with few or no processes. Immunofluorescence staining for the pan-microglial marker Iba-1 demonstrated robust cytoplasmic signal. Nuclear staining with DAPI indicated that nearly all nuclei corresponded to Iba-1 positive cells. The merged images confirmed that the culture was composed predominantly of microglia with consistent marker expression (Figure 18).

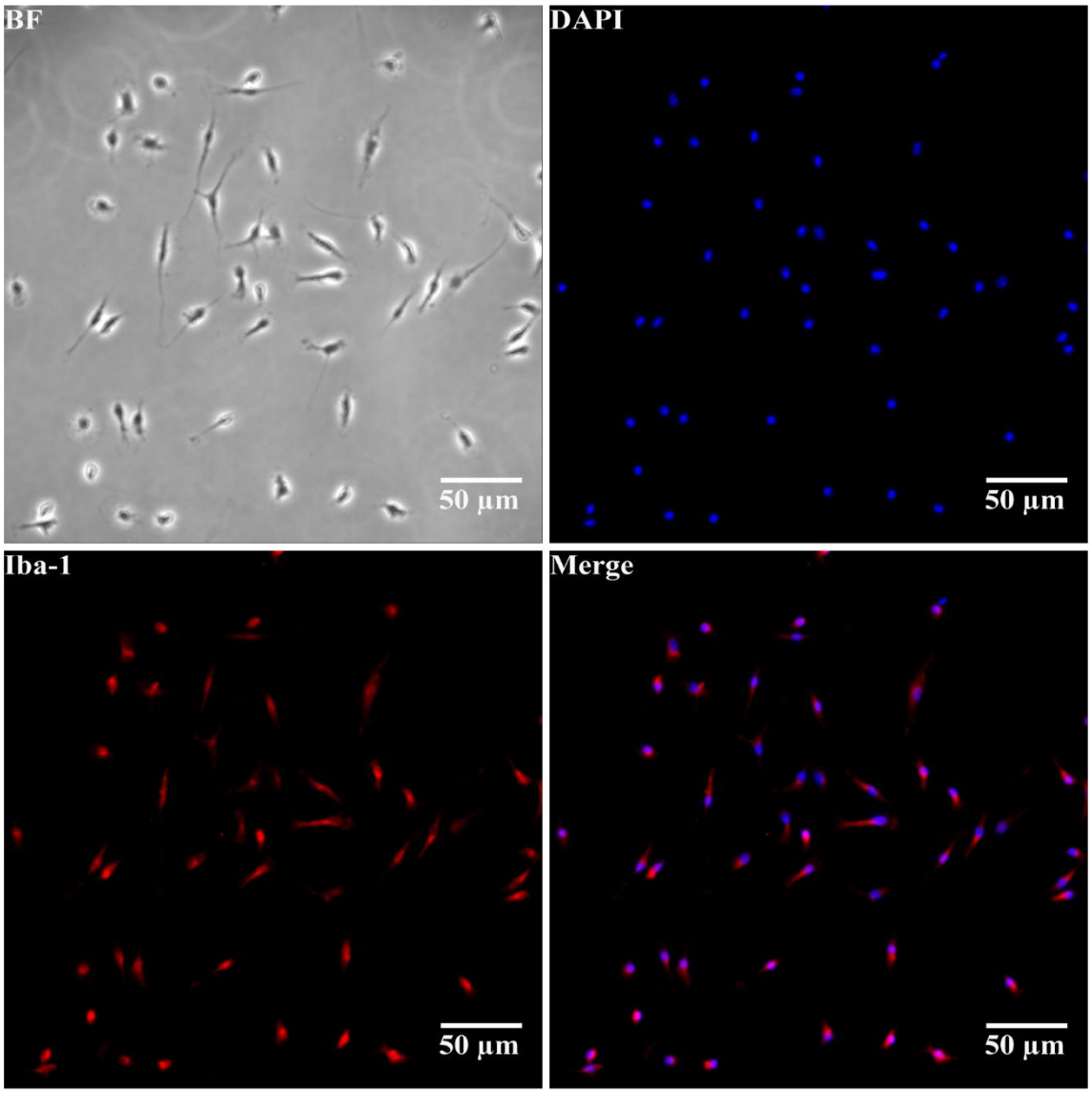

Figure 18. Morphology and identification of primary microglia.

Primary microglia were isolated from the cerebral cortices of neonatal wild-type C57BL/6J mice. Representative bright-field (BF) image shows characteristic somata and processes. Immunofluorescence images display Iba-1 immunoreactivity in the cytoplasm (red) and nuclei stained with DAPI (blue); the merged panel overlays both channels. Scale bar: 50 µm.

3.3.2 Impact of OGD/RO on primary microglial viability

Cell viability of primary microglia exposed to 2 h, 4 h, 6 h, or 8 h of oxygen-glucose deprivation (OGD) followed by 12 h of reoxygenation (RO) was assessed using the MTT assay. A normoxia group maintained under standard culture conditions without OGD served as the control. In total, five groups were analyzed. As shown in Figure 19, viability was significantly reduced in all OGD groups compared with normoxia ($p < 0.0001$). Exposure to 6 h of OGD followed by 12 h of reoxygenation resulted in approximately 50% viability, providing a moderate yet experimentally tractable level of injury. This condition was therefore selected for subsequent molecular analyses.

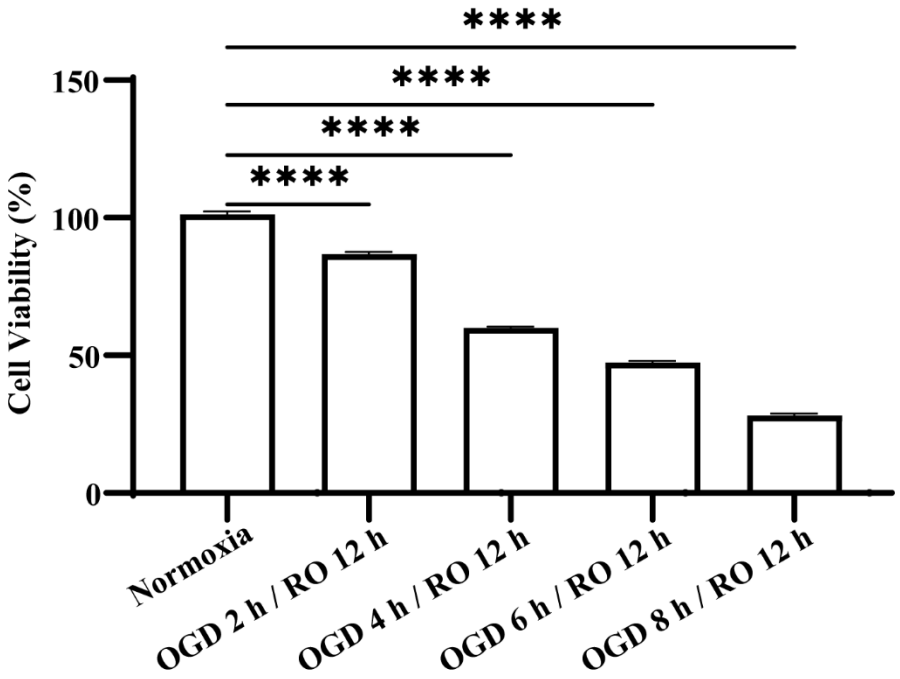

Figure 19. Primary microglial viability after OGD/RO.
Primary microglia underwent OGD for 0, 2, 4, 6, or 8 h, followed by 12 h reoxygenation (n =8). Mean ± SEM; **** $p < 0.0001$ vs normoxia; one-way ANOVA with multiple comparisons.

3.3.3 CXCR4 expression dynamics in primary microglia following OGD/RO

Western blot analysis revealed a transient, time-dependent increase in CXCR4 protein in primary microglia subjected to OGD followed by 12 h of reoxygenation (Figure 20, A–B). CXCR4 levels increased with OGD duration, peaked at 6 h OGD/12 h RO ($p < 0.05$), and declined at 8 h OGD/12 h RO. This pattern indicated a non-linear response to ischemic-like stress with maximal induction at an intermediate duration.

Immunofluorescence staining was performed to assess CXCR4 expression following OGD/RO (Figure 20, C–D). CXCR4 signals (green) were primarily cytoplasmic and were evaluated together with DAPI (blue) to identify nuclei. Quantification of mean CXCR4 fluorescence within DAPI-positive regions using ImageJ showed weak, diffuse cytoplasmic signal under normoxia, whereas the 6 h OGD/12 h RO group exhibited a marked increase ($p < 0.05$), consistent with the Western blot results. Considering both expression and the moderate level of cell viability at this time point, 6 h OGD followed by 12 h reoxygenation was selected as the representative exposure for subsequent experiments.

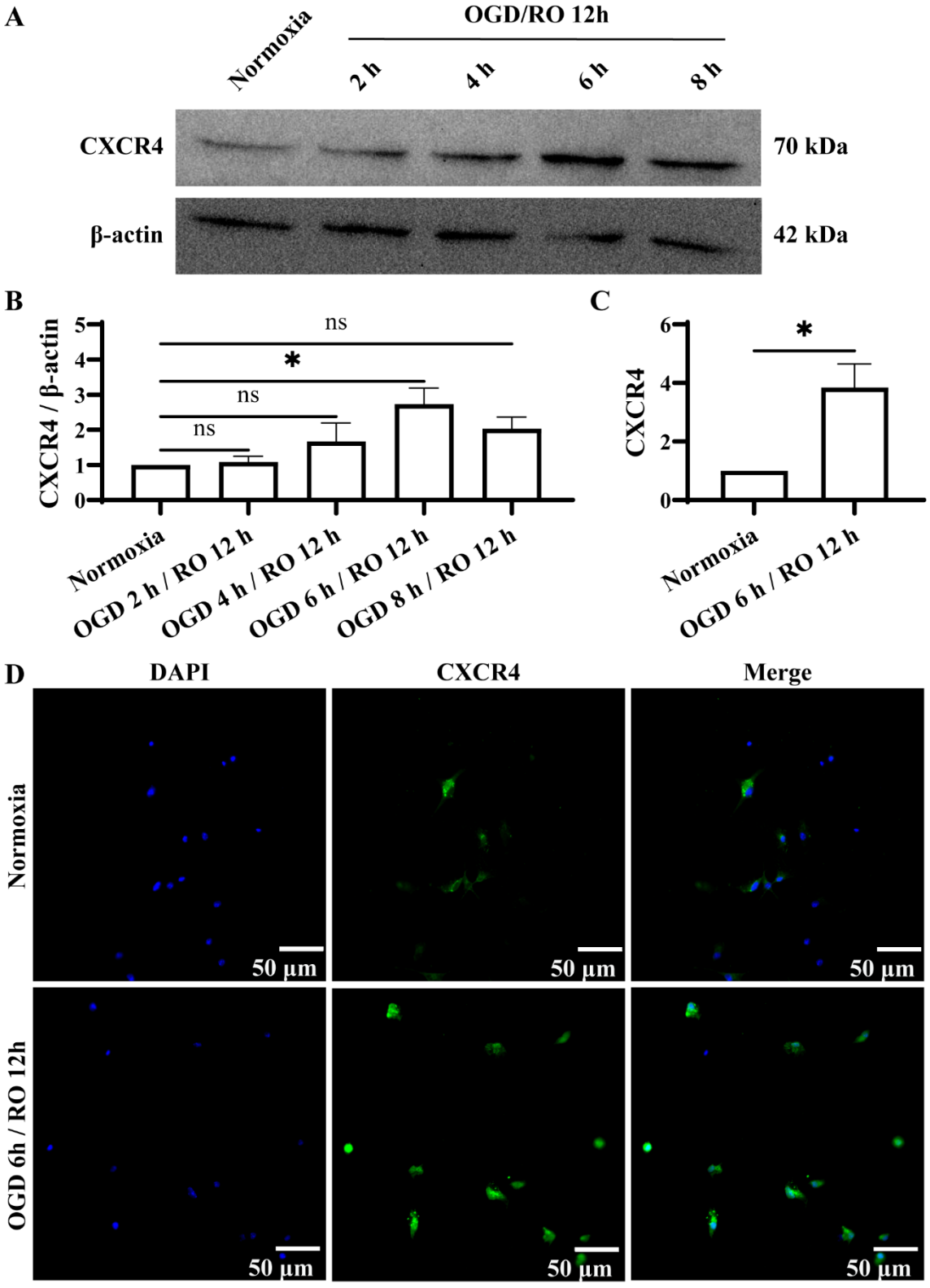

Figure 20. CXCR4 expression in primary microglia after OGD/RO.

A. Western blot of CXCR4 (~70 kDa) in primary microglia after OGD for 0, 2, 4, 6, or 8 h with 12 h reoxygenation; β-actin (42 kDa) as loading control. Densitometry was normalized to β-actin and expressed relative to normoxia; **B.** Relative CXCR4 expression in primary microglia subjected to oxygen glucose deprivation for 0, 2, 4, 6, or 8 h followed by 12 h reoxygenation. Data are presented as mean ± SEM, n = 3 independent experiments. *$p < 0.05$ versus normoxic control, one way analysis of variance with post hoc multiple comparison test; **C.** Quantification of CXCR4 immunofluorescence intensity in primary microglia under normoxia and after 6 h OGD followed by 12 h reoxygenation. Mean cellular CXCR4 intensity was measured within DAPI positive nuclear masks and normalized to normoxia. Data are presented as mean ± SEM; n = 3 independent experiments. *$p < 0.05$ vs normoxia; unpaired two tailed t test; **D.** Representative immunofluorescence images of primary microglia under normoxia and after 6 h OGD/12 h reoxygenation, showing CXCR4 (green) and nuclei stained with DAPI (blue). Scale bar: 50 μm.

3.3.4 Effect of CXCR4 antagonist on microglial viability after OGD/RO

AMD3100, also called plerixafor, is a selective small-molecule antagonist of CXCR4 that prevents CXCL12 binding and downstream G-protein signaling. Given the observed induction of CXCR4 and the enrichment of chemokine-guided motility, receptor trafficking, and inflammatory programs in microglia after MCAO, AMD3100 was used as a pharmacologic probe to test whether interrupting the CXCL12–CXCR4 axis modulates pyroptotic execution. Cell viability of primary microglia after OGD followed by 12 hours of reoxygenation was measured by the MTT assay across AMD3100 doses of 0, 1, 5, 10, and 20 Mm (Figure 21). AMD3100 was added immediately after OGD, before reoxygenation, and remained in the medium throughout the twelve-hour period. A normoxia group without OGD or AMD3100 served as the reference and was normalized to 100 percent; this group was not included in statistical testing. Viability in the 10 and 20 μM groups was significantly lower than in the OGD/RO control without AMD3100, $p < 0.05$. Balancing biological effect and practicality, 5 μM maintained an intermediate level of viability under hypoxic stress and was selected for subsequent cellular analyses; this dose is easier to handle and reduces pipetting error compared with 1 μM.

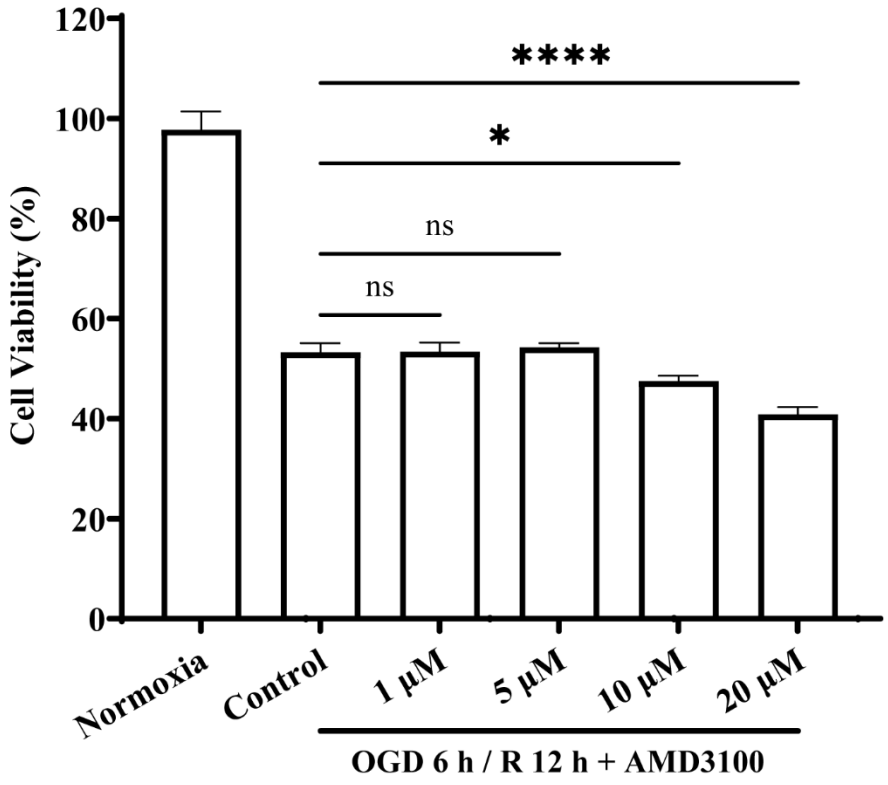

Figure 21. Primary microglial viability after OGD/RO+AMD3100.
Primary microglia underwent OGD/RO and were treated with AMD3100 at 0, 1, 5, 10, or 20 µM. Normoxia was displayed as a reference only. Mean ± SEM; n = 6. *p < 0.05 vs control (OGD/RO without AMD3100); **** p < 0.0001 vs control; one-way ANOVA with multiple comparisons.

3.3.5 AMD3100 attenuates GSDMD cleavage after OGD/RO in microglia

Based on the viability analysis, which showed approximately 50 percent survival at 6 h OGD followed by 12 h reoxygenation, and by the CXCR4 time course in Section 3.3.3, which showed maximal induction at the same time point, subsequent assays were performed under 6 h OGD and 12 h reoxygenation. The AMD3100 dose was set to 5 µM to balance CXCR4 blockade with acceptable survival and to ensure practical handling by reducing pipetting error relative to lower micromolar concentrations. AMD3100 was added immediately after OGD, before reoxygenation, and was maintained throughout the twelve-hour reoxygenation. Three groups were analyzed: normoxia, OGD/RO, and OGD/RO plus AMD3100. Western blotting detected full-length GSDMD at approximately 55 kDa and the cleaved N-terminal fragment at approximately 35 kDa in primary microglia, as shown in Figure 22, panels A to

C. Full-length GSDMD did not differ among the three groups. In contrast, the N-terminal fragment increased in the OGD followed by reoxygenation group relative to normoxia and decreased with AMD3100 compared with OGD followed by reoxygenation; both effects were significant at $p < 0.05$.

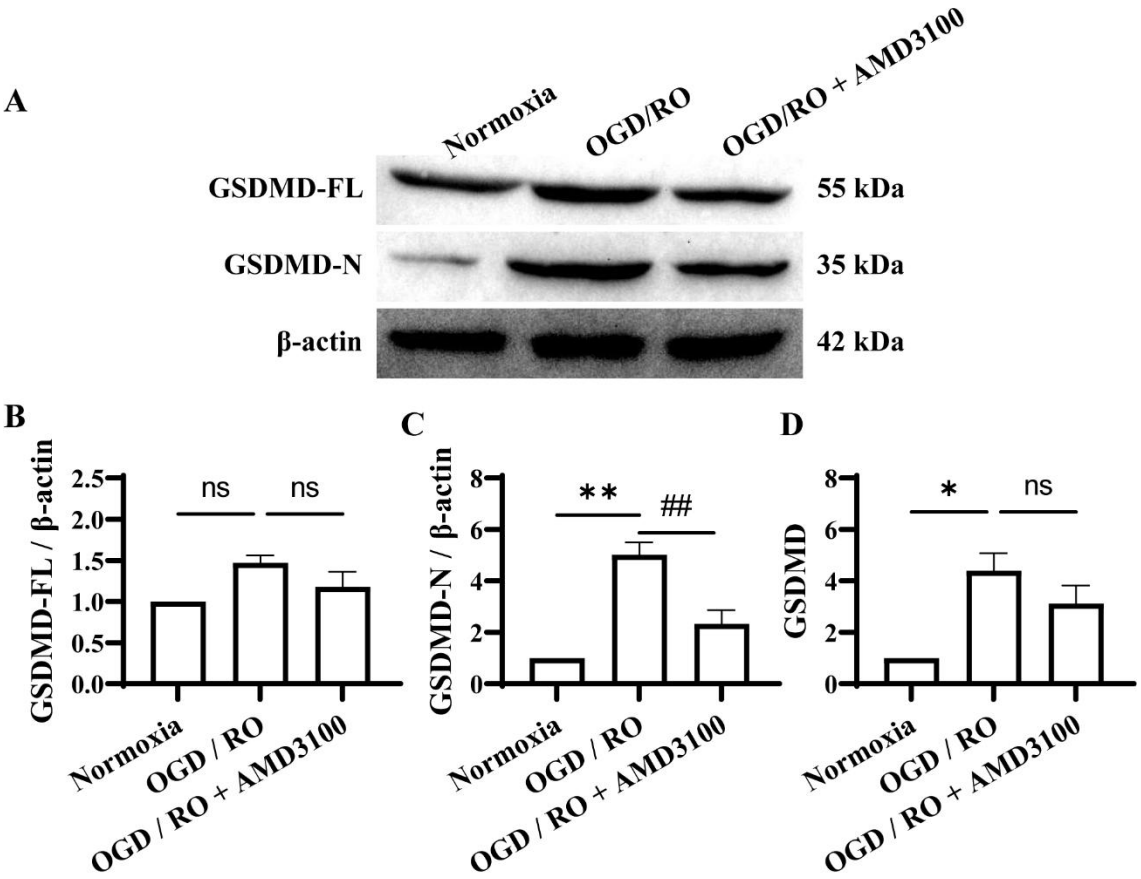

Figure 22. GSDMD expression and cleavage in microglia after OGD/RO+AMD3100.
A. Representative Western blot of full-length GSDMD and the cleaved N-terminal fragment in microglia under normoxia, OGD/RO, and OGD/RO + AMD3100. β-actin serves as the loading control; **B.** Densitometric quantification of GSDMD-FL normalized to β-actin and expressed relative to normoxia. Bars show mean ± SD; n = 3 independent experiments; **C.** Densitometric quantification of GSDMD-N normalized to β-actin and expressed relative to normoxia. Bars show mean ± SD; n = 3 independent experiments. ** $p < 0.01$ vs normoxia; ## $p < 0.01$ vs OGD/RO; one way ANOVA with multiple comparisons; **D.** GSDMD immunofluorescence intensity in primary microglia under three conditions. Bars show mean ± SEM; n = 3 independent experiments. One-way ANOVA with multiple comparisons was used for statistics; * $p < 0.05$ vs normoxia.

Immunofluorescence staining was performed to compare microglial morphology and the expression and subcellular localization of GSDMD across the three conditions (Figure 22D,

Figure 23). Under normoxia, cells displayed a ramified morphology with small somata and thin branching processes, and GSDMD signal was low and confined to perinuclear puncta without enrichment at the plasma membrane. After OGD followed by reoxygenation, microglia adopted a hypertrophic amoeboid appearance with retracted processes and condensed nuclei, while GSDMD redistributed from perinuclear puncta to a diffuse cytosolic pattern with clear enhancement along the nuclear envelope and cell perimeter, consistent with cleavage-driven translocation of the N-terminal fragment to membranes and early pore assembly during pyroptotic execution. Quantification of GSDMD immunofluorescence intensity showed a marked increase relative to normoxia, approximately 4.4-fold, and a reduction with AMD3100 to approximately 3.1-fold, although this decrease did not reach statistical significance, as shown in Figure 22D. With AMD3100 treatment, morphology partially normalized as soma size decreased and elongated processes reappeared, and GSDMD distribution shifted toward perinuclear puncta with minimal membrane-associated accumulation; a mixture of intermediate states indicated heterogeneous rescue (Figure 23). Together with immunoblot evidence for increased GSDMD-N after OGD followed by reoxygenation and its reduction by AMD3100, these imaging data support that CXCR4 blockade attenuated pyroptotic execution with slightly decreasing total GSDMD abundance.

Taken together, AMD3100 attenuated GSDMD cleavage without altering total GSDMD after OGD/RO, indicating an effect on the activation–execution axis of pyroptosis rather than on protein abundance. These data are consistent with a scenario in which CXCL12–CXCR4 signaling potentiates inflammasome–caspase-1 processing of GSDMD during is-chemia–reoxygenation stress, while pharmacological blockade tempers this processing and may limit pore formation and lytic cell death.

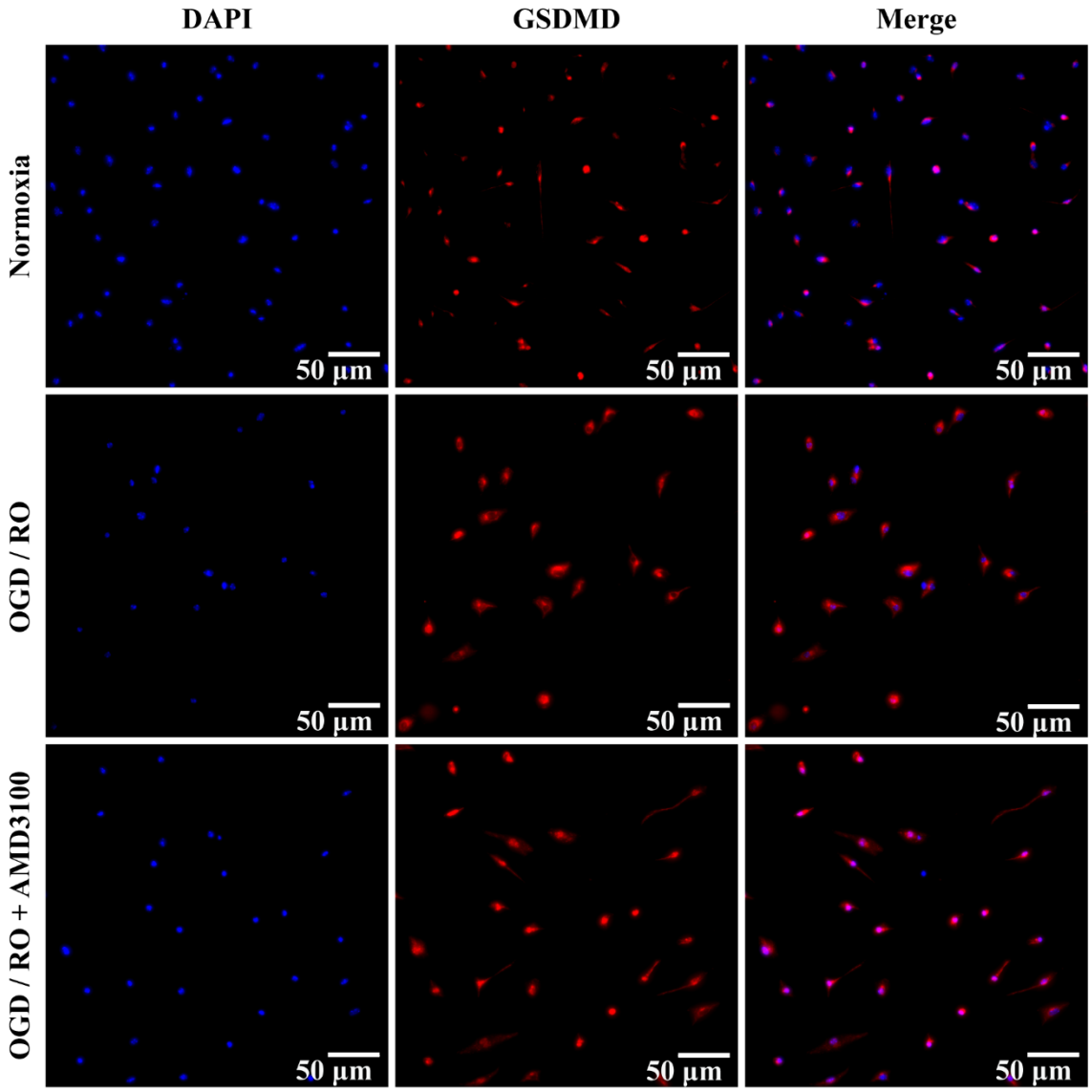

Figure 23. Immunofluorescence staining of microglia after OGD/RO+AMD3100.
Nuclei stained with DAPI, blue; total GSDMD, red. Normoxia shows ramified cells with small somata and perinuclear puncta of GSDMD. OGD/RO produces hypertrophic amoeboid cells with retracted processes and diffuse cytosolic GSDMD with membrane enrichment. AMD3100 reduces membrane-associated GSDMD and partially restores a ramified morphology with perinuclear puncta. Scale bar: 50 µm.

4 DISCUSSION

4.1 Microglial reactions in ischemia–reperfusion

Microglia are tissue-resident macrophages of the central nervous system and display high plasticity. After acute brain injury, including traumatic brain injury, ischemic stroke, and intracerebral hemorrhage, microglia are among the earliest non-neuronal cells to become activated, rapidly migrating toward the lesion and undergoing marked morphological and functional changes. In ischemia reperfusion injury, microglia play a dual and central role (Zhao et al., 2024). They can drive neuroinflammation and aggravate damage, but they can also support debris clearance and tissue repair (Song et al., 2019). These effects depend on activation states and downstream signaling pathways. For a long time, studies consistently observed rapid microglial activation after ischemia reperfusion and microglia were broadly described as proinflammatory and anti-inflammatory phenotypes by analogy to macrophage polarization (Song et al., 2019). The proinflammatory M1 phenotype released mediators including TNF-α, IL-1β, IL-6, and reactive oxygen species, which amplified neuronal injury (Song et al., 2019; Tian et al., 2024). The anti-inflammatory M2 phenotype secreted factors including IL-10 and TGF-β, thereby promoting repair and neuroprotection (Song et al., 2019; Tian et al., 2024). The dynamic balance between these phenotypes was considered crucial for determining injury severity and recovery. Although this binary model had clear limitations, it provided a useful conceptual framework for morphological and functional interpretation of microglia after ischemia-reperfusion injury. More recently, single-cell RNA sequencing and spatial transcriptomics have revealed that microglia adopt multiple transcriptionally and functionally distinct subpopulations across time and brain regions (H. Li et al., 2023). After ischemia-reperfusion, microglial states extend far beyond the simple M1/M2 framework and exhibit pronounced clustering and functional heterogeneity.

4.1.1 Functional diversification of microglia after ischemia–reperfusion

In the present study, single-cell analysis of ipsilateral brain tissue from mice subjected to 1 h MCAO followed by 24 h reperfusion was used to classify microglia by unsupervised clustering based on top marker genes, and the functional characteristics of the resulting clusters were annotated after clustering without imposing predefined categories, thereby minimizing bias from prior assumptions regarding microglial polarization. After integration and subsetting, sham microglia largely occupied a compact basin in UMAP space, consistent with a relatively uniform homeostatic phenotype in the uninjured brain, in agreement with previous reports from other groups using a similar model (H. Li et al., 2023). In contrast, MCAO microglia redistributed into several discrete territories with limited overlap with sham cells, and unsupervised clustering resolved eight transcriptional states. This diversification is in line with accumulating single-cell evidence that microglia after ischemic stroke occupy multiple activation and repair states rather than a simple binary M1/M2 continuum (H. Li et al., 2023). The P2ry12- and Tmem119-enriched cluster 0 represented homeostatic surveillant microglia and anchored the trajectory. In contrast, cluster 1 expressed chemokines and inflammatory mediators including Ccl2, Ccl4, and Tnf together with negative feedback regulators such as Socs3 and Gpr84, consistent with a chemokine-rich inflammatory state that can attract leukocytes and adjust microglial sensitivity to danger signals. Cluster 2 expressed Spp1, Lgals3, Lpl, Cd14, and Plin2, indicating a phagocytic lipid-handling phenotype with enhanced debris recognition, lysosomal activity, and lipid clearance reminiscent of disease-associated microglia described in other CNS pathologies. Cluster 3 combined genes linked to cytoskeletal remodeling and chemotaxis, including Lgals1, Capg, Ccl5, and Ccl9, suggesting a stress-responsive migratory phenotype that may support directed movement toward injured or necrotic regions. Other clusters pointed to additional functional axes. Cluster 4 expressed Il1r2, Ms4a family members, and immediate-early and cell-cycle checkpoint genes including Ier3 and Cdkn1a, suggesting a state that modulates interleukin-1 signaling and adapts to stress while maintaining controlled responsiveness. This configuration is compatible with an early regulatory node that limits excessive IL-1 signaling and may transiently restrain the transition to a fully pro-inflammatory phenotype. Cluster 5 was dominated by cell-cycle and replication genes such as Stmn1 and Mcm5, reflecting microglial proliferation,

which has been recognized as a key component of microglial repopulation and lesion containment after ischemic injury. Cluster 6 expressed Cldn5, Flt1, Slc2a1, and Ly6a, a vascular-associated signature that is compatible with perivascular microglia closely interacting with endothelial cells, although a contribution of rare endothelial doublets cannot be fully excluded. Finally, cluster 7 expressed a type I interferon–responsive program, including Cxcl10, Ifit1, Ifit2, Rsad2, and Isg15, representing an interferon-stimulated state that may mediate antiviral defense, debris sensing, and crosstalk with infiltrating lymphocytes. Together, these states mapped a spectrum from homeostatic surveillance toward inflammatory, chemotactic, proliferative, phagocytic lipid-handling, interferon-responsive, and vascular-associated phenotypes after ischemia–reperfusion, consistent with the view that microglial activation encompasses multiple partially overlapping programs rather than a strict M1/M2 dichotomy.

4.1.2 Microglial state transitions after ischemia–reperfusion

Pseudotime analysis organized the clustered states into a plausible progression after ischemia–reperfusion. With the homeostatic cluster 0 fixed as the root, microglia in the MCAO group followed a monotonic ordering from cluster 0 through cluster 4, then through an intermediate segment involving clusters 6 and 1, followed by cluster 5, then cluster 3, and finally clusters 2 and 7. Early in the inferred trajectory, cells in cluster 0 retained homeostatic surveillance features, and the transition to cluster 4 suggested that microglia first engaged stress-adaptation and interleukin-1 modulatory programs. This stepwise transition fits with the concept that microglial activation initially involves controlled sensing and gating of inflammatory signals before full effector deployment. The mid-trajectory segment had two components. The chemokine-rich cluster 1 indicated a state in which microglia became competent to orchestrate leukocyte recruitment and paracrine signaling, while cluster 6 suggested that a subset of cells engaged in perivascular or blood–brain barrier–related interactions. The emergence of a proliferative cluster 5 later along the trajectory is consistent with clonal expansion of reactive microglia, a process that has been observed in vivo and may serve to amplify specific effector states within the lesion. In the late pseudotime stages, cluster 3 represented a stress-responsive migratory phenotype, and clusters 2 and 7 represented Spp1-positive phagocytic lipid-handling and type I interferon (type I IFN)–responsive states respectively. The positioning of these clusters at the distal end of the trajectory suggests that after initial

sensing, signaling, and expansion, microglia progressed toward effector functions centered on migration into damaged tissue, phagocytic clearance of myelin and cellular debris, and interferon signaling. This framework is compatible with previous reports that post-ischemic microglia sequentially transition from early surveillance and anti-inflammatory states to proliferative, inflammatory, and then debris-clearing phenotypes over days after reperfusion. At the same time, the presence of both phagocytic and interferon-responsive states at late pseudotime indicates that microglia do not converge on a single terminal phenotype but instead branch into parallel effector arms that may differentially influence neuronal survival, synaptic remodeling, and long-term outcomes. An important observation was that cluster 0 contained cells at both the earliest and the latest pseudotime positions, even though its overall abundance decreased after MCAO. This pattern suggests that a subset of microglia may have reverted toward a homeostatic-like transcriptional profile after traversing inflammatory, proliferative, migratory, and phagocytic–interferon states. Such apparent "re-homeostatic" microglia have been reported in other injury models and may reflect successful resolution of inflammation in parts of the tissue. However, the transcriptional resemblance to baseline surveillance does not guarantee full functional normalization, and subtle epigenetic or metabolic imprints may persist. In the context of ischemia–reperfusion, this potential return toward homeostasis supports the concept that microglial activation is dynamically reversible and that timely resolution of inflammatory and phagocytic programs may be critical for limiting chronic neuroinflammation and secondary neurodegeneration. Taken together, these data support a model in which ischemia–reperfusion first induces broad remodeling of vascular and glial compartments, then drives microglia from a relatively uniform homeostatic population into multiple activated states that are ordered along a trajectory from stress adaptation and cytokine modulation toward chemokine production, perivascular interaction, proliferation, migration, phagocytic lipid handling, and interferon responsiveness, with partial re-entry into a homeostatic-like state.

4.1.3 Type I IFN–responsive microglia as the main pyroptotic state

Pyroptosis module scoring indicated that microglial pyroptosis programs after ischemia–reperfusion were not uniformly upregulated across all states but instead concentrated in an interferon-responsive microglial subset (cluster 7), whose top marker genes were dominated

by canonical interferon-stimulated genes such as Cxcl10, Ifit1, Ifit2, Rsad2, and Isg15, consistent with a type I interferon–driven transcriptional program. Although eight transcriptional states emerged after MCAO, most MCAO clusters (1–6) showed reduced activation and overall pyroptosis scores compared with sham cluster 0 at both the single-cell and sample levels, with the largest decreases in chemokine-rich inflammatory, Spp1^{+} phagocytic, proliferative, and vascular-associated states. In contrast, the type I IFN–responsive cluster 7 consistently displayed higher activation and higher overall pyroptosis scores than the sham reference, whereas execution scores did not change significantly. This pattern suggests that cluster 7 represents the principal post-ischemic pyroptotic microglial population in which inflammasome-related transcriptional programs are selectively enhanced rather than globally suppressed. Integration of pseudotime and state identity further supported this interpretation, as cluster 7 occupied a distal position along the inferred trajectory, downstream of stress-adaptation, inflammatory, proliferative, migratory, and Spp1^{+} phagocytic states, indicating that amplification of pyroptosis-related modules occurred during late stages rather than during early sensing or expansion phases. These observations are consistent with accumulating evidence that type I interferons are not only central mediators of antiviral and antibacterial immunity but also direct regulators of pyroptosis and other forms of programmed cell death. IFN-I can induce a TRIF-dependent transcriptional program that upregulates Zbp1, Mlkl, caspase-11, and Gsdmd, thereby facilitating NLRP3 inflammasome activation and GSDMD-dependent pore formation (Y. Li et al., 2018). During infections including influenza, IFN-I signaling through the JAK–STAT pathway shifts the mode of cell death from apoptosis toward pyroptosis and augments inflammatory output (Lee et al., 2018). IFN-β has been reported to increase the susceptibility of mesenchymal stem cells to pyroptosis, which further supports a pro-pyroptotic role of IFN-I in selected cellular contexts (Zhang et al., 2020). At the same time, IFN-I and pyroptosis participate in feedback circuits that restrain excessive inflammation. GSDMD-dependent pore formation and the associated ion fluxes can attenuate cGAS-driven IFN-I production, providing a negative feedback loop that limits sustained interferon signaling and tissue damage (Banerjee et al., 2018). IFN-I–induced guanylate-binding proteins such as GBP1 promote pyroptosis in macrophages to improve control of intracellular pathogens (L. Li et al., 2023). Together, these data indicate that IFN-I does not

simply act upstream of inflammasome activation but dynamically shapes the onset, magnitude, and resolution of pyroptosis, providing a mechanistic framework for the selective enrichment of pyroptosis-related transcriptional modules in type I IFN–responsive microglia after ischemia–reperfusion in the present study.

4.2 The role of CXCR4 in microglia after ischemia–reperfusion

CXCR4 is a chemokine receptor exerting complex and context-dependent effects in brain ischemia by modulating inflammation, cell migration, neuroprotection, and tissue repair. Its activity is mediated primarily through the CXCL12 (SDF-1)/CXCR4 signaling axis, which is dynamically regulated after ischemic injury (Xutong Li et al., 2020). CXCR4 is upregulated after cerebral ischemia and facilitates the recruitment of leukocytes and other inflammatory cells, thereby aggravating tissue damage and blood–brain barrier disruption. Pharmacological inhibition of CXCR4 with antagonists including AMD3100 reduces inflammatory cell infiltration, suppresses proinflammatory cytokine production, and preserves blood–brain barrier integrity, leading to improved neurological outcomes in animal models (Jun Huang et al., 2013; Chengli Liu et al., 2023; Werner et al., 2020). However, the contribution of CXCR4 to microglial pyroptosis after ischemia–reperfusion had not been clarified previously and the present work provides the first focused analysis of this relationship.

4.2.1 CXCR4 modulates microglia morphological remodeling after OGD/RO

Ischemia-reperfusion triggered distinct morphological responses of microglia. After ischemic stroke and during reperfusion, microglial morphology showed a spatiotemporal relationship with the progression of brain injury (Morrison & Filosa, 2013). In the healthy brain under homeostatic conditions, microglia displayed a highly ramified dendritic shape and served a surveillance role (Nimmerjahn et al., 2005). The soma was small, whereas numerous dynamic processes extended broadly to continuously monitor the surrounding microenvironment and support tissue homeostasis (Nimmerjahn et al., 2005). After ischemia reperfusion, microglia in the injured regions shifted from a highly ramified dendritic morphology to a less ramified, process retracted, or amoeboid shape (Yuan et al., 2025). Quantitative analyses showed significant reductions in total process length and in the number of endpoints per cell, with the most pronounced decline within 24 hours after reperfusion (Morrison & Filosa,

2013). These changes were strongest near the necrotic core, where dendritic arbors collapsed and process dynamics weakened, consistent with robust activation. In the present research, immunofluorescence imaging revealed a clear morphology shift across conditions. Under normoxia, microglia preserved a homeostatic surveillance profile, characterized by small somata and thin, highly branched processes. This ramified architecture is typical of resting microglia and supports continuous environmental scanning through dynamic process extension and retraction, consistent with a low stress state. After OGD followed by reoxygenation, microglia underwent pronounced structural remodeling toward a hypertrophic amoeboid appearance. Soma enlargement, process retraction, and nuclear condensation indicated a transition from surveillance to an activated effector state. De-ramification and amoeboid shaping generally accompany increased motility, phagocytic engagement, and pro injury signal integration in ischemic contexts. The combination of enlarged cell bodies and condensed nuclei also aligns with disruption of ionic and osmotic homeostasis during severe inflammatory execution, suggesting that morphology changes paralleled the onset of pyroptosis related cellular stress. AMD3100 treatment partially reversed these structural alterations. Reduced soma size and re-emergence of elongated processes indicated attenuation of the OGD reoxygenation driven hyperactivation and a shift back toward a surveillance like morphology. This morphological normalization supported a role for CXCR4 signaling in shaping early microglial activation dynamics after ischemic stress. The persistence of intermediate morphologies suggested heterogeneous rescue. Some cells likely progressed beyond a reversible activation phase, whereas others remained responsive to CXCR4 blockade. Overall, morphology-based evidence indicated that CXCR4 inhibition moderated early microglial overactivation and may limit the downstream injury cascade initiated during reperfusion.

4.2.2 Ischemia-reperfusion-induced CXCR4 drives multiple microglial responses

The re-analysis of public RNA-seq data from microglia isolated three days after 60-min MCAO indicates that ischemia–reperfusion induces a broad transcriptional reprogramming dominated by up-regulated genes, and positions CXCR4 among the more strongly induced transcripts. The enriched terms linked to ameboid cell migration, chemotaxis, regulation of angiogenesis and vasculature development, and gliogenesis converge on a picture in which microglia are not only activated but are also poised to migrate, remodel their interactions

with the vasculature, and participate in glial reorganization in peri-infarct regions. This pattern fits well with the concept that after ischemia–reperfusion, microglia leave a relatively stationary surveillance mode and enter a motile, guidance-cue–responsive state that supports directed movement toward injured tissue and evolving vascular niches. Cellular component and molecular function terms add mechanistic depth to this interpretation. Enrichment at the leading edge, growth cone, distal axon, and early endosome points to coordinated actin remodeling and dynamic receptor trafficking. These changes are compatible with ligand-dependent CXCR4 internalization, recycling, and polarized membrane distribution, which are known to sustain chemokine gradient sensing and directional motility (Cambier et al., 2023; Heuninck et al., 2019; Tarasova et al., 1998). In parallel, over-representation of actin binding, cytokine and chemokine binding, and cytokine receptor activity suggests that microglia increase their capacity to integrate adhesive, chemotactic, and inflammatory cues. Together, these findings support a model in which ischemia–reperfusion–induced CXCR4 does not act in isolation but participates in a broader motility and signaling module that enables microglia to reposition within the injured brain and dynamically tune their responsiveness to extracellular signals.

The co-occurrence analysis of CXCR4 with other differentially expressed genes across enriched terms further refines this functional neighborhood. The presence of Cxcl12 among the top partners is consistent with reinforcement of the canonical ligand–receptor pair, while the inclusion of Vegfa, Edn1, and Ednra points to tight coupling between CXCR4 signaling and vascular or endothelial regulatory circuits. Morphogen and trophic factors such as Bmp4, Wnt5a, Igf1, and Nrg1, together with the cytoskeleton-associated kinase Abl1, suggest that CXCR4-positive microglia operate at the intersection of developmental patterning cues, survival and growth signals, and cytoskeletal control. In this context, the frequent co-mention of Il1b with CXCR4 indicates that chemokine-responsive microglia also reside in a cytokine-enriched environment where inflammasome-related signaling, receptor trafficking, and motility are closely intertwined. Such a setting is compatible with microglia that both sense and amplify inflammatory signals while simultaneously adapting their positioning relative to vessels, neurons, and infiltrating leukocytes.

These analyses support that CXCR4 upregulation after ischemia–reperfusion contributes to a multifaceted microglial program encompassing chemokine responsiveness, migration, vascular interaction, and cytokine signaling rather than a single linear “pro-inflammatory” state. At the same time, several limitations should be acknowledged. The bulk RNA-seq dataset captures $CD11b^{+}/CD45^{int}$ microglia at a single time point three days after reperfusion and cannot resolve cell-to-cell heterogeneity or earlier transient states. Transcriptional changes do not necessarily translate into proportional alterations at the protein or functional level, and enrichment and co-occurrence analyses infer pathway activity from gene lists without proving direct regulatory relationships.

4.2.3 CXCR4 as a modulator of microglial pyroptosis after ischemia–reperfusion

The present study combined single-cell transcriptomic analysis, network-based virtual knockout, and in vitro pharmacologic blockade to examine the relationship between CXCR4 signaling and microglial pyroptosis after ischemia–reperfusion. At the transcriptomic level, the CXCL12–CXCR4 axis score showed weak but statistically robust positive correlations with pyroptosis modules at the single-cell scale. Across all microglia (MCAO plus sham), the axis score correlated most strongly with the composite pyroptosis score and, to a lesser extent, with the execution module, whereas the association with the activation module was smaller. Importantly, these correlations were essentially absent in sham microglia, indicating that coupling between CXCR4 activity and pyroptosis emerged in the post-ischemic context rather than representing a fixed homeostatic property of microglia. The small effect sizes (Spearman r in the range of 0.03–0.07) are compatible with at least two, not mutually exclusive, scenarios. First, CXCR4 signaling may tune pyroptotic tone in concert with many other pathways rather than functioning as a dominant on–off switch. Second, pyroptosis may involve only a vulnerable, CXCR4-sensitive subset of microglia after ischemia–reperfusion, rather than the entire microglial population. This interpretation is consistent with reports that CXCL12/CXCR4 is upregulated after brain injury and can modulate inflammasome-related cytokines and GSDMD-dependent pathways in other settings (Cheng et al., 2021; Gu et al., 2021; C. Liu et al., 2023).

The network-based virtual CXCR4 knockout further supported a contributory role of this axis in sustaining pyroptosis-related regulatory programs, although the magnitude of the effect remained modest. When CXCR4 was virtually silenced with scTenifoldNet, oriented Stouffer Z scores for pyroptosis modules showed heterogeneous patterns across microglial clusters. The most coherent attenuation at the composite level occurred in the type I interferon responsive microglial cluster, which, as noted above, also represented the main pyroptosis-enriched cluster in our dataset. After virtual knockout, scores for the activation module increased in several clusters, yet many of these same clusters showed decreases in the execution module. Together, these findings suggest that CXCR4 signaling is more important for maintaining the transcriptional architecture of the execution arm of pyroptosis, particularly in the type I interferon responsive microglial subset, whereas upstream inflammasome activation modules remain under broader and partly CXCR4-independent control. This view aligns with previous work in experimental subarachnoid hemorrhage and other central nervous system injury models, where CXCR4-related pathways have been linked to neuroinflammation and pyroptotic injury, but also with reports that CXCL12 can dampen inflammasome activation in some microglial contexts, indicating that the direction of effect is context dependent and shaped by the surrounding cytokine milieu (C. Liu et al., 2023; Roosen et al., 2021).

The in vitro OGD/RO experiments provided mechanistic support for a functional contribution of CXCR4 signaling to microglial pyroptotic execution. Primary microglia exposed to increasing durations of OGD followed by reoxygenation showed a non linear induction of CXCR4 protein. This nonlinear pattern may have reflected reduced cell viability and a lower number of surviving cells at the longest OGD duration, because within the 2 h, 4 h, and 6 h OGD range CXCR4 protein levels increased approximately linearly with OGD duration, with a peak at 6 h OGD and 12 h reoxygenation that coincided with about 50 percent cell viability. Under this intermediate injury condition, pharmacologic blockade of CXCR4 with AMD3100 did not alter total GSDMD abundance but selectively reduced the cleaved N terminal GSDMD fragment and decreased membrane associated GSDMD signal in immunofluorescence, while partially normalizing microglial morphology. These findings were consistent with a specific effect on the activation–execution axis of pyroptosis, in which inflammasome and caspase 1 dependent processing of GSDMD was tempered, thereby limiting pore formation and lytic cell death rather than producing a general suppression of GSDMD

expression. They also converged with in vivo and ex vivo studies in experimental stroke and other central nervous system injuries in which AMD3100 attenuated microglial activation, reduced inflammatory mediator production, and improved functional outcome, implicating CXCL12–CXCR4 signaling as a modifiable amplifier of neuroinflammation (J. Huang et al., 2013; Michalettos et al., 2021; Walter et al., 2015).

Taken together, these three lines of evidence support a model in which CXCR4 signaling contributes to microglial pyroptosis after ischemia–reperfusion but does so in a graded and state-dependent manner. The single-cell correlations indicate that cells with higher CXCL12–CXCR4 axis activity tend to show stronger engagement of pyroptosis modules, particularly the execution component, once ischemic injury has occurred. The virtual knock-out analysis indicates that removal of CXCR4 weakens the inferred regulatory support for pyroptosis genes, most consistently in an interferon-responsive microglial subpopulation, which may represent a subset especially prone to CXCR4-dependent coupling between chemokine signaling and pyroptotic machinery. The OGD/RO and AMD3100 experiments then provide causal evidence that CXCR4 activity is required for full GSDMD cleavage under ischemia-like stress in primary microglia, with blockade attenuating morphological and molecular hallmarks of pyroptotic execution.

At the same time, several aspects of the data argue against a simple linear pathway in which CXCR4 alone determines microglial pyroptosis. The correlations between axis and pyroptosis scores, while statistically robust, are small, and the network-based perturbations yield modest Z shifts that rarely reach conventional significance. The activation module shows divergent responses across clusters, suggesting that inflammasome priming and activation are shaped by a broader network of signals that include, but are not limited to, CXCR4. The AMD3100 experiments were performed in vitro and focused on GSDMD cleavage, without direct measurement of IL-1β or IL-18 release or distinction from other forms of cell death. In addition, CXCL12–CXCR4 signaling can exert neuroprotective or anti-inflammatory effects in other models, including suppression of inflammasome activation in LPS-challenged microglia, which suggests that cell type, timing, and injury context strongly influence how this axis intersects with pyroptosis pathways (Brint et al., 2024; Gu et al., 2021; Roosen et al., 2021).

Within these limitations, the current findings support the view that CXCR4 acts as a context-dependent modulator of microglial pyroptosis after ischemia–reperfusion. The data point to a preferential influence on the execution arm of pyroptosis, particularly on GSDMD processing in a subset of activated microglia, rather than a uniform effect on inflammasome activation across all microglial states. This has potential therapeutic implications. Partial inhibition of CXCR4 signaling, for example through optimized dosing or timing of AMD3100 or related agents, may be sufficient to dampen excessive pyroptotic execution and associated secondary injury while preserving beneficial aspects of microglial chemotaxis, phagocytic clearance, and tissue remodeling. Future work combining conditional CXCR4 deletion in microglia with in vivo readouts of inflammasome activation, IL-1 family cytokine release, and long-term functional outcome will be important to delineate more precisely how CXCR4 integrates into the broader network of pathways that govern microglial pyroptosis and post-ischemic repair.

4.2.4 Therapeutic prospects and of CXCR4 inhibition in ischemia–reperfusion

Findings from the present study, together with accumulating evidence from experimental stroke models, indicate that CXCR4 signaling amplifies microglial pyroptotic execution in the acute phase of ischemia–reperfusion (J. Huang et al., 2013; Walter et al., 2015). In this framework, transient inhibition of the CXCL12–CXCR4 axis may attenuate lytic cell death and secondary neuroinflammation while leaving basal GSDMD expression largely preserved, consistent with reports that AMD3100 reduces inflammatory cytokine production, protects blood–brain barrier integrity, dampens microglial activation, and improves neurological outcome (Wang et al., 2014).

Preclinical work has mainly used systemic AMD3100 dosing to target CXCR4. In rodent focal ischemia models, once-daily intraperitoneal injections at 0.5 or 1 mg/kg for several days initiated shortly after MCAO reduced blood–brain barrier leakage, myeloperoxidase-positive cell infiltration, and pro-inflammatory cytokines such as IL-6, TNF-α, and IFN-γ, with associated improvements in infarct volume and neurological scores (J. Huang et al., 2013; D. Li et al., 2018). In a photothrombotic stroke model, twice-daily AMD3100 at 0.5 mg/kg from day 2 to day 6 after stroke decreased microglial activation and enhanced recovery of lost neurological function (Walter et al., 2015). These regimens broadly support systemic

administration during the early inflammatory window and indicate that short courses over several days are sufficient to exert biological effects. In the present study, OGD/RO experiments in primary microglia further inform dose and timing considerations. CXCR4 protein was induced in a time-dependent manner and peaked at 6 h OGD plus 12 h reoxygenation, which coincided with roughly 50% cell viability. Under this intermediate injury condition, a moderate concentration of AMD3100 (5 μM) preserved a workable level of survival but significantly attenuated GSDMD cleavage, whereas higher doses reduced viability. These observations argue for a therapeutic window in which CXCR4 inhibition is introduced after ischemia–reperfusion has occurred, at a stage when pyroptotic signaling is engaged but a substantial fraction of microglia remains viable, and at doses that limit execution without imposing excessive toxicity. At the same time, systemic CXCR4 inhibition carries important limitations. AMD3100 (plerixafor) is clinically approved as a hematopoietic stem cell mobilizing agent and induces rapid mobilization of $CD34^+$ cells and leukocytes into the peripheral blood (Devine et al., 2004; Emir et al., 2014). Although generally well tolerated, treatment can cause leukocytosis, gastrointestinal symptoms, and injection-site reactions and is contraindicated in patients with acute or chronic leukemia because of the risk of mobilizing malignant cells (Liu et al., 2015; Slater, 2012).

In the context of ischemic stroke, peripheral immune cell recruitment is a double-edged sword: while AMD3100 can suppress some aspects of leukocyte infiltration and acute neuroinflammation, broad alteration of CXCR4-dependent trafficking may also perturb reparative myeloid subsets (Dabrowska et al., 2019; Jujo et al., 2013). Furthermore, CXCL12–CXCR4 signaling is involved in recruiting neural and endothelial progenitor cells, promoting angiogenesis and neurogenesis, and attracting protective natural killer cells to ischemic lesions (Wang et al., 2023; Xiao et al., 2025). Prolonged or poorly timed CXCR4 blockade could therefore impair vascular remodeling, progenitor engraftment, and innate immune protection. Experimental data also indicate that AMD3100 can inhibit neural stem cell migration and differentiation, raising concern that chronic or late-phase inhibition might interfere with endogenous repair (Liu et al., 2017). These considerations suggest that any translational use of CXCR4 antagonists in ischemia–reperfusion would require careful selection of the time window, limiting treatment to the acute or subacute phase in which pyroptotic microglia and destructive inflammation predominate, and avoiding extended exposure during recovery

phases that depend on CXCR4-mediated regenerative processes. The route of administration and tissue specificity represent additional challenges. Most stroke studies have relied on systemic (intraperitoneal or intravenous) dosing, which exposes peripheral organs, bone marrow, and the entire immune system to CXCR4 blockade. Alternative delivery strategies, including intrathecal administration or targeted nanoparticle-based delivery, have been explored in other ischemia–reperfusion and pain models and can reduce glial activation and cytokine release in the central nervous system while limiting systemic exposure (Li et al., 2016; Zinnhardt et al., 2018). In light of the present findings that CXCR4-dependent amplification of pyroptotic execution appears most pronounced in a specific interferon-responsive microglial subset, future interventions might aim for microglia-enriched or lesion-localized delivery rather than global CXCR4 blockade. Possible approaches include microglia-targeted nanoparticles carrying CXCR4 antagonists, antisense oligonucleotides, or siRNAs, as well as biodegradable matrices or intranasal formulations designed to concentrate drug in perivascular and parenchymal compartments while minimizing effects on bone marrow and peripheral progenitor niches.

Finally, the current data point toward several directions for next-generation CXCR4-targeted therapies. Rather than full antagonism, biased or partial inhibitors that preferentially disrupt the coupling between CXCR4 and downstream inflammasome–caspase-1–GSDMD signaling, while preserving pathways involved in angiogenesis and progenitor recruitment, may offer a more favorable risk–benefit profile. Small molecules and natural compounds that indirectly inhibit the CXCL12/CXCR4 axis and its downstream JAK2/STAT3 or PI3K/AKT/NF-κB signaling have already shown promise in reducing neuroinflammation in experimental models. In parallel, combinatorial strategies that pair CXCR4 modulation with direct inhibitors of pyroptosis components such as NLRP3, caspase-1, or GSDMD might allow lower CXCR4 inhibitor doses and shorter treatment durations, thereby reducing systemic side effects. From the perspective of the present study, such approaches would aim to selectively blunt the execution arm of microglial pyroptosis in the acute phase of ischemia–reperfusion, while preserving microglial chemotaxis, phagocytic clearance of debris, and later reparative functions. Careful in vivo experiments that integrate conditional microglial

CXCR4 deletion, time-resolved readouts of pyroptosis and regeneration, and graded pharmacologic regimens will be essential to define the therapeutic window in which CXCR4 inhibition can be leveraged to improve outcome without compromising endogenous repair.

5 ABSTRACT

Cerebral ischemia–reperfusion injury elicits rapid sterile inflammation in which microglia undergo marked state transitions and can contribute to secondary tissue damage. Pyroptosis, executed by gasdermin D cleavage and pore formation, has been implicated in amplification of neuroinflammation, while the chemokine receptor CXCR4 is induced after stroke and may intersect with inflammatory execution pathways. This thesis investigated the role of CXCR4 in microglial pyroptosis after ischemia–reperfusion and evaluated whether pharmacological CXCR4 blockade with AMD3100 attenuates acute pyroptotic execution. Public datasets were reanalyzed, including bulk RNA sequencing of microglia three days after 60-min middle cerebral artery occlusion (MCAO) with reperfusion and brain-wide single-cell RNA sequencing 24 h after MCAO or sham. Bulk RNA-seq identified extensive transcriptional remodeling and significant induction of CXCR4 together with prominent inflammatory, and enrichment analyses mapped CXCR4-containing programs to chemokine signaling, chemotaxis, cytoskeletal remodeling, and receptor trafficking. Single-cell analysis resolved eight microglial states indicating pronounced post-ischemic heterogeneity. Pyroptosis-related module scores were broadly reduced across most MCAO-associated states but increased in the interferon-responsive state. CXCR4-axis activity showed weak yet significant positive associations with pyroptosis composite and execution programs after ischemia–reperfusion, whereas no significant correlations were detected in sham microglia, and a network-based virtual CXCR4 knockout suggested the most coherent attenuation of pyroptosis-related regulation in the interferon-responsive microglial state. For in vitro validation, primary mouse microglia were subjected to oxygen–glucose deprivation followed by reoxygenation (OGD/RO). CXCR4 protein increased transiently and peaked at 6 h OGD with 12 h reoxygenation. Under this condition, AMD3100 treatment reduced the cleaved GSDMD N-terminal fragment without altering full-length GSDMD and was accompanied by reduced membrane-associated GSDMD patterns and partial morphological normalization. Collectively, these findings support a model in which CXCR4 contributes to microglial pyroptotic execution in a time- and state-dependent manner after ischemia–reperfusion and indicate CXCR4 antagonism as a potential strategy to dampen acute inflammatory injury.

6 ZUSAMMENFASSUNG

Zerebrale Ischämie–Reperfusionsschädigung löst eine rasche sterile Entzündungsreaktion aus, in deren Verlauf Mikroglia ausgeprägte Zustandswechsel durchlaufen und zur sekundären Gewebeschädigung beitragen können. Die Pyroptose, die durch Spaltung von Gasdermin D und nachfolgende Porenbildung ausgeführt wird, gilt als Mechanismus der neuroinflammatorischen Amplifikation. Der Chemokinrezeptor CXCR4 wird nach Schlaganfall induziert und könnte mit inflammatorischen Ausführungsprogrammen interagieren. Ziel dieser Arbeit war es, die Rolle von CXCR4 in der mikroglialen Pyroptose nach Ischämie–Reperfusion zu untersuchen und zu prüfen, ob eine pharmakologische CXCR4-Blockade durch AMD3100 die akute pyroptotische Ausführung abschwächt. Hierzu wurden öffentliche Datensätze reanalysiert, darunter Bulk-RNA-Sequenzierungen von Mikroglia drei Tage nach 60-minütigem Verschluss der Arteria cerebri media (MCAO) mit Reperfusion sowie eine hirnweite Single-Cell-RNA-Sequenzierung 24 h nach MCAO oder Sham-Operation. Die Bulk-RNA-seq zeigte eine ausgeprägte transkriptionelle Remodellierung mit signifikanter Induktion von CXCR4 bei gleichzeitig ausgeprägter inflammatorischer Aktivierung. Anreicherungsanalysen ordneten CXCR4-assoziierte Programme Chemokinsignalwegen, Chemotaxis, zytoskelettaler Remodellierung und Rezeptor-Trafficking zu. Die Single-Cell-Analyse identifizierte acht Mikroglia-Zustände, die unterschiedliche Programme umfassten und damit eine ausgeprägte postischämische Heterogenität belegten. Pyroptose-bezogene Modul-Scores waren in den meisten MCAO-assoziierten Zuständen insgesamt vermindert, jedoch im interferon-responsiven Zustand erhöht. Die Aktivität der CXCR4-Achse zeigte nach Ischämie–Reperfusion schwache, jedoch signifikante positive Assoziationen mit pyroptotischen Komposit- und Ausführungsprogrammen, während in Sham-Mikroglia keine signifikanten Korrelationen nachweisbar waren. Ein netzwerkbasiertes virtuelles CXCR4-Knockout wies auf die kohärenteste Abschwächung pyroptosebezogener Regulation im interferon-responsiven Mikroglia-Zustand hin. Zur in-vitro-Validierung wurden primäre murine Mikroglia einer Sauerstoff-Glukose-Deprivation mit anschließender Reoxygenierung (OGD/RO) unterzogen. Das CXCR4-Protein nahm transient zu und erreichte ein Maximum bei 6 h OGD und 12 h Reoxygenierung. Unter dieser Bedingung reduzierte AMD3100 das gespaltene GSDMD-N-terminale Fragment, ohne das Volllängen-GSDMD zu verändern, und war mit verminderten membranassoziierten GSDMD-Musterungen sowie einer teilweisen morphologischen Normalisierung assoziiert. Insgesamt stützen diese Ergebnisse ein Modell, nach dem CXCR4 in zeit- und zustandsabhängiger Weise zur mikroglialen pyroptotischen Ausführung nach Ischämie–Reperfusion beiträgt, und weisen auf CXCR4-Antagonismus als potenzielle Strategie zur Dämpfung akuter inflammatorischer Schädigungsprozesse hin.

7 BIBLIOGRAPHY

Adibhatla, R. M., & Hatcher, J. F. (2008). Phospholipase A(2), reactive oxygen species, and lipid peroxidation in CNS pathologies. *BMB Rep*, *41*(8), 560-567. https://doi.org/10.5483/bmbrep.2008.41.8.560

Aglietti, R. A., & Dueber, E. C. (2017). Recent Insights into the Molecular Mechanisms Underlying Pyroptosis and Gasdermin Family Functions. *Trends Immunol*, *38*(4), 261-271. https://doi.org/10.1016/j.it.2017.01.003

Anaya-Fernández, R., Anaya-Prado, R., Anaya-Fernández, M., Guerrero-Palomera, M., Garcia-Ramirez, I., Gonzalez-Martinez, D., Azcona-Ramirez, C., Guerrero-Palomera, C., Garcia-Perez, C., Tenorio-Gonzalez, B., Tenorio-Gonzalez, J., Vargas-Ascencio, L., Canseco-Villegas, A., Servin-Romero, G., Barragan-Arias, A., & Reyna-Rodriguez, B. (2024). Oxidative Stress in Cerebral Ischemia/Reperfusion Injury. *OBM Neurobiology*. https://doi.org/10.21926/obm.neurobiol.2403239

Anderson, M. F., & Sims, N. R. (2002). The effects of focal ischemia and reperfusion on the glutathione content of mitochondria from rat brain subregions. *J Neurochem*, *81*(3), 541-549. https://doi.org/10.1046/j.1471-4159.2002.00836.x

Asahi, M., Wang, X., Mori, T., Sumii, T., Jung, J. C., Moskowitz, M. A., Fini, M. E., & Lo, E. H. (2001). Effects of matrix metalloproteinase-9 gene knock-out on the proteolysis of blood-brain barrier and white matter components after cerebral ischemia. *J Neurosci*, *21*(19), 7724-7732. https://doi.org/10.1523/jneurosci.21-19-07724.2001

Azam, S., Jakaria, M., Kim, I. S., Kim, J., Haque, M. E., & Choi, D. K. (2019). Regulation of Toll-Like Receptor (TLR) Signaling Pathway by Polyphenols in the Treatment of Age-Linked Neurodegenerative Diseases: Focus on TLR4 Signaling. *Front Immunol*, *10*, 1000. https://doi.org/10.3389/fimmu.2019.01000

Banerjee, I., Behl, B., Mendonça, M., Shrivastava, G., Russo, A., Ménoret, A., Ghosh, A., Vella, A., Vanaja, S., Sarkar, S., Fitzgerald, K., & Rathinam, V. (2018). Gasdermin D Restrains Type I Interferon Response to Cytosolic DNA by Disrupting Ionic Homeostasis. *Immunity*, *49*, 413. https://doi.org/10.1016/j.immuni.2018.07.006

Bedard, K., & Krause, K. H. (2007). The NOX family of ROS-generating NADPH oxidases: physiology and pathophysiology. *Physiol Rev*, *87*(1), 245-313. https://doi.org/10.1152/physrev.00044.2005

Bernardi, P., Rasola, A., Forte, M., & Lippe, G. (2015). The Mitochondrial Permeability Transition Pore: Channel Formation by F-ATP Synthase, Integration in Signal Transduction, and Role in Pathophysiology. *Physiol Rev*, *95*(4), 1111-1155. https://doi.org/10.1152/physrev.00001.2015

Brint, A., Greene, S., Fennig-Victor, A. R., & Wang, S. (2024). Multiple sclerosis: the NLRP3 inflammasome, gasdermin D, and therapeutics. *Ann Transl Med*, *12*(4), 62. https://doi.org/10.21037/atm-23-1960

Broz, P., & Dixit, V. M. (2016). Inflammasomes: mechanism of assembly, regulation and signalling. *Nat Rev Immunol*, *16*(7), 407-420. https://doi.org/10.1038/nri.2016.58

Bui, T. A., Jickling, G. C., & Winship, I. R. (2022). Neutrophil dynamics and inflammaging in acute ischemic stroke: A transcriptomic review. *Front Aging Neurosci*, *14*, 1041333. https://doi.org/10.3389/fnagi.2022.1041333

Cambier, S., Gouwy, M., & Proost, P. (2023). The chemokines CXCL8 and CXCL12: molecular and functional properties, role in disease and efforts towards pharmacological intervention. *Cellular and Molecular Immunology*, *20*, 217-251. https://doi.org/10.1038/s41423-023-00974-6

Chen, H., He, Y., Chen, S., Qi, S., & Shen, J. (2020). Therapeutic targets of oxidative/nitrosative stress and neuroinflammation in ischemic stroke: Applications for natural product efficacy with omics and systemic biology. *Pharmacol Res*, *158*, 104877. https://doi.org/10.1016/j.phrs.2020.104877

Chen, J., Chen, J., Chen, S., Zhang, C., Zhang, L., Xiao, X., Das, A., Zhao, Y., Yuan, B., Morris, M., Zhao, B., & Chen, Y. (2012). Transfusion of CXCR4-primed endothelial progenitor cells reduces cerebral ischemic damage and promotes repair in db/db diabetic mice. *PLoS One*, *7*(11), e50105. https://doi.org/10.1371/journal.pone.0050105

Cheng, K.-I., Chen, S.-L., Hsu, J.-H., Cheng, Y.-C., Chang, Y.-C., Lee, C.-H., Yeh, J.-L., Dai, Z.-K., & Wu, B.-N. (2021). Loganin prevents CXCL12/CXCR4-regulated neuropathic pain via the NLRP3 inflammasome axis in nerve-injured rats. *Phytomedicine*, *92*, 153734. https://doi.org/https://doi.org/10.1016/j.phymed.2021.153734

Cheng, S. M., Ho, C. L., Chen, S. L., Huang, Y. T., Mao, P. C., Lin, T. C., Chen, J. S., Sun, H. S., Hwang, D. Y., & Chu, C. H. (2025). Functional Diversity of Two Novel Embryonic Microglial Subpopulations and Their Developmental Trajectories in Developing Mouse Brains. *Glia*, *73*(11), 2236-2252. https://doi.org/10.1002/glia.70064

Cheng, X., Wang, H., Zhang, X., Zhao, S., Zhou, Z., Mu, X., Zhao, C., & Teng, W. (2017). The Role of SDF-1/CXCR4/CXCR7 in Neuronal Regeneration after Cerebral Ischemia. *Front Neurosci*, *11*, 590. https://doi.org/10.3389/fnins.2017.00590

Choi, D. W. (2020). Excitotoxicity: Still Hammering the Ischemic Brain in 2020. *Front Neurosci*, *14*, 579953. https://doi.org/10.3389/fnins.2020.579953

Cooke, M. S., Evans, M. D., Dizdaroglu, M., & Lunec, J. (2003). Oxidative DNA damage: mechanisms, mutation, and disease. *Faseb j*, *17*(10), 1195-1214. https://doi.org/10.1096/fj.02-0752rev

Dabrowska, S., Andrzejewska, A., Lukomska, B., & Janowski, M. (2019). Neuroinflammation as a target for treatment of stroke using mesenchymal stem cells and extracellular vesicles. *J Neuroinflammation*, *16*(1), 178. https://doi.org/10.1186/s12974-019-1571-8

Davalos, D., Grutzendler, J., Yang, G., Kim, J. V., Zuo, Y., Jung, S., Littman, D. R., Dustin, M. L., & Gan, W. B. (2005). ATP mediates rapid microglial response to local brain injury in vivo. *Nat Neurosci*, *8*(6), 752-758. https://doi.org/10.1038/nn1472

Dawson, T. M., & Dawson, V. L. (2018). Nitric Oxide Signaling in Neurodegeneration and Cell Death. *Adv Pharmacol*, *82*, 57-83. https://doi.org/10.1016/bs.apha.2017.09.003

Denorme, F., Portier, I., Rustad, J. L., Cody, M. J., de Araujo, C. V., Hoki, C., Alexander, M. D., Grandhi, R., Dyer, M. R., Neal, M. D., Majersik, J. J., Yost, C. C., & Campbell, R. A. (2022). Neutrophil extracellular traps regulate ischemic stroke brain injury. *J Clin Invest*, *132*(10). https://doi.org/10.1172/jci154225

Devine, S. M., Flomenberg, N., Vesole, D. H., Liesveld, J., Weisdorf, D., Badel, K., Calandra, G., & DiPersio, J. F. (2004). Rapid mobilization of CD34+ cells following administration of the CXCR4 antagonist AMD3100 to patients with multiple myeloma and non-Hodgkin's lymphoma. *J Clin Oncol*, *22*(6), 1095-1102. https://doi.org/10.1200/jco.2004.07.131

Diepenhorst, G. M., van Gulik, T. M., & Hack, C. E. (2009). Complement-mediated ischemia-reperfusion injury: lessons learned from animal and clinical studies. *Ann Surg*, *249*(6), 889-899. https://doi.org/10.1097/SLA.0b013e3181a38f45

Ding, J., Wang, K., Liu, W., She, Y., Sun, Q., Shi, J., Sun, H., Wang, D. C., & Shao, F. (2016). Pore-forming activity and structural autoinhibition of the gasdermin family. *Nature*, *535*(7610), 111-116. https://doi.org/10.1038/nature18590

Du, S., Xiong, S., Du, X., Yuan, T. F., Peng, B., & Rao, Y. (2021). Primary Microglia Isolation from Postnatal Mouse Brains. *J Vis Exp*(168). https://doi.org/10.3791/62237

Emir, S., Demir, H. A., Aksu, T., Kara, A., Özgüner, M., & Tunç, B. (2014). Use of plerixafor for peripheral blood stem cell mobilization failure in children. *Transfus Apher Sci*, *50*(2), 214-218. https://doi.org/10.1016/j.transci.2013.12.017

Feigin, V. L., Brainin, M., Norrving, B., Martins, S. O., Pandian, J., Lindsay, P., M, F. G., & Rautalin, I. (2025). World Stroke Organization: Global Stroke Fact Sheet 2025. *Int J Stroke*, *20*(2), 132-144. https://doi.org/10.1177/17474930241308142

Feigin, V. L., & Owolabi, M. O. (2023). Pragmatic solutions to reduce the global burden of stroke: a World Stroke Organization-Lancet Neurology Commission. *Lancet Neurol*, *22*(12), 1160-1206. https://doi.org/10.1016/s1474-4422(23)00277-6

Garcia, J. M., Stillings, S. A., Leclerc, J. L., Phillips, H., Edwards, N. J., Robicsek, S. A., Hoh, B. L., Blackburn, S., & Doré, S. (2017). Role of Interleukin-10 in Acute Brain Injuries. *Front Neurol*, *8*, 244. https://doi.org/10.3389/fneur.2017.00244

Gerkau, N. J., Rakers, C., Durry, S., Petzold, G. C., & Rose, C. R. (2017). Reverse NCX Attenuates Cellular Sodium Loading in Metabolically Compromised Cortex. *Cerebral Cortex*, *28*(12), 4264-4280. https://doi.org/10.1093/cercor/bhx280

Ginhoux, F., Greter, M., Leboeuf, M., Nandi, S., See, P., Gokhan, S., Mehler, M. F., Conway, S. J., Ng, L. G., Stanley, E. R., Samokhvalov, I. M., & Merad, M. (2010). Fate mapping analysis reveals that adult microglia derive from primitive macrophages. *Science*, *330*(6005), 841-845. https://doi.org/10.1126/science.1194637

Global, regional, and national burden of stroke and its risk factors, 1990-2021: a systematic analysis for the Global Burden of Disease Study 2021. (2024).

Lancet Neurol, *23*(10), 973-1003. https://doi.org/10.1016/s1474-4422(24)00369-7

Gomez Perdiguero, E., Klapproth, K., Schulz, C., Busch, K., Azzoni, E., Crozet, L., Garner, H., Trouillet, C., de Bruijn, M. F., Geissmann, F., & Rodewald, H. R. (2015). Tissue-resident macrophages originate from yolk-sac-derived erythro-myeloid progenitors. *Nature*, *518*(7540), 547-551. https://doi.org/10.1038/nature13989

Gu, R., Wang, L., Zhou, H., Wang, X., Lenahan, C., Qu, H., Liu, Y., Li, S., Wei, C., Han, L., Hu, X., & Zuo, G. (2021). Rh-CXCL-12 Attenuates Neuronal Pyroptosis after Subarachnoid Hemorrhage in Rats via Regulating the CXCR4/NLRP1 Pathway. *Oxid Med Cell Longev*, *2021*, 6966394. https://doi.org/10.1155/2021/6966394

Gülke, E., Gelderblom, M., & Magnus, T. (2018). Danger signals in stroke and their role on microglia activation after ischemia. *Therapeutic Advances in Neurological Disorders*, *11*. https://doi.org/10.1177/1756286418774254

Guo, C., & Ma, Y. Y. (2021). Calcium Permeable-AMPA Receptors and Excitotoxicity in Neurological Disorders. *Front Neural Circuits*, *15*, 711564. https://doi.org/10.3389/fncir.2021.711564

Hammond, T. R., Dufort, C., Dissing-Olesen, L., Giera, S., Young, A., Wysoker, A., Walker, A. J., Gergits, F., Segel, M., Nemesh, J., Marsh, S. E., Saunders, A., Macosko, E., Ginhoux, F., Chen, J., Franklin, R. J. M., Piao, X., McCarroll, S. A., & Stevens, B. (2019). Single-Cell RNA Sequencing of Microglia throughout the Mouse Lifespan and in the Injured Brain Reveals Complex Cell-State Changes. *Immunity*, *50*(1), 253-271.e256. https://doi.org/10.1016/j.immuni.2018.11.004

He, W. T., Wan, H., Hu, L., Chen, P., Wang, X., Huang, Z., Yang, Z. H., Zhong, C. Q., & Han, J. (2015). Gasdermin D is an executor of pyroptosis and required for interleukin-1β secretion. *Cell Res*, *25*(12), 1285-1298. https://doi.org/10.1038/cr.2015.139

Heuninck, J., Viciano, C. P., Işbilir, A., Caspar, B., Capoferri, D., Briddon, S., Durroux, T., Hill, S., Lohse, M., Milligan, G., Pin, J., & Hoffmann, C. (2019). Context-dependent signalling of CXC chemokine receptor 4 (CXCR4) and atypical chemokine receptor 3 (ACKR3). *Molecular pharmacology*. https://doi.org/10.1124/mol.118.115477

Hickman, S., Izzy, S., Sen, P., Morsett, L., & El Khoury, J. (2018). Microglia in neurodegeneration. *Nat Neurosci*, *21*(10), 1359-1369. https://doi.org/10.1038/s41593-018-0242-x

Hill, W. D., Hess, D. C., Martin-Studdard, A., Carothers, J. J., Zheng, J., Hale, D., Maeda, M., Fagan, S. C., Carroll, J. E., & Conway, S. J. (2004). SDF-1 (CXCL12) is upregulated in the ischemic penumbra following stroke: association with bone marrow cell homing to injury. *J Neuropathol Exp Neurol*, *63*(1), 84-96. https://doi.org/10.1093/jnen/63.1.84

Hong, S., Beja-Glasser, V. F., Nfonoyim, B. M., Frouin, A., Li, S., Ramakrishnan, S., Merry, K. M., Shi, Q., Rosenthal, A., Barres, B. A., Lemere, C. A., Selkoe, D. J., & Stevens, B. (2016). Complement and microglia mediate early synapse loss in Alzheimer mouse models. *Science*, *352*(6286), 712-716. https://doi.org/10.1126/science.aad8373

Huang, H., Chen, Y. M., Zhu, F., Tang, S. T., Xiao, J. D., Li, L. L., & Lin, X. J. (2015). Down-regulated Na(+)/K(+)-ATPase activity in ischemic penumbra after focal cerebral ischemia/reperfusion in rats. *Int J Clin Exp Pathol*, *8*(10), 12708-12717.

Huang, J., Li, Y., Tang, Y., Tang, G., Yang, G.-Y., & Wang, Y. (2013). CXCR4 Antagonist AMD3100 Protects Blood–Brain Barrier Integrity and Reduces Inflammatory Response After Focal Ischemia in Mice. *Stroke*, *44*, 190. https://doi.org/10.1161/strokeaha.112.670299

Huang, J., Li, Y., Tang, Y., Tang, G., Yang, G. Y., & Wang, Y. (2013). CXCR4 antagonist AMD3100 protects blood-brain barrier integrity and reduces inflammatory response after focal ischemia in mice. *Stroke*, *44*(1), 190-197. https://doi.org/10.1161/strokeaha.112.670299

Iadecola, C., & Anrather, J. (2011). The immunology of stroke: from mechanisms to translation. *Nat Med*, *17*(7), 796-808. https://doi.org/10.1038/nm.2399

Inose, Y., Kato, Y., Kitagawa, K., Uchiyama, S., & Shibata, N. (2015). Activated microglia in ischemic stroke penumbra upregulate MCP-1 and CCR2 expression in response to lysophosphatidylcholine derived from adjacent neurons and astrocytes. *Neuropathology*, *35*(3), 209-223. https://doi.org/10.1111/neup.12182

Janda, E., Boi, L., & Carta, A. R. (2018). Microglial Phagocytosis and Its Regulation: A Therapeutic Target in Parkinson's Disease? *Front Mol Neurosci*, *11*, 144. https://doi.org/10.3389/fnmol.2018.00144

Jia, J., Yang, L., Chen, Y., Zheng, L., Chen, Y., Xu, Y., & Zhang, M. (2021). The Role of Microglial Phagocytosis in Ischemic Stroke. *Front Immunol*, *12*, 790201. https://doi.org/10.3389/fimmu.2021.790201

Jin, W. N., Gonzales, R., Feng, Y., Wood, K., Chai, Z., Dong, J. F., La Cava, A., Shi, F. D., & Liu, Q. (2018). Brain Ischemia Induces Diversified Neuroantigen-Specific T-Cell Responses That Exacerbate Brain Injury. *Stroke*, *49*(6), 1471-1478. https://doi.org/10.1161/strokeaha.118.020203

Jujo, K., Ii, M., Sekiguchi, H., Klyachko, E., Misener, S., Tanaka, T., Tongers, J., Roncalli, J., Renault, M. A., Thorne, T., Ito, A., Clarke, T., Kamide, C., Tsurumi, Y., Hagiwara, N., Qin, G., Asahi, M., & Losordo, D. W. (2013). CXC-chemokine receptor 4 antagonist AMD3100 promotes cardiac functional recovery after ischemia/reperfusion injury via endothelial nitric oxide synthase-dependent mechanism. *Circulation*, *127*(1), 63-73. https://doi.org/10.1161/circulationaha.112.099242

Jung, E. S., Choi, H., & Mook-Jung, I. (2025). Decoding microglial immunometabolism: a new frontier in Alzheimer's disease research. *Mol Neurodegener*, *20*(1), 37. https://doi.org/10.1186/s13024-025-00825-0

Jung, H., Lee, D., You, H., Lee, M., Kim, H., Cheong, E., & Um, J. W. (2023). LPS induces microglial activation and GABAergic synaptic deficits in the hippocampus accompanied by prolonged cognitive impairment. *Sci Rep*, *13*(1), 6547. https://doi.org/10.1038/s41598-023-32798-9

Keller, J. N., Mark, R. J., Bruce, A. J., Blanc, E., Rothstein, J. D., Uchida, K., Waeg, G., & Mattson, M. P. (1997). 4-Hydroxynonenal, an aldehydic product of mem-

brane lipid peroxidation, impairs glutamate transport and mitochondrial function in synaptosomes. *Neuroscience*, *80*(3), 685-696. https://doi.org/10.1016/s0306-4522(97)00065-1

Lai, K., Pritišanac, I., Liu, Z. Q., Liu, H. W., Gong, L. N., Li, M. X., Lu, J. F., Qi, X., Xu, T. L., Forman-Kay, J., Shi, H. B., Wang, L. Y., & Yin, S. K. (2024). Glutamate acts on acid-sensing ion channels to worsen ischaemic brain injury. *Nature*, *631*(8022), 826-834. https://doi.org/10.1038/s41586-024-07684-7

Lai, T. W., Zhang, S., & Wang, Y. T. (2014). Excitotoxicity and stroke: identifying novel targets for neuroprotection. *Prog Neurobiol*, *115*, 157-188. https://doi.org/10.1016/j.pneurobio.2013.11.006

Lampron, A., Larochelle, A., Laflamme, N., Préfontaine, P., Plante, M. M., Sánchez, M. G., Yong, V. W., Stys, P. K., Tremblay, M., & Rivest, S. (2015). Inefficient clearance of myelin debris by microglia impairs remyelinating processes. *J Exp Med*, *212*(4), 481-495. https://doi.org/10.1084/jem.20141656

Lawson, L. J., Perry, V. H., Dri, P., & Gordon, S. (1990). Heterogeneity in the distribution and morphology of microglia in the normal adult mouse brain. *Neuroscience*, *39*(1), 151-170. https://doi.org/10.1016/0306-4522(90)90229-w

Lee, S., Hirohama, M., Noguchi, M., Nagata, K., & Kawaguchi, A. (2018). Influenza A Virus Infection Triggers Pyroptosis and Apoptosis of Respiratory Epithelial Cells through the Type I Interferon Signaling Pathway in a Mutually Exclusive Manner. *Journal of Virology*, *92*. https://doi.org/10.1128/jvi.00396-18

Legros, H., Launay, S., Roussel, B. D., Marcou-Labarre, A., Calbo, S., Catteau, J., Leroux, P., Boyer, O., Ali, C., Marret, S., Vivien, D., & Laudenbach, V. (2009). Newborn- and adult-derived brain microvascular endothelial cells show age-related differences in phenotype and glutamate-evoked protease release. *J Cereb Blood Flow Metab*, *29*(6), 1146-1158. https://doi.org/10.1038/jcbfm.2009.39

Leyh, J., Paeschke, S., Mages, B., Michalski, D., Nowicki, M., Bechmann, I., & Winter, K. (2021). Classification of Microglial Morphological Phenotypes Using Machine Learning. *Front Cell Neurosci*, *15*, 701673. https://doi.org/10.3389/fncel.2021.701673

Li, D., Sun, H., Li, W.-Z., & Zhang, X. (2018). Protective effects of AMD3100 on ischemic stroke by inhibiting inflammation and promoting angiogenesis and neuranagenesis. https://consensus.app/papers/protective-effects-of-amd3100-on-ischemic-stroke-by-li-sun/a957e1f47da75f448e38258dbee137c7/

Li, H., Liu, P., Zhang, B., Yuan, Z., Guo, M., Zou, X., Qian, Y., Deng, S., Zhu, L., Cao, X., Tao, T., Xia, S., Bao, X., & Xu, Y. (2023). Acute ischemia induces spatially and transcriptionally distinct microglial subclusters. *Genome Med*, *15*(1), 109. https://doi.org/10.1186/s13073-023-01257-5

Li, L., Dickinson, M., Coers, J., & Miao, E. (2023). Pyroptosis in defense against intracellular bacteria. *Seminars in immunology*, *69*, 101805. https://doi.org/10.1016/j.smim.2023.101805

Li, Q., Cao, Y., Dang, C., Han, B., Han, R., Ma, H., Hao, J., & Wang, L. (2020). Inhibition of double-strand DNA-sensing cGAS ameliorates brain injury after ischemic stroke. *EMBO Mol Med*, *12*(4), e11002. https://doi.org/10.15252/emmm.201911002

Li, Q., Cheng, Z., Zhou, L., Darmanis, S., Neff, N. F., Okamoto, J., Gulati, G., Bennett, M. L., Sun, L. O., Clarke, L. E., Marschallinger, J., Yu, G., Quake, S. R., Wyss-Coray, T., & Barres, B. A. (2019). Developmental Heterogeneity of Microglia and Brain Myeloid Cells Revealed by Deep Single-Cell RNA Sequencing. *Neuron*, *101*(2), 207-223.e210. https://doi.org/10.1016/j.neuron.2018.12.006

Li, W., Shen, N., Kong, L., Huang, H., Wang, X., Zhang, Y., Wang, G., Xu, P., & Hu, W. (2024). STING mediates microglial pyroptosis via interaction with NLRP3 in cerebral ischaemic stroke. *Stroke Vasc Neurol*, *9*(2), 153-164. https://doi.org/10.1136/svn-2023-002320

Li, X., Zhang, Y., Wang, Y., Zhao, D., Sun, C., Zhou, S., Xu, D., & Zhao, J. (2020). Exosomes Derived from CXCR4-Overexpressing BMSC Promoted Activation of Microvascular Endothelial Cells in Cerebral Ischemia/Reperfusion Injury. *Neural Plasticity*, *2020*. https://doi.org/10.1155/2020/8814239

Li, X., Zhang, Y., Wang, Y., Zhao, D., Sun, C., Zhou, S., Xu, D., & Zhao, J. (2020). Exosomes Derived from CXCR4-Overexpressing BMSC Promoted Activation of Microvascular Endothelial Cells in Cerebral Ischemia/Reperfusion Injury. *Neural Plast*, *2020*, 8814239. https://doi.org/10.1155/2020/8814239

Li, X. Q., Zhang, Z. L., Tan, W. F., Sun, X. J., & Ma, H. (2016). Down-Regulation of CXCL12/CXCR4 Expression Alleviates Ischemia-Reperfusion-Induced Inflammatory Pain via Inhibiting Glial TLR4 Activation in the Spinal Cord. *PLoS One*, *11*(10), e0163807. https://doi.org/10.1371/journal.pone.0163807

Li, Y., Guo, X., Hu, C., Du, Y., Guo, C., Wang, D., Zhao, W., Huang, G., Li, C., Lu, Q., Lai, R., Xu, T., & Qi, X. (2018). Type I IFN operates pyroptosis and necroptosis during multidrug-resistant A. baumannii infection. *Cell Death & Differentiation*, *25*, 1304-1318. https://doi.org/10.1038/s41418-017-0041-z

Liston, A., & Masters, S. L. (2017). Homeostasis-altering molecular processes as mechanisms of inflammasome activation. *Nat Rev Immunol*, *17*(3), 208-214. https://doi.org/10.1038/nri.2016.151

Liu, C., Yao, K., Tian, Q., Guo, Y., Wang, G., He, P.-N., Wang, J., Wang, J., Zhang, Z., & Li, M. (2023). CXCR4-BTK axis mediate pyroptosis and lipid peroxidation in early brain injury after subarachnoid hemorrhage via NLRP3 inflammasome and NF-κB pathway. *Redox Biology*, *68*. https://doi.org/10.1016/j.redox.2023.102960

Liu, C., Yao, K., Tian, Q., Guo, Y., Wang, G., He, P., Wang, J., Wang, J., Zhang, Z., & Li, M. (2023). CXCR4-BTK axis mediate pyroptosis and lipid peroxidation in early brain injury after subarachnoid hemorrhage via NLRP3 inflammasome and NF-κB pathway. *Redox Biol*, *68*, 102960. https://doi.org/10.1016/j.redox.2023.102960

Liu, J. M., Zhao, K., Du, L. X., Zhou, Y., Long, X. H., Chen, X. Y., & Liu, Z. L. (2017). AMD3100 inhibits the migration and differentiation of neural stem cells after spinal cord injury. *Sci Rep*, *7*(1), 64. https://doi.org/10.1038/s41598-017-00141-8

Liu, T., Li, X., You, S., Bhuyan, S. S., & Dong, L. (2015). Effectiveness of AMD3100 in treatment of leukemia and solid tumors: from original discovery to use in current clinical practice. *Exp Hematol Oncol*, *5*, 19. https://doi.org/10.1186/s40164-016-0050-5

Liu, Y., Dong, J., Zhang, Z., Liu, Y., & Wang, Y. (2023). Regulatory T cells: A suppressor arm in post-stroke immune homeostasis. *Neurobiol Dis*, *189*, 106350. https://doi.org/10.1016/j.nbd.2023.106350

Lücht, J., Rolfs, N., Wowro, S. J., Berger, F., Schmitt, K. R. L., & Tong, G. (2021). Cooling and Sterile Inflammation in an Oxygen-Glucose-Deprivation/Reperfusion Injury Model in BV-2 Microglia. *Mediators Inflamm*, *2021*, 8906561. https://doi.org/10.1155/2021/8906561

Mandrekar, S., Jiang, Q., Lee, C. Y., Koenigsknecht-Talboo, J., Holtzman, D. M., & Landreth, G. E. (2009). Microglia mediate the clearance of soluble Abeta through fluid phase macropinocytosis. *J Neurosci*, *29*(13), 4252-4262. https://doi.org/10.1523/jneurosci.5572-08.2009

Martynov, M. Y., Zhuravleva, M. V., Vasyukova, N. S., Kuznetsova, E. V., & Kameneva, T. R. (2023). [Oxidative stress in the pathogenesis of stroke and its correction]. *Zh Nevrol Psikhiatr Im S S Korsakova*, *123*(1), 16-27. https://doi.org/10.17116/jnevro202312301116 (Okislitel'nyi stress v patogeneze tserebral'nogo insul'ta i ego korrektsiya.)

Matejuk, A., & Ransohoff, R. M. (2020). Crosstalk Between Astrocytes and Microglia: An Overview. *Front Immunol*, *11*, 1416. https://doi.org/10.3389/fimmu.2020.01416

Michalettos, G., Walter, H. L., Antunes, A. R. P., Wieloch, T., Talhada, D., & Ruscher, K. (2021). Effect of Anti-inflammatory Treatment with AMD3100 and CX(3)CR1 Deficiency on GABA(A) Receptor Subunit and Expression of Glutamate Decarboxylase Isoforms After Stroke. *Mol Neurobiol*, *58*(11), 5876-5889. https://doi.org/10.1007/s12035-021-02510-x

Mo, Y., Xu, W., Fu, K., Chen, H., Wen, J., Huang, Q., Guo, F., Mo, L., & Yan, J. (2022). The dual function of microglial polarization and its treatment targets in ischemic stroke. *Front Neurol*, *13*, 921705. https://doi.org/10.3389/fneur.2022.921705

Morrison, H. W., & Filosa, J. A. (2013). A quantitative spatiotemporal analysis of microglia morphology during ischemic stroke and reperfusion. *Journal of Neuroinflammation*, *10*(1), 782. https://doi.org/10.1186/1742-2094-10-4

Neher, J. J., Emmrich, J. V., Fricker, M., Mander, P. K., Théry, C., & Brown, G. C. (2013). Phagocytosis executes delayed neuronal death after focal brain ischemia. *Proc Natl Acad Sci U S A*, *110*(43), E4098-4107. https://doi.org/10.1073/pnas.1308679110

Neumann, J., Sauerzweig, S., Rönicke, R., Gunzer, F., Dinkel, K., Ullrich, O., Gunzer, M., & Reymann, K. G. (2008). Microglia cells protect neurons by direct engulfment of invading neutrophil granulocytes: a new mechanism of CNS immune privilege. *J Neurosci*, *28*(23), 5965-5975. https://doi.org/10.1523/jneurosci.0060-08.2008

Neves, D., Salazar, I. L., Almeida, R. D., & Silva, R. M. (2023). Molecular mechanisms of ischemia and glutamate excitotoxicity. *Life Sci*, *328*, 121814. https://doi.org/10.1016/j.lfs.2023.121814

Nimmerjahn, A., Kirchhoff, F., & Helmchen, F. (2005). Resting microglial cells are highly dynamic surveillants of brain parenchyma in vivo. *Science*, *308*(5726), 1314-1318. https://doi.org/10.1126/science.1110647

Nishizawa, Y. (2001). Glutamate release and neuronal damage in ischemia. *Life Sci*, *69*(4), 369-381. https://doi.org/10.1016/s0024-3205(01)01142-0

Ong, S. B., Samangouei, P., Kalkhoran, S. B., & Hausenloy, D. J. (2015). The mitochondrial permeability transition pore and its role in myocardial ischemia reperfusion injury. *J Mol Cell Cardiol*, *78*, 23-34. https://doi.org/10.1016/j.yjmcc.2014.11.005

Orellana-Urzúa, S., Rojas, I., Líbano, L., & Rodrigo, R. (2020). Pathophysiology of Ischemic Stroke: Role of Oxidative Stress. *Curr Pharm Des*, *26*(34), 4246-4260. https://doi.org/10.2174/1381612826666200708133912

Orihuela, R., McPherson, C. A., & Harry, G. J. (2016). Microglial M1/M2 polarization and metabolic states. *Br J Pharmacol*, *173*(4), 649-665. https://doi.org/10.1111/bph.13139

Orr, A. G., Orr, A. L., Li, X. J., Gross, R. E., & Traynelis, S. F. (2009). Adenosine A(2A) receptor mediates microglial process retraction. *Nat Neurosci*, *12*(7), 872-878. https://doi.org/10.1038/nn.2341

Parkhurst, C. N., Yang, G., Ninan, I., Savas, J. N., Yates, J. R., 3rd, Lafaille, J. J., Hempstead, B. L., Littman, D. R., & Gan, W. B. (2013). Microglia promote learning-dependent synapse formation through brain-derived neurotrophic factor. *Cell*, *155*(7), 1596-1609. https://doi.org/10.1016/j.cell.2013.11.030

Patel, S. (2018). Danger-Associated Molecular Patterns (DAMPs): the Derivatives and Triggers of Inflammation. *Curr Allergy Asthma Rep*, *18*(11), 63. https://doi.org/10.1007/s11882-018-0817-3

Patri, M. (2019). Synaptic Transmission and Amino Acid Neurotransmitters. *Neurochemical Basis of Brain Function and Dysfunction*. https://doi.org/10.5772/intechopen.82121

Pettas, S., Karagianni, K., Kanata, E., Chatziefstathiou, A., Christoudia, N., Xanthopoulos, K., Sklaviadis, T., & Dafou, D. (2022). Profiling Microglia through Single-Cell RNA Sequencing over the Course of Development, Aging, and Disease. *Cells*, *11*(15). https://doi.org/10.3390/cells11152383

Pober, J. S., & Sessa, W. C. (2014). Inflammation and the blood microvascular system. *Cold Spring Harb Perspect Biol*, *7*(1), a016345. https://doi.org/10.1101/cshperspect.a016345

Powers, W. J., Rabinstein, A. A., Ackerson, T., Adeoye, O. M., Bambakidis, N. C., Becker, K., Biller, J., Brown, M., Demaerschalk, B. M., Hoh, B., Jauch, E. C., Kidwell, C. S., Leslie-Mazwi, T. M., Ovbiagele, B., Scott, P. A., Sheth, K. N., Southerland, A. M., Summers, D. V., Tirschwell, D. L., & on behalf of the American Heart Association Stroke, C. (2019). Guidelines for the Early Management of Patients With Acute Ischemic Stroke: 2019 Update to the 2018 Guidelines for the Early Management of Acute Ischemic Stroke: A Guideline for Healthcare Professionals From the American Heart Association/American Stroke Association. *Stroke*, *50*(12), e344-e418. https://doi.org/10.1161/STR.0000000000000211

Rami, A. (2003). Ischemic neuronal death in the rat hippocampus: the calpain-calpastatin-caspase hypothesis. *Neurobiol Dis*, *13*(2), 75-88. https://doi.org/10.1016/s0969-9961(03)00018-4

Ransohoff, R. M. (2016). A polarizing question: do M1 and M2 microglia exist? *Nat Neurosci*, *19*(8), 987-991. https://doi.org/10.1038/nn.4338

Roosen, K., Scheld, M., Mandzhalova, M., Clarner, T., Beyer, C., & Zendedel, A. (2021). CXCL12 inhibits inflammasome activation in LPS-stimulated BV2 cells. *Brain Res*, *1763*, 147446. https://doi.org/10.1016/j.brainres.2021.147446

Rosito, M., Sanchini, C., Gosti, G., Moreno, M., De Panfilis, S., Giubettini, M., Debellis, D., Catalano, F., Peruzzi, G., Marotta, R., Indrieri, A., De Leonibus, E., De Stefano, M. E., Ragozzino, D., Ruocco, G., Di Angelantonio, S., & Bartolini, F. (2023). Microglia reactivity entails microtubule remodeling from acentrosomal to centrosomal arrays. *Cell Rep*, *42*(2), 112104. https://doi.org/10.1016/j.celrep.2023.112104

Rossi, D. J., Oshima, T., & Attwell, D. (2000). Glutamate release in severe brain ischaemia is mainly by reversed uptake. *Nature*, *403*(6767), 316-321. https://doi.org/10.1038/35002090

Ruiz, A., Matute, C., & Alberdi, E. (2009). Endoplasmic reticulum Ca(2+) release through ryanodine and IP(3) receptors contributes to neuronal excitotoxicity. *Cell Calcium*, *46*(4), 273-281. https://doi.org/10.1016/j.ceca.2009.08.005

Sacco, R. L., Kasner, S. E., Broderick, J. P., Caplan, L. R., Connors, J. J., Culebras, A., Elkind, M. S. V., George, M. G., Hamdan, A. D., Higashida, R. T., Hoh, B. L., Janis, L. S., Kase, C. S., Kleindorfer, D. O., Lee, J.-M., Moseley, M. E., Peterson, E. D., Turan, T. N., Valderrama, A. L., & Vinters, H. V. (2013). An Updated Definition of Stroke for the 21st Century. *Stroke*, *44*(7), 2064-2089. https://doi.org/10.1161/STR.0b013e318296aeca

Sah, R. G., d'Esterre, C. D., Hill, M. D., Hafeez, M., Tariq, S., Forkert, N. D., Frayne, R., Demchuk, A. M., Goyal, M., & Barber, P. A. (2019). Diffusion-weighted imaging lesion growth occurs despite recanalization in acute ischemic stroke: Implications for future treatment trials. *Int J Stroke*, *14*(3), 257-264. https://doi.org/10.1177/1747493018798550

Shi, J., Zhao, Y., Wang, K., Shi, X., Wang, Y., Huang, H., Zhuang, Y., Cai, T., Wang, F., & Shao, F. (2015). Cleavage of GSDMD by inflammatory caspases determines pyroptotic cell death. *Nature*, *526*(7575), 660-665. https://doi.org/10.1038/nature15514

Slater, S. (2012). Plerixafor. *J Adv Pract Oncol*, *3*(1), 49-54.

Song, Y., Li, Z., He, T., Qu, M., Jiang, L., Li, W., Shi, X., Pan, J.-J., Zhang, L., Wang, Y., Zhang, Z.-J., Tang, Y., & Yang, G.-Y. (2019). M2 microglia-derived exosomes protect the mouse brain from ischemia-reperfusion injury via exosomal miR-124. *Theranostics*, *9*, 2910-2923. https://doi.org/10.7150/thno.30879

Stadtman, E. R., & Levine, R. L. (2000). Protein oxidation. *Ann N Y Acad Sci*, *899*, 191-208. https://doi.org/10.1111/j.1749-6632.2000.tb06187.x

Stumm, R. K., Rummel, J., Junker, V., Culmsee, C., Pfeiffer, M., Krieglstein, J., Höllt, V., & Schulz, S. (2002). A dual role for the SDF-1/CXCR4 chemokine receptor system in adult brain: isoform-selective regulation of SDF-1 expression modulates CXCR4-dependent neuronal plasticity and cerebral leukocyte recruitment after focal ischemia. *J Neurosci*, *22*(14), 5865-5878. https://doi.org/10.1523/jneurosci.22-14-05865.2002

Stys, P. K. (1998). Anoxic and ischemic injury of myelinated axons in CNS white matter: from mechanistic concepts to therapeutics. *J Cereb Blood Flow Metab*, *18*(1), 2-25. https://doi.org/10.1097/00004647-199801000-00002

Swanson, K. V., Deng, M., & Ting, J. P. (2019). The NLRP3 inflammasome: molecular activation and regulation to therapeutics. *Nat Rev Immunol*, *19*(8), 477-489. https://doi.org/10.1038/s41577-019-0165-0

Swanson, R. A., Farrell, K., & Simon, R. P. (1995). Acidosis causes failure of astrocyte glutamate uptake during hypoxia. *J Cereb Blood Flow Metab*, *15*(3), 417-424. https://doi.org/10.1038/jcbfm.1995.52

Szydlowska, K., & Tymianski, M. (2010). Calcium, ischemia and excitotoxicity. *Cell Calcium*, *47*(2), 122-129. https://doi.org/10.1016/j.ceca.2010.01.003

Tarasova, N., Stauber, R., & Michejda, C. (1998). Spontaneous and Ligand-induced Trafficking of CXC-Chemokine Receptor 4*. *The Journal of Biological Chemistry*, *273*, 15883-15886. https://doi.org/10.1074/jbc.273.26.15883

Thion, M. S., Ginhoux, F., & Garel, S. (2018). Microglia and early brain development: An intimate journey. *Science*, *362*(6411), 185-189. https://doi.org/10.1126/science.aat0474

Tian, X., Yang, W., Jiang, W., Zhang, Z., Liu, J., & Tu, H. (2024). Multi-Omics Profiling Identifies Microglial Annexin A2 as a Key Mediator of NF-κB Pro-inflammatory Signaling in Ischemic Reperfusion Injury. *Molecular & Cellular Proteomics : MCP*, *23*. https://doi.org/10.1016/j.mcpro.2024.100723

Var, S. R., Shetty, A. V., Grande, A. W., Low, W. C., & Cheeran, M. C. (2021). Microglia and Macrophages in Neuroprotection, Neurogenesis, and Emerging Therapies for Stroke. *Cells*, *10*(12). https://doi.org/10.3390/cells10123555

Wake, H., Moorhouse, A. J., Jinno, S., Kohsaka, S., & Nabekura, J. (2009). Resting microglia directly monitor the functional state of synapses in vivo and determine the fate of ischemic terminals. *J Neurosci*, *29*(13), 3974-3980. https://doi.org/10.1523/jneurosci.4363-08.2009

Walter, H. L., van der Maten, G., Antunes, A. R., Wieloch, T., & Ruscher, K. (2015). Treatment with AMD3100 attenuates the microglial response and improves outcome after experimental stroke. *J Neuroinflammation*, *12*, 24. https://doi.org/10.1186/s12974-014-0232-1

Wang, K., Sun, Z., Ru, J., Wang, S., Huang, L., Ruan, L., Lin, X., Jin, K., Zhuge, Q., & Yang, S. (2020). Ablation of GSDMD Improves Outcome of Ischemic Stroke Through Blocking Canonical and Non-canonical Inflammasomes Dependent Pyroptosis in Microglia. *Front Neurol*, *11*, 577927. https://doi.org/10.3389/fneur.2020.577927

Wang, S., de Fabritus, L., Kumar, P. A., Werner, Y., Ma, M., Li, D., Siret, C., Simic, M., Li, B., Kerdiles, Y. M., Hou, L., Stumm, R., & van de Pavert, S. A. (2023). Brain endothelial CXCL12 attracts protective natural killer cells during ischemic stroke. *J Neuroinflammation*, *20*(1), 8. https://doi.org/10.1186/s12974-023-02689-x

Wang, Y., Huang, J., Li, Y., & Yang, G. Y. (2012). Roles of chemokine CXCL12 and its receptors in ischemic stroke. *Curr Drug Targets*, *13*(2), 166-172. https://doi.org/10.2174/138945012799201603

Wang, Y., Yue, X., Kiesewetter, D. O., Wang, Z., Lu, J., Niu, G., Teng, G., & Chen, X. (2014). [18F]DPA-714 PET Imaging of AMD3100 Treatment in a Mouse Model of Stroke. *Molecular Pharmaceutics*, *11*(10), 3463-3470. https://doi.org/10.1021/mp500234d

Werner, Y., Mass, E., Kumar, P. A., Ulas, T., Händler, K., Horne, A., Klee, K., Lupp, A., Schütz, D., Saaber, F., Redecker, C., Schultze, J., Geissmann, F., & Stumm, R. (2020). CXCR4 distinguishes HSC-derived monocytes from microglia and reveals monocyte immune responses to experimental stroke. *Nature Neuroscience*, *23*, 351-362. https://doi.org/10.1038/s41593-020-0585-y

Woodburn, S. C., Bollinger, J. L., & Wohleb, E. S. (2021). The semantics of microglia activation: neuroinflammation, homeostasis, and stress. *J Neuroinflammation*, *18*(1), 258. https://doi.org/10.1186/s12974-021-02309-6

Wu, K. J., Yu, S. J., Shia, K. S., Wu, C. H., Song, J. S., Kuan, H. H., Yeh, K. C., Chen, C. T., Bae, E., & Wang, Y. (2017). A Novel CXCR4 Antagonist CX549 Induces Neuroprotection in Stroke Brain. *Cell Transplant*, *26*(4), 571-583. https://doi.org/10.3727/096368916x693563

Wu, L., Xiong, X., Wu, X., Ye, Y., Jian, Z., Zhi, Z., & Gu, L. (2020). Targeting Oxidative Stress and Inflammation to Prevent Ischemia-Reperfusion Injury. *Frontiers in Molecular Neuroscience*, *13*. https://doi.org/10.3389/fnmol.2020.00028

Wu, Q. J., & Tymianski, M. (2018). Targeting NMDA receptors in stroke: new hope in neuroprotection. *Mol Brain*, *11*(1), 15. https://doi.org/10.1186/s13041-018-0357-8

Xia, X., Wang, X., Cheng, Z., Qin, W., Lei, L., Jiang, J., & Hu, J. (2019). The role of pyroptosis in cancer: pro-cancer or pro-"host"? *Cell Death Dis*, *10*(9), 650. https://doi.org/10.1038/s41419-019-1883-8

Xiao, L., Huang, Y., Wu, L., Zeng, S., Qiu, C., Li, X., Xie, L., & Wu, D. (2025). The role of inflammation in Ischemic stroke: from biomarker to treatment. *Front Immunol*, *16*, 1608353. https://doi.org/10.3389/fimmu.2025.1608353

Yang, C., Hawkins, K. E., Doré, S., & Candelario-Jalil, E. (2019). Neuroinflammatory mechanisms of blood-brain barrier damage in ischemic stroke. *Am J Physiol Cell Physiol*, *316*(2), C135-c153. https://doi.org/10.1152/ajpcell.00136.2018

Yu, F., Wang, Y., Stetler, A. R., Leak, R. K., Hu, X., & Chen, J. (2022). Phagocytic microglia and macrophages in brain injury and repair. *CNS Neurosci Ther*, *28*(9), 1279-1293. https://doi.org/10.1111/cns.13899

Yu, X., Chen, D., Zhang, Y., Wu, X., Huang, Z., Zhou, H., Zhang, Y., & Zhang, Z. (2012). Overexpression of CXCR4 in mesenchymal stem cells promotes migration, neuroprotection and angiogenesis in a rat model of stroke. *J Neurol Sci*, *316*(1-2), 141-149. https://doi.org/10.1016/j.jns.2012.01.001

Yuan, Y.-J., Chen, T., Yang, Y.-L., Han, H.-N., & Xu, L.-M. (2025). E2F1/CDK5/DRP1 axis mediates microglial mitochondrial division and autophagy in the pathogenesis of cerebral ischemia-reperfusion injury. *Clinical and Translational Medicine*, *15*(2), e70197. https://doi.org/https://doi.org/10.1002/ctm2.70197

Zhan, C., Huang, M., Yang, X., & Hou, J. (2021). MLKL: Functions beyond serving as the Executioner of Necroptosis. *Theranostics*, *11*(10), 4759-4769. https://doi.org/10.7150/thno.54072

Zhang, C., Zhao, C., Chen, X., Tao, R., Wang, S., Meng, G., Liu, X., Shao, C., & Su, X. (2020). Induction of ASC pyroptosis requires gasdermin D or caspase-1/11-dependent mediators and IFNβ from pyroptotic macrophages. *Cell Death & Disease*, *11*. https://doi.org/10.1038/s41419-020-2664-0

Zhang, M., Liu, Q., Meng, H., Duan, H., Liu, X., Wu, J., Gao, F., Wang, S., Tan, R., & Yuan, J. (2024). Ischemia-reperfusion injury: molecular mechanisms and therapeutic targets. *Signal Transduction and Targeted Therapy*, *9*. https://doi.org/10.1038/s41392-023-01688-x

Zhang, Y., Li, J., Huang, Y., Shi, Z., Wang, H., Cao, H., Tan, J., Wang, C., Wang, Y., Chen, D., Chen, S., Zhao, Y., Wang, Y., Zhu, Y., Jiang, Y., Gong, Y., & Gao, Y. (2024). *GSE220042: Arresting the Bad Seed: HDAC3 Regulates Proliferation of Different Microglia after Ischemic Stroke [RNA-seq]* National Center for Biotechnology Information. https://www.ncbi.nlm.nih.gov/geo/query/acc.cgi?acc=GSE220042

Zhao, B.-X., Zhang, S., Amin, N., Pan, J., Wu, F., Shen, G., Tan, M., Shi, Z., & Geng, Y. (2024). Thymoquinone regulates microglial M1/M2 polarization after cerebral ischemia-reperfusion injury via the TLR4 signaling pathway. *Neurotoxicology*. https://doi.org/10.1016/j.neuro.2024.02.002

Zhao, Y., Bhattacharjee, S., Jones, B. M., Dua, P., Alexandrov, P. N., Hill, J. M., & Lukiw, W. J. (2013). Regulation of TREM2 expression by an NF-κB-sensitive miRNA-34a. *Neuroreport*, *24*(6), 318-323. https://doi.org/10.1097/WNR.0b013e32835fb6b0

Zheng, D., Liwinski, T., & Elinav, E. (2020). Inflammasome activation and regulation: toward a better understanding of complex mechanisms. *Cell Discov*, *6*, 36. https://doi.org/10.1038/s41421-020-0167-x

Zheng, J., Ru, W., Adolacion, J. R., Spurgat, M. S., Liu, X., Yuan, S., Liang, R. X., Dong, J., Potter, A. S., Potter, S. S., Chen, K., Chen, R., Varadarajan, N., & Tang, S. J. (2021). Single-cell RNA-seq analysis reveals compartment-specific heterogeneity and plasticity of microglia. *iScience*, *24*(3), 102186. https://doi.org/10.1016/j.isci.2021.102186

Zinnhardt, B., Wiesmann, M., Honold, L., Barca, C., Schäfers, M., Kiliaan, A. J., & Jacobs, A. H. (2018). In vivo imaging biomarkers of neuroinflammation in the development and assessment of stroke therapies - towards clinical translation. *Theranostics*, *8*(10), 2603-2620. https://doi.org/10.7150/thno.24128

Zorov, D. B., Juhaszova, M., & Sollott, S. J. (2014). Mitochondrial reactive oxygen species (ROS) and ROS-induced ROS release. *Physiol Rev*, *94*(3), 909-950. https://doi.org/10.1152/physrev.00026.2013

8 EHRENWÖRTLICHE ERKLÄRUNG

„Hiermit erkläre ich, dass ich die vorliegende Arbeit selbständig und ohne unzulässige Hilfe oder Benutzung anderer als der angegebenen Hilfsmittel angefertigt habe. Alle Textstellen, die wörtlich oder sinngemäß aus veröffentlichten oder nichtveröffentlichten Schriften entnommen sind, und alle Angaben, die auf mündlichen Auskünften beruhen, sind als solche kenntlich gemacht. Bei den von mir durchgeführten und in der Dissertation erwähnten Untersuchungen habe ich die Grundsätze guter wissenschaftlicher Praxis, wie sie in der „Satzung der Justus-Liebig-Universität Gießen zur Sicherung guter wissenschaftlicher Praxis“ niedergelegt sind, eingehalten sowie ethische, datenschutzrechtliche und tierschutzrechtliche Grundsätze befolgt. Ich versichere, dass Dritte von mir weder unmittelbar noch mittelbar geldwerte Leistungen für Arbeiten erhalten haben, die im Zusammenhang mit dem Inhalt der vorgelegten Dissertation stehen, und dass die vorgelegte Arbeit weder im Inland noch im Ausland in gleicher oder ähnlicher Form einer anderen Prüfungsbehörde zum Zweck einer Promotion oder eines anderen Prüfungsverfahrens vorgelegt wurde. Alles aus anderen Quellen und von anderen Personen übernommene Material, das in der Arbeit verwendet wurde oder auf das direkt Bezug genommen wird, wurde als solches kenntlich gemacht. Insbesondere wurden alle Personen genannt, die direkt und indirekt an der Entstehung der vorliegenden Arbeit beteiligt waren. Mit der Überprüfung meiner Arbeit durch eine Plagiatserkennungssoftware bzw. ein internetbasiertes Softwareprogramm erkläre ich mich einverstanden.“

_____ _____

Ort/Datum Unterschrift

9 ACKNOWLEDGMENT

First and foremost, I would like to express my sincere gratitude to my supervisor, Professor Thorsten Roland Döppner, for giving me the opportunity to further explore scientific research and for helping me develop scientific thinking and problem-solving skills. I would also like to extend my special thanks to the postdoctoral researcher Dr. Sabine Huber for her guidance in experimental techniques and for supporting me through the challenges I encountered during my experiments.

I am truly grateful to all my colleagues and friends who offered their help, both in my studies and in daily life, and who made my three years in Germany fulfilling and meaningful.

I also gratefully acknowledge the generous support of the China Scholarship Council.

Finally, I wish to express my deepest love and appreciation to my husband, Guanhao Li, who not only married me in Germany but also took care of my daily life and provided constant emotional support. To my parents, I offer my profound gratitude for their moral support, love, and gentle yet persistent encouragement to pursue my dreams abroad.